2015

Search for a Permanent Electric Dipole Moment of Ra-225

Mukut R. Kalita

STUDENT AGREEMENT:

I represent that my thesis or dissertation and abstract are my original work. Proper attribution has been given to all outside sources. I understand that I am solely responsible for obtaining any needed copyright permissions. I have obtained needed written permission statement(s) from the owner(s) of each third-party copyrighted matter to be included in my work, allowing electronic distribution (if such use is not permitted by the fair use doctrine) which will be submitted to UKnowledge as Additional File.

I hereby grant to The University of Kentucky and its agents the irrevocable, non-exclusive, and royalty-free license to archive and make accessible my work in whole or in part in all forms of media, now or hereafter known. I agree that the document mentioned above may be made available immediately for worldwide access unless an embargo applies.

I retain all other ownership rights to the copyright of my work. I also retain the right to use in future works (such as articles or books) all or part of my work. I understand that I am free to register the copyright to my work.

REVIEW, APPROVAL AND ACCEPTANCE

The document mentioned above has been reviewed and accepted by the student's advisor, on behalf of the advisory committee, and by the Director of Graduate Studies (DGS), on behalf of the program; we verify that this is the final, approved version of the student's thesis including all changes required by the advisory committee. The undersigned agree to abide by the statements above.

Mukut R. Kalita, Student

Dr. Wolfgang Korsch, Major Professor

Dr. Tim Gorringe, Director of Graduate Studies

Search for a Permanent Electric Dipole Moment of ^{225}Ra

DISSERTATION

A dissertation submitted in partial

fulfillment of the requirements for

the degree of Doctor of Philosophy

in the College of Arts and Sciences

at the University of Kentucky

By

Mukut Ranjan Kalita

Lexington, Kentucky

Director: Dr. Wolfgang Korsch, Professor of Physics

Lexington, Kentucky 2015

ABSTRACT OF DISSERTATION

Search for a Permanent Electric Dipole Moment of ^{225}Ra

The observation of a permanent electric dipole moment (EDM) in a non-degenerate system would indicate the violation of discrete symmetries of Time reversal (T) or combined application of Charge (C) and Parity (P) symmetry violation through the CPT theorem. The diamagnetic ^{225}Ra atom with nuclear spin I=1/2 is a favorable candidate for an EDM search. Experimental sensitivity to its EDM is enhanced due to its high atomic mass and the increased Schiff moment of its octupole deformed nucleus. An experimental setup is developed where laser cooled neutral radium atoms are collected in a magneto-optical trap (MOT). The collected atoms are transported 1 meter with a far off-resonant optical dipole trap (ODT) and then the atoms are transferred to a second standing-wave ODT in an experimental chamber. The atoms are then optically polarized and allowed to Larmor precess in parallel and antiparallel electric and magnetic fields. The difference between the Larmor precession frequency for parallel and antiparallel fields is experimentally determined to measure the EDM. This thesis is about the first measurement of the EDM of the ^{225}Ra atom where an

upper limit of $|d(^{225}\text{Ra})| < 5.0 \times 10^{-22}$ $e{\cdot}$cm (95% confidence) is reached.

KEYWORDS: Permanent EDM, CP violation, laser cooling and

trapping, rare isotopes, radium

Author: Mukut Ranjan Kalita

Date: October 2, 2015

Search for a Permanent Electric Dipole Moment of ^{225}Ra

By

Mukut Ranjan Kalita

Dr. Wolfgang Korsch
_____
Director of Dissertation

Dr. Tim Gorringe
_____
Director of Graduate Studies

October 2, 2015
_____
Date

To my grandmother late Lakhipriya Kalita

TABLE OF CONTENTS

LIST OF FIGURES

LIST OF TABLES

Chapter 1 Introduction

The existence of a permanent electric dipole moment (EDM) in a non-degenerate system violates the discrete symmetries of Parity(P) and Time reversal (T). According to the CPT theorem T violation indicates CP violation, i.e the product of charge conjugation C and parity P. CP violation is proposed to be one of the conditions necessary for the explanation of the baryon asymmetry of the universe (BAU). CP violation has been observed in nature and this violation can be explained within the framework of the Standard Model (SM) of particle physics. However, the magnitude of CP violation within the SM is not enough to explain the observed BAU. Also, the SM is not a complete theory. Therefore to understand the fundamental nature of our universe it is important to search for new theories beyond the SM and look for new sources of CP violation.

Searches for permanent EDMs are unique tools to look for new sources of CP violation. Experimental searches for permanent EDMs have been going on for the last six decades beginning with an experiment to measure the permanent EDM of the neutron. Since then the permanent EDM experiments have been extended to other systems such as nuclei, atoms, molecules, and solids. All the permanent EDM experiments so far have yielded null results. But still, the permanent EDM limits obtained in these experiments have immensely helped in testing the SM and constrained many new theories beyond the SM severely. The sensitivity of the permanent EDM experiments is continuously being improved. However, the current experimental limits on the permanent EDMs are several orders of magnitude away from their SM predicted values. A non-zero permanent EDM will be a clear sign of physics beyond the SM

and new sources of CP violation beyond those present in the SM. This thesis is about an experiment to search for the permanent EDM of the ^{225}Ra atom. The permanent EDM of the ^{225}Ra atom is mostly sensitive to CP violating interactions within its nucleus. For this permanent EDM search an experimental setup that uses the techniques of laser cooling and trapping has been developed. The experiment involves collecting Ra atoms in a magneto optical trap and then transporting the atoms 1 meter using an optical dipole trap to our experimental region. In this region the atoms are optically polarized and allowed to Larmor precess in parallel and antiparallel electric and magnetic fields. By measuring the difference between the Larmor precession frequency for parallel and antiparallel field configurations we attempt to measure the permanent EDM. In this thesis I describe the experiment and discuss the first results of the permanent EDM search performed on the ^{225}Ra atom.

In the next sections of this chapter I introduce the definition of the EDM and then I discuss the theoretical motivations to search for the permanent EDMs. I end the chapter with a discussion of the general experimental technique that is used in most permanent EDM searches.

1.1 Permanent Electric Dipole Moments

For an electric charge distribution the EDM $\mathbf{d}$ is defined as the following integral,

$$\mathbf{d} = \int_0^{\mathbf{R}} \mathbf{r}\rho(\mathbf{r})\,\mathrm{d}^3\mathbf{r} \tag{1.1}$$

where $\rho(\mathbf{r})$ is the volume charge density and the integral extends over the volume of the charge distribution [60]. The existence of an EDM in a charge distribution indicates a displacement between its center of charge and its center of mass. From Eq.1.1 we see that the EDM is a polar vector. The EDM can be induced in a charge distribution or a charge distribution can possess a permanent EDM. If a

charge distribution has both a permanent EDM and a spin, the EDM will align with the spin which is an axial vector. This is because, according to the Wigner-Eckart theorem, the expectation value of any vector operator in an eigenstate of total angular momentum $\mathbf{J}$ is proportional to the expectation value of $\mathbf{J}$ [91]. This is also true if we think of the spin classically, because any component of an EDM not aligned with the spin direction will average out to zero. For the scope of this thesis we are interested in the permanent EDM of charge distributions with spin that exist in a non-degenerate state, meaning charge distributions which can exist in nature in only one state, with the permanent EDM either parallel to the spin or anti-parallel to the spin. This non-degenerate alignment of the permanent EDM and the spin in a system leads to the violation of certain discrete symmetries of nature. The connection of the permanent EDM and the discrete symmetry violation enables the permanent EDM searches to be a very interesting tool to probe physics at the fundamental level. In contrast, it is common for molecules such as H_2O and NH_3 to have permanent EDMs. However, in nature they can exist in both states: with their permanent EDMs parallel to the spin and with their permanent EDMs anti-parallel to the spin. These systems do not violate the discrete symmetries that I discuss in the next section and hence are not interesting for the scope of this thesis. In the reminder of this thesis I use the acronym EDM to mean the permanent EDM unless specified otherwise.

1.2 Discrete Symmetries

The three discrete symmetries that are important in the SM are: Parity transformation (P), Charge conjugation (C) and Time reversal (T). For each of these symmetries an operator is defined. Application of the operators changes the conditions of

a physical process; e.g application of the P operator corresponds to inversion of all space coordinates used to describe a process i.e P $\psi(\mathbf{x, y, z}) \rightarrow \psi(\mathbf{-x, -y, -z})$. The application of the C operator interchanges particles with antiparticles (by changing the sign of charge) i.e C $\psi_n \rightarrow \psi_{\bar{n}}$ ($\bar{n}$ represents the antiparticle of n) and application of the T operator corresponds to T $\psi(t) \rightarrow \psi(-t)$, where t represents time in a physical process. Conservation of symmetry implies that a physical process obtained after symmetry operation is equally probable as the physical process before the symmetry operation. Otherwise the process is said to violate the symmetry [44].

1.3 Violation of the Discrete Symmetries C, P and CP

Until the middle of the nineteenth century it was widely believed that physical laws conserve P symmetry and there were experimental evidence of P conservation in the strong and the electromagnetic interactions. However, in 1956 T.D Lee and C.N Yang pointed out that there was no experimental evidence of P conservation in the weak interaction [70]. In 1957 C.S Wu and her collaborator's landmark experiment on the β decay of ^{60}Co nucleus showed that P is violated in the weak interaction [108]. Violation of C and P were also observed in the same year in the decays of mu-leptons [49] and pi-mesons [74]. However combined application of C and P, CP was still thought to be conserved until 1964, when CP violation was observed in the decay of neutral K_0 particles. It was known that the neutral K_0 can turn into its antiparticle $\overline{K_0}$. In the laboratory the observed states are $|K_1\rangle$ and $|K_2\rangle$ which are linear combinations of K_0 and $\overline{K_0}$ with

$$|K_1\rangle = \frac{1}{\sqrt{2}}(K_0 - \overline{K_0})$$
$$|K_2\rangle = \frac{1}{\sqrt{2}}(K_0 + \overline{K_0}).$$

4

If CP is conserved the state $|K_1\rangle$ decays into two pions and the state $|K_2\rangle$ decays into three pions. It was found experimentally that a fraction of $(2.0 \pm 0.4) \times 10^{-3}$ of all $|K_2\rangle$ state decays into two pions, indicating CP violation [23]. Since then CP violation has been observed in the decay of neutral B meson. This experiment looked and found a CP violating asymmetry in the decay rates of B^0 and $\overline{B}^0$ to a common eigenstate [12]. Recently, CP violation has also been observed in the decays of B_S^0 meson [11]. These experiments have provided the evidence for the violation of C, P and, CP in nature. Theoretically, the combined application of C, P, T is expected to be conserved and the statement of this conservation is called the CPT theorem [66, 94, 63]. All the experimental data so far provide firm confirmation of the CPT theorem.

1.4 CP Violation and the SM

The CP violations that were observed in the K and B systems have been explained within the framework of the SM. But the interest in CP violation is far from over. This is because, CP violation is widely believed to be one of the key conditions necessary to understand the universe that we see today. The experimental evidence today indicates that the universe is fundamentally matter-antimatter asymemtric with excess of matter compared to antimatter [101, 100, 28, 104]. This is known as the baryon asymmetry of the universe (BAU). Experimental observations put an upper bound on the amount of antimatter in the universe. Theoretical estimates from standard cosmology can estimate the relative abundances of baryonic matter and antimatter. The primordial nucleosynthesis [31] model of standard cosmology can predict the cosmological abundance of the light elements H, ^{3}He,^{4}He, D, B and

^{7}Li with the requirement of only a one input parameter η given by

$$\eta \equiv \frac{n_B}{s} = \frac{n_b - n_{\bar{b}}}{s},\tag{1.2}$$

where n_b is the number density of baryons in the universe, $n_{\bar{b}}$ is the number density of anti-baryons in the universe, n_B is the difference between these two and s is entropy density of the universe. Using the standard cosmological model a complete and accurate description of the evolution of the universe from extremely early times (a few minutes) to the present day (10-20 billion years) can be obtained starting from a set of initial conditions one of which is the value of η. Modern cosmology attempts to explain the required initial conditions on the basis of quantum field theories of elementary particles in the early universe. The generation of the observed value of η ($1.5 \times 10^{-10} < \eta < 7 \times 10^{-10}$) in this context is referred to as baryogenesis [104]. In 1967 Andrei Sakharov described three minimum properties of nature which are required for any baryogenesis to occur, regardless to the exact mechanism [90]. These minimum properties are known today as Sakharov conditions:

1) At least one Baryon number violating process.

2) C and CP- violation.

3) Interactions outside of the thermal equilibrium.

The SM possesses these properties [48]. The SM has two sources of CP violation: a single complex phase δ, in the Cabibbo-Kobayashi-Maskawa (CKM) quark-mixing matrix to parametrize the interaction of quarks with W bosons and the T and P violating product of the gluon field strength tensor and its dual characterized by the parameter $\bar{\theta}$ [65]. However, these two sources of CP violation in the SM cannot create the necessary conditions leading to the BAU that we observe today. This strongly suggests that there are other sources of CP violation beyond those present in the SM that are yet to be discovered [84].

6

Also, even though the SM is experimentally verified in many aspects, there are still unresolved issues with it [48]. For example, the SM does not solve the mass hierarchy problem-why the masses of the known particles are so much smaller than the fundamental Planck mass (10^{19} GeV/c^2) or the grand-unification mass (10^{16} GeV/c^2) and the SM does not incorporate gravity [47, 93]. The realization that the SM is not a complete description of nature, motivates the search for new theories beyond the SM.

1.5 EDMs and CP Violation

EDM experiments play a very important role in the searches for new sources of CP violation and the searches for new theories beyond the SM. This is because the existence of an EDM in a non-degenerate system violates CP and hence EDM experiments can be used to directly observe the evidence for CP violation and test the SM and the theories beyond the SM. The CP violation in the context of EDMs can be explained by considering a non-degenerate system with EDM $\mathbf{d}$ and internal spin angular momentum $\mathbf{J}$. As mentioned earlier, the direction of $\mathbf{d}$ can only be parallel to $\mathbf{J}$ or anti-parallel to $\mathbf{J}$. Therefore the EDM can be written as

$$\mathbf{d} = \alpha \mathbf{J}, \tag{1.3}$$

where α is a proportionality constant. Now, under the application of P the polar vector $\mathbf{d}$ changes sign but the axial vector $\mathbf{J}$ does not. So a non-zero $\mathbf{d}$ violates P. It was shown by Landau that EDMs also violate T [69, 63]. This is because, under the application of T, $\mathbf{d}$ does not change sign but $\mathbf{J}$ changes sign [63]. According to the CPT theorem, T violation indicates CP violation and thus a non-zero EDM in a non-degenerate system also violates CP. The cartoon in Fig. 1.1 illustrates these ideas,

7
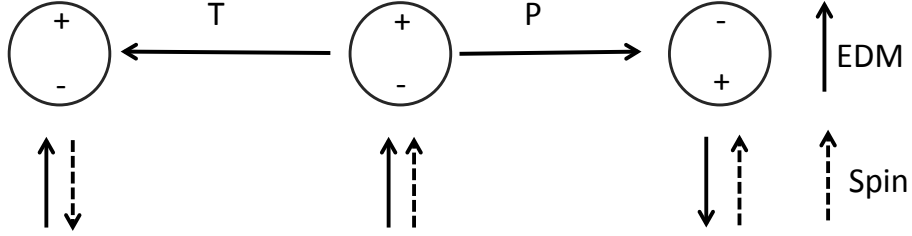
Figure 1.1: Under application of T the EDM direction remains the same but the spin direction changes, under application of P the EDM direction changes but the spin direction does not change. The solid arrow shows the EDM direction and the broken arrow shows the spin direction.

1.6 EDMs in the SM and Beyond

The EDMs predicted by the SM are non-zero. The EDMs in the SM arise because of the CP violating phase δ present in the CKM matrix. However, the SM predicted values of quark and electron EDMs are quite small. This is because the quark EDMs identically vanish at the one and two loop level and the leading order contributions to quark EDM come in three loop order. The first non-zero contribution to charged lepton EDMs come in four loop order. The SM predicted values of quark and electron EDM are $\sim 10^{-34}$ $e{\cdot}$cm [61, 32] and $\sim 10^{-38}$ $e{\cdot}$cm [85], respectively where e is the charge of the electron. The predicted neutron EDM value based on the SM is $\sim 10^{-31}$-10^{-33} $e{\cdot}$cm [61, 67]. These SM predictions of EDM are still orders of magnitude away from the sensitivity reach of current generation of EDM experiments. The other source of CP violation in the SM known as strong CP violation is very small and the parameter $\bar{\theta}$ is experimentally bound to be $<10^{-10}$ [51], although there is no theoretical explanation for the small size of $\bar{\theta}$. The lack of established explanation for

the small size of $\bar{\theta}$ is known as the "strong CP problem". The plausible explanations include spontaneous symmetry breaking at low energies [79] and predict the existence of a new fundamental particle called the *axion* [106, 107, 67].

Some theories beyond the SM include new sources of CP violation and predict EDM values different and often bigger than values predicted by the SM [18, 56]. However, the null results of the EDM searches so far have put severe constraints on these theories. One of the well motivated extensions of the SM is the supersymmetric model (SUSY) which indicates symmetry of nature at high energies which is broken at the electroweak scale. SUSY relates bosons and fermions according to which every fermion has a bosonic super partner and *vice versa*. For example, fermionic quarks are partners of bosonic squarks. Similarly bosonic gluons are are partners of fermionic gluinos. The minimal supersymmetric extensions of the SM (the MSSM) contains super-partners for all the particles of the SM. Some of their coupling constants are determined by SUSY and the known coupling constants of the SM. Most of the remaining coupling constants and the masses of the super-partners depend on the details of how SUSY is broken. These parameters are known as soft-breaking parameters. The number of parameters are of $\mathcal{O}(100)$ and there are few dozen CP violating phases. The EDMs in SUSY can be generated at one loop level. Also the mixing angle/Yukawa coupling suppression are not present for EDMs induced by the phases of the soft-breaking parameters. As a result the EDMs in SUSY are larger than the SM predictions. EDMs are also sensitive to flavor-changing terms in the soft-breaking sector and provide significant constraints on SUSY models with non-minimal flavor structure [84, 93]. This means EDM experiments can provide valuable information in constraining various SUSY models.

To fully explore the nature of EDM generating mechanisms the theoretical and experimental searches for EDMs are carried out in different systems such as nuclei,

9

atoms, molecules and solids [25, 41]. Our system of interest the ^{225}Ra atom, is dia-magnetic. Measurements of EDMs in the diamagnetic systems (zero total electron angular momentum) are mostly sensitive to hadronic sources of P, T violation while measurements of EDMs in paramagnetic systems (non-zero total electron angular momentum) are mostly sensitive to leptonic sources of P, T violation, in particular the electron EDM. Both systems are sensitive to P, T violating semi-leptonic pro-cesses (the electron-nucleon interaction); paramagnetic systems to those involving electron spin and the diamagnetic systems to those involving nuclear spin [50].

1.7 Search for EDMs in Different Systems

The first experiment to search for the EDMs began in 1957, with an experiment carried out by Purcell and Ramsay at Oakridge National Laboratory, Oakridge to measure the EDM of the neutron. From this experiment they put an upper limit on the EDM of the neutron at 5×10^{-20} $e \cdot$cm [98]. In the last six decades several neutron EDM experiments were carried out. With each experiment the upper limit on the neutron EDM was gradually improved. Currently, the best experimental limit on the neutron EDM is 3×10^{-26} $e \cdot$cm (90% confidence limit (C.L.)) resulting from an experiment carried out at Institut Laue-Langevin, Grenoble [16]. This result is still 5-6 orders of magnitude away from the SM predicted value for the neutron EDM. The search for the EDM of the neutron is far from over and there are several ongoing and proposed experiments around the world to improve the limit on the EDM of the neutron [68, 80]. There are several EDM searches performed in paramagnetic atoms ^{85}Rb [42], ^{133}Cs [73], ^{205}Tl [88], metastable ^{129}Xe [83], and ^{211}Fr [67]. The results from all these EDM searches are still consistent with a zero value for the EDM. Most recently, EDM searches done in molecular systems have provided an improved

limit on the EDM of the electron [59, 30]. The current upper limit on the electron EDM is 8.7×10^{-29} $e \cdot$cm (90%C.L.) obtained from an experiment that used the ThO molecule [30]. Electron EDM searches were also performed in $\text{Eu}_{0.5}\text{Ba}_{0.5}\text{TiO}_3$ which is a solid state system [39]. In diamagnetic systems EDM searches have been performed in ^{129}Xe [105, 75, 1, 2] ,^{199}Hg [51]. There are ongoing efforts to measure the EDM of two isotopes of the Rn atom (^{221}Rn and ^{223}Rn). The best limit on the EDM of diamagnetic atoms comes from the ^{199}Hg experiment. This puts an upper limit on the EDM of ^{199}Hg at 3.1×10^{-29} $e \cdot$cm (90%C.L.). EDM searches have also been performed on the muon [19]. There are proposed experiment to search for the EDM of the proton and the deuteron [3]. In the following table I summarize the most sensitive experimental results and their corresponding SM predictions for the EDMs in four different systems.

System	Experimental value	SM prediction
Neutron	$< 3 \times 10^{-26}$ $e \cdot$cm (90%C.L.) [16]	$< 10^{-32}$ $e \cdot$cm [62]
Electron	$< 8.7 \times 10^{-29}$ $e \cdot$cm (90%C.L.) [30]	$< 10^{-38}$ $e \cdot$cm [85]
Muon	$< 1.9 \times 10^{-19}$ $e \cdot$cm (95%C.L.) [19]	$< 10^{-36}$ $e \cdot$cm [43]
^{199}Hg	$< 3.1 \times 10^{-29}$ $e \cdot$cm (95%C.L.) [51]	10^{-33} $e \cdot$cm [84]

Table 1.1: Experimental values of EDMs in four different systems and their theoretical predictions based on SM calculations.

The following figure (from ref.[84]) shows a plot of the hierarchy of energy scales between the CP-odd sources and three generic classes of observable EDMs.

1.8 General Scheme of EDM Experiments

As we have seen from the preceeding sections, the EDM signal that we are interested in is very small. Therefore in most EDM experiments the EDM signal is converted into a frequency signal and a frequency or a phase measurement is performed on the
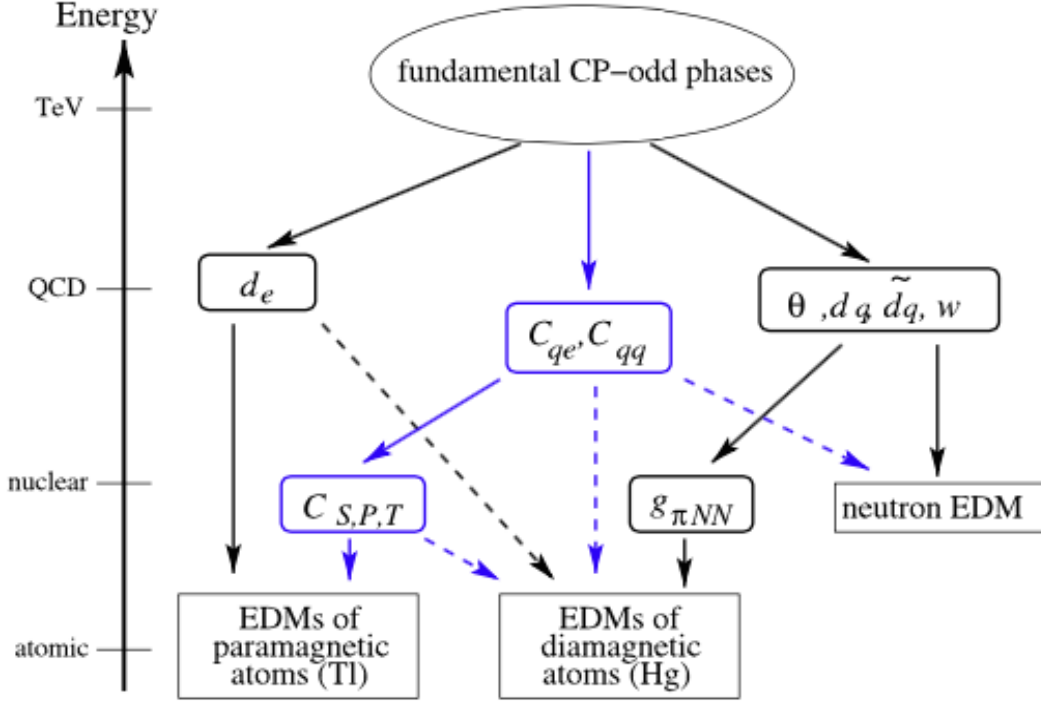
Figure 1.2: The above figure is adopted from reference [84]. The dashed lines indicate generically weaker dependencies.

signal. This is because, experimentally it is easier to perform a frequency measurement. To convert the EDM signal to a frequency signal the species under investigation is subjected to parallel electric(E) and magnetic(B) fields. Then it is polarized in the transverse direction to the fields. If the species has an EDM, the EDM will couple to the E field in a manner similar to the coupling of the magnetic moment to the B field. The interaction Hamiltonian can be written as

$$H = -(\boldsymbol{\mu}.\mathbf{B} + \mathbf{d}.\mathbf{E}) \tag{1.4}$$

where $\boldsymbol{\mu}$ is the magnetic dipole moment and $\mathbf{d}$ is the EDM. Usually a small value for the B field and a large value for the E field are used. The B field acts as a holding field and it is generally used for the confirmation measurement of the polarization.

12

For a spin 1/2 particle the resulting precession frequency(ω_+) can be written as

$$\hbar\omega_+ = (2\mu B + 2dE) \qquad (1.5)$$

where $\hbar$ is the reduced Planck constant. If the direction of the E field is reversed the precession frequency(ω_-) becomes

$$\hbar\omega_- = (2\mu B - 2dE) \qquad (1.6)$$

This means, by keeping the B field constant and measuring the difference in precession frequency ($\Delta\omega$) between the E field parallel to the B field and the E field antiparallel to the B field the EDM d can be measured according to the following equation,

$$\Delta\omega = 4dE/\hbar \qquad (1.7)$$

The goal of an EDM experiment is then to measure this difference in precession frequency with utmost precision.

In our experiment, we have used a slight variant of this technique. We polarize the ^{225}Ra atoms in presence of the B field only. The E field is turned on after the atoms are polarized and kept on for a finite time τ. A phase measurement is performed after the E field is turned off. The measurement is done with E field parallel to the B field and the E field antiparallel to the B field. A non-zero EDM will cause a polarity dependent phase shift $\Delta\phi = \Delta\omega\tau$ between the two cases. From this we measure the EDM given by

$$d = \frac{\hbar\Delta\phi}{4E\tau} \qquad (1.8)$$

1.9 Sensitivity Estimate

The sensitivity of EDM experiments can be estimated by estimating how well the precession frequency can be determined. In general, the longer the allowed precession

time τ, the smaller the uncertainty in the determination of a given frequency, so

$$\delta\nu = \frac{1}{\tau} \tag{1.9}$$

For n number of measurements the shot noise limited sensitivity is

$$\delta\nu = \frac{1}{\tau\sqrt{n}} \tag{1.10}$$

with n given by

$$n = \frac{NT}{\tau}\epsilon \tag{1.11}$$

where N is the total number of particles used in the measurement, T is the total duration of the experiment and ϵ is the efficiency of a single measurement. Using the contribution of the EDM in an E field to the precession frequency, the sensitivity of an EDM measurement can be written as,

$$\delta d = \frac{\hbar}{2E\sqrt{NT\tau\epsilon}} \tag{1.12}$$

Therefore, the design goal of an EDM experiment includes increasing all the parameters in the denominator of the above equation. e.g. if we use E field E=100 kv cm^{-1}, number of atoms N=1×10^6 atoms, spin precession time of τ=100 s and detection efficiency of ϵ=1 then according to Eq. 1.12 EDM sensitivity of 3×10^{-28} e·cm can be reached in $T = 100$ days.

Chapter 2 EDMs in Neutral Atoms

In this chapter I discuss the origin of the EDM in neutral atoms and discuss about the properties of ^{225}Ra that makes it a favorable system for an EDM search.

As I have discussed in the previous chapter, the usual way of measuring the EDM of a particle involves putting the particle in an external E field and detecting its response to this external field. For a neutral particle; such as an atom placed in an external uniform E field the net force on the atom is zero (evident from the fact that a neutral particle does not move in an E field). This can be explained by considering the fact that an atom constitutes of a positively charged nucleus surrounded by a negatively charged electron cloud. When the atom is placed in the external E field , the electron cloud rearranges itself creating an internal E field opposite in direction to the external E field . This effect results in the shielding of the nucleus from the external E field [86]. This shielding is exact for a point like nucleus, meaning the net E field at the nucleus is zero. Therefore, if a point like nucleus has an EDM it will be completely screened by the atomic electrons and we will not be able to measure it by putting it in an external E field [86]. However, real nuclei have finite volumes. Schiff showed in 1963 that for a nucleus of finite volume shielding of the external E field by the internal E field is not perfect over the nuclear volume [92]. This makes it possible to probe the atomic nucleus using an external E field and search for quantities such as the EDM.

2.1 Schiff Moment and the EDM

The EDM in a diamagnetic atom arises not because of the EDM of its nucleus. Instead the EDM in an atom is induced due to the electrostatic interaction between the atomic electrons and the nuclear Schiff moment [45]. The Schiff moment reflects the mean-square radius of the nuclear dipole distribution. This means, the larger the Schiff moment the larger is the induced EDM in the atom. The expression for the Schiff moment can be obtained by a multipole expansion of the electrostatic potential of the nucleus atom considering the screening by the atomic electrons. The lowest order T-, P-odd nuclear moment in the expansion is defined as the Schiff moment. The Schiff moment $\mathbf{S}$ can be written as [40],

$$\mathbf{S} = \frac{1}{10}\left[\mathbf{O}_0 - \frac{5}{3}\mathbf{d}_0\langle r^2\rangle_{ch}\right], \tag{2.1}$$

where $\mathbf{d}_0$ is the dipole moment of the nuclear charge distribution given by

$$\mathbf{d}_0 = \int d^3x\ \mathbf{x}\rho(\mathbf{x}), \tag{2.2}$$

and $\mathbf{O}_0$ is the second moment of the dipole distribution given by

$$\mathbf{O}_0 = \int d^3x\ \mathbf{x}x^2\rho(\mathbf{x}). \tag{2.3}$$

For this discussion we consider the collective Schiff moment of a deformed nucleus. The moments such as the collective dipole, octupole, and the Schiff moment, can exist in the body-fixed system of a deformed nucleus without any T, P violation. These moments are oriented along the nuclear axis. However, the nucleus rotates and the average values of these moments are zero for a rotational state in the laboratory system. T-, P- odd interactions within the nucleus mixes the rotational doublet states and produces an average orientation of the nuclear axis $\mathbf{n}$ along the nuclear

16

spin **I**. This results in the non-zero values of these moments, such as the Schiff moment in the laboratory frame [15].

This can be seen by considering a nearly degenerate rotational parity doublet of an axially symmetric nucleus. The wave functions of the members of the parity doublet can be written as

$$\psi_\pm = \frac{1}{\sqrt{2}}(|IMK\rangle \pm |IM-K\rangle), \qquad (2.4)$$

where I is the nuclear spin, $M = I_z$ and K=$\mathbf{I}\cdot\mathbf{n}$; $\mathbf{n}$ is a unit vector along the nuclear axis. For these states $\langle\psi_\pm|\mathbf{I}\cdot\mathbf{n}|\psi_\pm\rangle = 0$, because K and $-K$ have equal probabilities and this means there is no average orientation of the nuclear axis in the laboratory frame and $\langle\psi_\pm|\mathbf{n}|\psi_\pm\rangle = 0$ if T and P are conserved. The correlation $\mathbf{I}\cdot\mathbf{n}$ violates T and P as discussed in section 1.5.

If $\hat{V}_{PT}$ represents the T and P violating interactions, then its presence in the nucleus will mix the members of the parity doublet. Following ref.[55] and [57] the expression for $\hat{V}_{PT}$ can be written as,

$$\hat{V}_{PT}(\mathbf{r}_1 - \mathbf{r}_2) = -\frac{g\, m_\pi^2}{8\pi m_N}\left\{(\boldsymbol{\sigma}_1 - \boldsymbol{\sigma}_2).(\mathbf{r}_1 - \mathbf{r}_2)\left[\bar{g}_0\boldsymbol{\tau}_1.\boldsymbol{\tau}_2 - \frac{\bar{g}_1}{2}(\boldsymbol{\tau}_{1z} + \boldsymbol{\tau}_{2z})\right.\right.$$
$$\left.\left.+\bar{g}_2(3\boldsymbol{\tau}_{1z}\boldsymbol{\tau}_{2z} - \boldsymbol{\tau}_1.\boldsymbol{\tau}_2)\right] - \frac{\bar{g}_1}{2}(\boldsymbol{\sigma}_1 + \boldsymbol{\sigma}_2).(\mathbf{r}_1 - \mathbf{r}_2)(\boldsymbol{\tau}_{1z} - \boldsymbol{\tau}_{2z})\right\}\times \qquad (2.5)$$
$$\frac{\exp(-m_\pi|\mathbf{r}_1 - \mathbf{r}_2|)}{m_\pi|\mathbf{r}_1 - \mathbf{r}_2|}\left[1 + \frac{1}{m_\pi|\mathbf{r}_1 - \mathbf{r}_2|}\right]$$

where, the $\bar{g}$'s are the unknown isoscalar, isovector and isotensor T violating pion-nucleon couplings and g is the usual πNN coupling constant, m_N is the nucleon mass and $\hbar=c=1$.

Now, the admixed wave function of the predominantly positive parity member of the doublet can be written as $\psi = \psi_+ + \alpha\psi_-$ or

$$\psi = \frac{1}{\sqrt{2}}[(1+\alpha)|IMK\rangle + (1-\alpha)|IM-K\rangle] \qquad (2.6)$$

17

where α is the T and P violating admixture

$$\alpha = \frac{\langle\psi_-|V_{PT}|\psi_+\rangle}{E_+ - E_-} = \frac{\langle\psi_-|V_{PT}|\psi_+\rangle}{\Delta E} \tag{2.7}$$

and ΔE is the energy splitting between the members of the doublet. Consideration of the negative parity member also leads to a similar expression. In the T (and P) admixed state

$$\langle\psi|\mathbf{I}\cdot\mathbf{n}|\psi\rangle = \langle\psi|\hat{K}|\psi\rangle = 2\alpha K \tag{2.8}$$

this means the nuclear axis $\mathbf{n}$ is oriented along the nuclear spin $\mathbf{I}$:

$$\langle\psi|\mathbf{n}|\psi\rangle = 2\alpha\frac{K}{(1+I)I} \tag{2.9}$$

Therefore in the laboratory system the Schiff moment obtains a non-zero average value. e.g in the ground state usually $M = K = I$ and

$$\langle\psi|S_z|\psi\rangle = 2\alpha\frac{I}{(1+I)I}S_{int}, \tag{2.10}$$

where S_{int} is the intrinsic Schiff moment. This expression can be used to calculate the Schiff moment when the nuclear wave functions are known.

2.2 The Case for ^{225}Ra

^{225}Ra is known to have an octupole deformed nucleus [13]. Two collective effects in octupole deformed nuclei enhance the Schiff moment in the nuclei. The first is the robust intrinsic Schiff moment of a deformed nucleus. For a deformed nucleus the intrinsic Schiff moment can be written as [40]

$$S_{int} = ZeR_N{}^3\frac{3}{20\pi}\sum_{l=2}\frac{(l+1)\beta_l\beta_{l+1}}{\sqrt{(2l+1)(2l+3)}} \approx eZR_N{}^3\frac{9\beta_2\beta_3}{20\pi\sqrt{35}}, \tag{2.11}$$

where R_N is the nuclear radius, $\beta_2 \approx 0.2$ (for ^{225}Ra) and $\beta_2 = -0.122$ (for ^{199}Hg) is the parameter of the quadrupole deformation and $\beta_3 \approx 0.1$ (for ^{225}Ra) and $\beta_3 = 0$ (for

[199]Hg) is the parameter of octupole deformation [64]. The deformation of the nucleus enhances the Schiff moment. Ref. [40] indicates that the octupole deformation needs not to be static and soft octupole vibrations can also lead to similar enhancements. The following figure represents the shape of the microscopically calculated mass distribution in [225]Ra, represented as the surface of a uniform body,
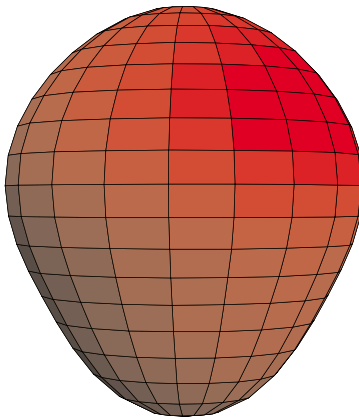
Figure 2.1: Representative shape of the [225]Ra nucleus adopted from ref. [35].

The second effect is the existence of parity doublets in this kind of nuclei. The parity doublet in [225]Ra is formed by the very low energy $|\psi_+\rangle \equiv |1/2_+\rangle$ state above the ground state $|\psi_-\rangle \equiv |1/2_-\rangle$. These two states are separated by 55.2 keV [15]. Because $\hat{V}_{PT}$ contains pseudoscalar terms it connects $|\psi_-\rangle$ and $|\psi_+\rangle$ states. The small energy denominator for the [225]Ra atom makes it a sensitive system for tests of P, T violation in the nucleon-nucleon interaction as can be seen from the expressions 2.7 and 2.10.

These two effects together with large nuclear charge lead to the enhancement of Schiff moment in a nucleus like [225]Ra. According to collective model estimates the Schiff moment of [225]Ra is factor of few hundred to few thousand times than that of [199]Hg. As mentioned in an earlier chapter [199]Hg was used to put the best

experimental EDM limit in the nuclear sector so far [15, 99, 51].

Using the expression for $\hat{V}_{PT}$ in Eq. 2.5, the Schiff moment can be written as

$$S = a_0 g\bar{g}_0 + a_1 g\bar{g}_1 + a_2 g\bar{g}_2, \tag{2.12}$$

where the coefficients a_i's have units of $e \cdot \text{fm}^3$. According to Schiff moment calculations of ^{199}Hg in ref. [34] and ref. [33] the following values for the coefficients a_i's have been obtained

$$\text{for } ^{199}\text{Hg}: \quad a_0 = 0.0004, \quad a_1 = 0.055, \quad a_2 = 0.009. \tag{2.13}$$

Ref. [35] shows calculations of the values of a_i's for ^{225}Ra at several levels of approximation. The following values of a_i's for ^{225}Ra were obtained using the SkO$'$ model and both including direct and exchange short range correlations,

$$\text{for } ^{225}\text{Ra}: \quad a_0 = -1.7, \quad a_1 = 6, \quad a_2 = -3.5. \tag{2.14}$$

These calculations indicate that the a_i coefficients for ^{225}Ra are more than two orders of magnitude larger than the coefficients for ^{199}Hg. Atomic calculations relating Schiff moments to induced EDMs indicate another factor of three enhancement in the EDM of ^{225}Ra over that of the EDM of ^{199}Hg [38]. Because of the enhancement of the Schiff moment in ^{225}Ra, an EDM measurement of ^{225}Ra can have significantly larger sensitivity to nuclear T and P violating interactions compared to an EDM measurement in ^{199}Hg.

Similar to ^{225}Ra there are other atoms with deformed nuclei, such as $^{221/223}$Rn [103] and ^{239}Pu [40] with high Z, large Schiff moment, and nuclear spin $\mathbf{I} = 1/2$ that are identified as good candidate for EDM searches in the nuclear sector. The EDM search in the radon isotopes are currently undergoing at TRIUMF.

Chapter 3 Properties of Radium

Radium was discovered in 1898 by Marie Curie. It is the heaviest alkaline earth element with atomic number Z=88. Radium has 33 different isotopes [4]. We use two the isotopes of radium in our experiment, ^{225}Ra and ^{226}Ra. In the following table I list some properties of these two isotopes that are relevant to our experiment.

Atomic mass (A)	Nuclear spin (I)	Nuclear magnetic moment (μ_N)	Half-life ($T_{\frac{1}{2}}$)
225	$\frac{1}{2}$	-0.7338(15)[14]	14.9 Days
226	0	0	1600 Years

Table 3.1: Relevant properties of the two radium isotopes used in our experiment.

^{225}Ra is produced as a decay product of ^{233}U. The following figure (Fig. 3.1) shows the nuclear decay chain of ^{233}U.
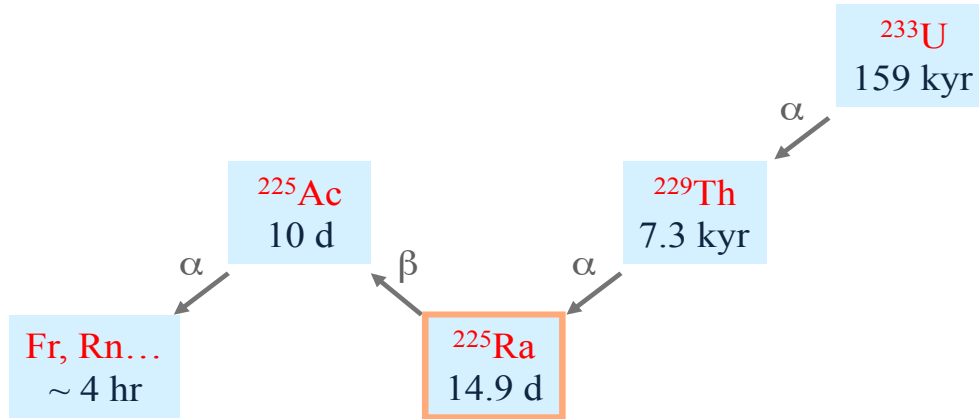
Figure 3.1: Decay chain of ^{233}U.

The long lived isotope ^{226}Ra with spin $I = 0$ ground state is used during the tuning phase of the experiment. However, because of its zero nuclear spin it cannot

be used for a nuclear spin precession experiment. The actual EDM experiment is performed with the isotope ^{225}Ra which has a spin $F = \frac{1}{2}$ ground state ($S = 0$, $I = \frac{1}{2}$). The use of $F = \frac{1}{2}$ isotope eliminates the quadrupole effects in a magnetic field.

The radioactivity of radium limits the quantity of radium that can be used for the experiment from a practical point of view. During the tuning phase of the experiment we have typically used 2-5 μCi ($\sim 10^{16}$ atoms) of ^{226}Ra. To perform the EDM experiment described in this thesis we have used 3 mCi and 6 mCi ($\sim 10^{14}$ atoms) of ^{225}Ra. This means we have to work with about 100 times fewer number of ^{225}Ra atoms than the ^{226}Ra atoms. This demands efficient use of the small quantity of radium atoms that are available for the EDM experiment.

Radium has a low vapor pressure. The boiling point of ^{225}Ra is 1140°C. This makes it difficult to design an EDM experiment using vapor cell techniques.

However, radium has electronic energy states that can be accessed with currently available lasers. Therefore, to prepare the limited amount of radium atoms available for the EDM experiment we have used the techniques of laser cooling and trapping of neutral atoms. In the next chapter I give an overview of the techniques that we have used to cool and trap neutral Ra atoms. The following figure (Fig. 3.2) shows the electronic energy level diagram of the radium atom, highlighting the electronic transitions that were used to cool and trap the neutral atoms.
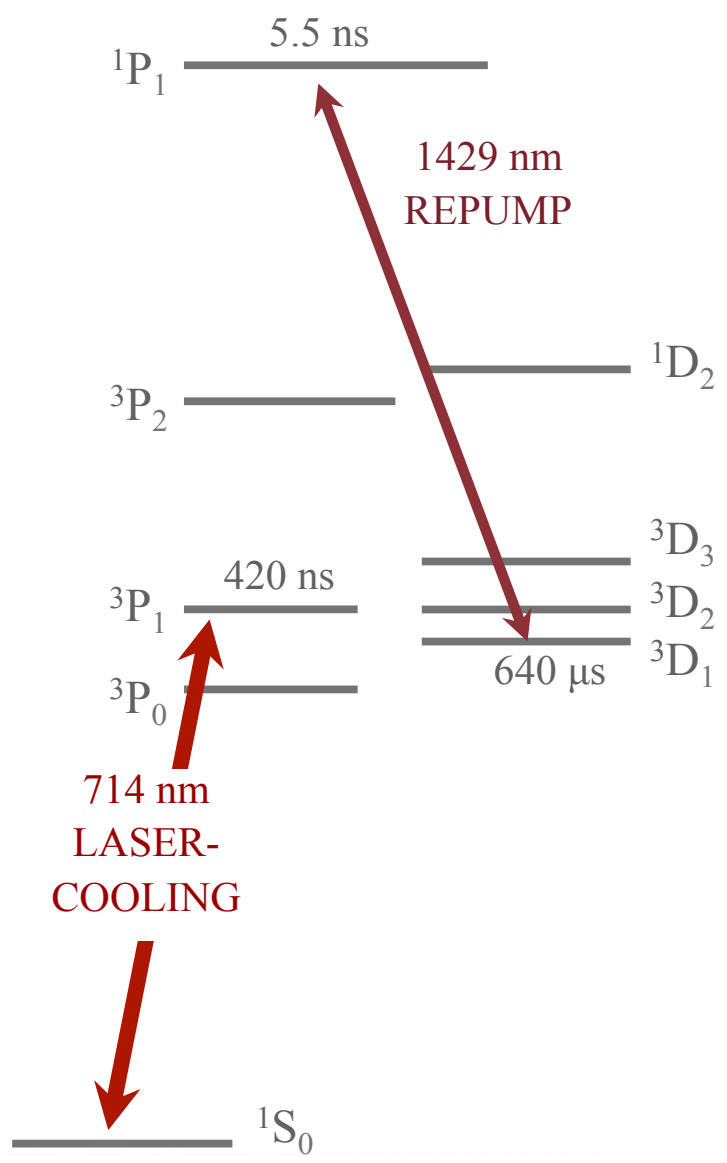
Figure 3.2: Electronic energy level diagram of radium, showing the electronic transitions that are used to laser cool and trap the neutral Ra atoms. The lifetime of the relevant atomic states are also shown.

Chapter 4 Experimental Methods

We obtain both isotopes of radium for our experiment from the U.S. National Isotope Development Center [5]. The center used to provide 10-12 mCi of ^{225}Ra every two months. Starting in June of this year (2015) the center will provide 10-12 mCi of ^{225}Ra every month. ^{225}Ra is chemically separated from a stock sample of ^{229}Th. We receive the radium in the form of a $Ra(NO_3)_2$ solution. In order to extract neutral radium atoms from this solution it is pipetted into an Al foil and placed in an effusive oven with $\sim$50 mg of Ba metal. The oven is typically run at (450-550)°C (the oven is described in a later chapter). The resulting hot atomic beam out of the oven contains neutral radium atoms as one of its constituents. We collect neutral radium atoms in an ultra high vacuum chamber from the atomic beam for the EDM experiment using the techniques of laser cooling and trapping. Using these techniques the atoms are slowed, trapped, and then transported to our experimental region[53, 77]. We first slow the atomic beam using a Zeeman slower, then we collect the slowed atoms in a magneto optical trap, and then we transport the collected atoms to our experimental region using an optical dipole trap. The 1997 Nobel prize was awarded in recognition of the successful demonstration of laser cooling and trapping of neutral atoms. There are excellent discussions on these techniques in the articles [81, 29, 24] and the references therein. In this chapter I first give a brief review of the techniques of laser cooling and trapping, the magneto optical trap and the optical dipole trap. In the later sections of this chapter, I introduce the method of optical pumping that was used to polarize the atoms and discuss about the detection principle of Larmor precession of the polarized atoms in an external uniform B field.

4.1 Laser Cooling and Trapping

In laser cooling and trapping experiments momentum exchange between atoms and laser light is utilized. Usually the laser's frequency is tuned to the frequency of an electronic transition of the atom. When the atom absorbs the laser light, the energy of light $\hbar\omega$, changes the internal energy of the atom, the angular momentum $\hbar$, changes the orbital angular momentum l of the atom, and the linear momentum of light $\hbar\omega/c = \hbar k$, changes the momentum of the atom in the laboratory frame [72]. To slow an atomic beam a well directed laser beam is send in a direction opposite to the direction of the atomic beam. At resonance the atoms will absorb photons from the laser beam and undergo excitation from their ground state to an exited state. This results in a change of momentum and the atoms feel a force in a direction opposite to their direction of velocity. If the intensity of light is low enough that the atoms have more probability of coming back to the ground state due to spontaneous emission than due to stimulated emission, photons are emitted in random directions. For many such absorption and emission cycles the spontaneously emitted photons follow a symmetric distribution. So the net momentum transfer of the atoms due to spontaneous emission averages to zero and the net force on the atoms is in the direction of the laser beam. This force $\mathbf{F}$, due to momentum exchange between light and an atom, is given by

$$\mathbf{F} = \frac{d\mathbf{p}}{dt} = \hbar\mathbf{k}\ \gamma_p \tag{4.1}$$

where $\mathbf{p}$ is linear momentum and γ_p is the excitation rate of the atoms determined by atomic physics.

The excitation rate depends on the frequency detuning of the laser beam from the atomic resonance frequency $\delta = \omega_l - \omega_a$, where ω_l is the laser frequency and ω_a

is the atomic resonance frequency. This frequency detuning changes with change in velocity of the atoms due to Doppler shift. Using optical Bloch equations it can be shown that for a two level atom the excitation rate is [72, 46]

$$\gamma_p = \frac{s_0\gamma/2}{1 + s_0 + [2(\delta + \omega_D)/2]^2} \tag{4.2}$$

where $\gamma = 1/\tau$ is angular frequency corresponding to the decay rate of an excited state. s_0 is the ratio of light intensity I to the saturation intensity $I_s = \pi h c/3\lambda^3\tau$ and $\omega_D = -\mathbf{k} \cdot \mathbf{v}$ is the Doppler shift seen by atoms moving with velocity $\mathbf{v}$. The scattering rate is maximal when $\delta = -\omega_D$. If δ is chosen for a particular velocity then as the atoms slow down they fall out of resonance with the laser beam. The momentum change due to single photon absorption is very small. For example, upon absorption of a single 714 nm photon the velocity of a ^{225}Ra atom changes by 0.24 cm/s (the recoil velocity). To stop a ^{225}Ra atom moving with initial speed of e.g. 60 m/s the atom will need to scatter $\sim 25,000$ of 714 nm photons, with every photon slowing it down by a very small amount compared to its initial velocity. This means to achieve sufficient deceleration of an atomic beam it is necessary to keep the atoms in resonance by compensating for the changes in the Doppler shift. This can be done by changing ω_D through the angular dependence of $\mathbf{k} \cdot \mathbf{v}$ or changing δ via ω_l or ω_a. The common methods of changing δ are sweeping the laser frequency ω_l with changing ω_D of the decelerating atoms or changing the atomic resonance frequency using the Zeeman effect of a spatially varying DC magnetic field to keep the atoms in resonance with a fixed frequency laser. In the second method usually a tapered solenoid magnet is used to produce the required magnetic field and the arrangement combined with the laser is called a Zeeman slower [82]. The minimum length of the slower is determined by the initial velocity of atoms that are chosen to slow down and the maximum deceleration value, which is given by $a_{max} = \hbar\mathbf{k}\,\gamma/2M$, where M is the

mass of the atom [72]. We use a 1 m long Zeeman slower to slow the radium atoms [77]. The Zeeman slower is constructed using three sets of copper coils powered by three independent current supplies. The laser beam of the Zeeman slower is typically detuned 3γ below resonance of the $7s^2$ $^1S_0 \rightarrow 7s7p$ $^3P_1$ transition of radium at 714 nm.

4.2 Magneto Optical Trap

Once the atoms are slowed they can be trapped. We use a magneto optical trap(MOT) [87] to trap the slowed atoms. The first MOT for radium was demonstrated in our laboratory in 2007 [53]. The trap consists of a quadrupole magnetic coil and three pairs of counter propagating laser beam in the three perpendicular directions. Fig. 4.1 shows the arrangement of the components of a MOT.
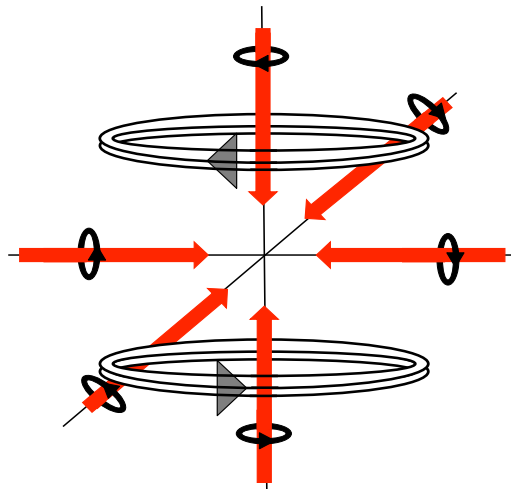
Figure 4.1: Typical arrangement of the laser light and the magnetic field used to form a MOT for neutral atoms. The red arrows represent the direction of the circularly polarized laser beams. The top and bottom rings represent current carrying coils for the quadrupole magnetic field with the arrows showing the direction of current.

Each pair of counter propagating laser beams has opposite circular polarization and the frequency of the light is tuned below the atomic resonance (red detuned). The radium MOT is designed to have zero magnetic field at the center and a gradient of 1G/cm away from the center of the trap [77]. Because of the spatially varying magnetic field the atoms experience a spatially varying Zeeman shift. A diagram of the separation of the relevant energy levels as a function of the distance from the center of a MOT is shown in Fig. 4.2 with the horizontal axis representing distance from the center of the MOT. The vertical axis is energy. The red arrows show the direction of the opposite circularly polarized laser beams. The arrows labelled B show the direction of the magnetic field.
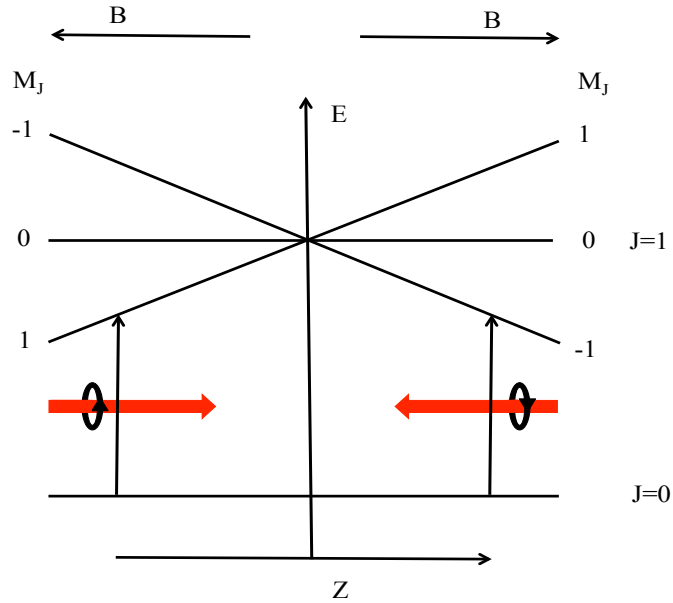
Figure 4.2: Separation of energy levels due to Zeeman splitting (not to scale) as a function of distance from the center of the MOT for the $J = 0$ and the $J = 1$ states.

The trap works for transitions where the ground and excited states have different Zeeman shifts. For radium we use the $7s^2$ $^1S_0 \rightarrow 7s7p$ $^3P_1$ intercombination tran-

28

sition. For ^{226}Ra we excite along $(J = 0) \rightarrow (J' = 1)$ and for ^{225}Ra we excite along $(F = 1/2) \rightarrow (F' = 3/2)$. The atoms in the MOT experience position dependent Zeeman shifts and they absorb light preferentially from the beam directed opposing their motion. This arrangement produces a position dependent force and the laser beams push atoms toward the center of the MOT. In a MOT the atoms experience position dependent force leading to confinement of the atoms and also a velocity dependent force leading to cooling of atoms. By using a time of flight method the temperature of the atoms was measured to be 45 ± 5 μK in our ^{225}Ra MOT [102]. The dynamics of the atoms in a MOT and detailed discussion of the working of a MOT can be found in standard textbooks [72, 46]. Fig. 4.3 shows a picture of our MOT chamber. The atoms are trapped in a custom made vacuum chamber.
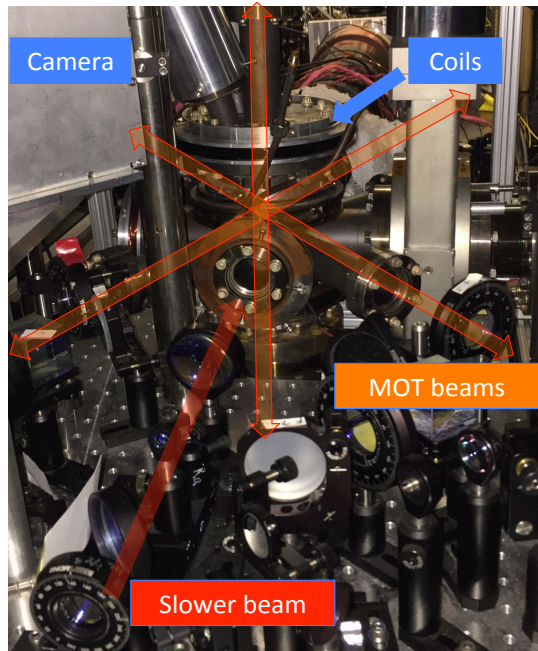
Figure 4.3: Picture of the Ra MOT chamber. The top flange is $10''$ in diameter. The semi-transparent arrows show the path of the laser beams. A camera housed in a dark enclosure is used to image the atoms in the MOT.

4.3 Optical Dipole Trap

We use the MOT to collect the radium atoms from the atomic beam. However, the MOT is not a good place to do an EDM experiment because of the difficulty in applying and controlling the uniform E and B fields. Therefore, to perform the EDM experiment we transport the atoms collected in the MOT to an experimental region 1 m away. To do this we use another type of trap, called the optical dipole trap(ODT) [24, 52]. This trap is formed by a far detuned and strongly focussed laser beam. The (ODT) utilizes the interaction of the far detuned laser light with atoms. When an atom is placed in a laser beam, the E field of the laser beam induces an atomic dipole moment $\vec{p}$ that oscillates at the driving frequency ω. The amplitude of the dipole moment is related to the field amplitude E by

$$p = \alpha E. \tag{4.3}$$

Where α is the complex polarizability which depends on the driving frequency ω.

The interaction potential of the induced dipole moment **p** in the driving field E is given by

$$U_{dip} = -\frac{1}{2} < pE > = -\frac{1}{2\epsilon_0 c} Re(\alpha) I. \tag{4.4}$$

Where the angular brackets denote the time average over the rapidly oscillating terms, the field intensity is $I = 2\epsilon_0 c |E|^2$, and the factor $\frac{1}{2}$ arises because the dipole is induced and not permanent. The dipole force results from the gradient of the interaction potential

$$F_{dip}(r) = -\nabla U_{dip}(r) = \frac{1}{2\epsilon_0 c} Re(\alpha) \nabla I(r). \tag{4.5}$$

The polarizability can be separated into two parts, the real part responsible for the dispersive properties of the interaction and the imaginary part responsible for

the absorption of light. The scattering rate can be written as

$$\Gamma_{sc}(r) = \frac{P_{abs}}{\hbar\omega} = \frac{1}{\hbar\epsilon_0 c}\text{Im}(\alpha)I(r). \tag{4.6}$$

Following a semi-classical approach as shown in [52] the general expression for the dipole potential and the scattering rate simplify to

$$U_{dip}(r) = \frac{3\pi c^2}{2\hbar\omega_0^3}\frac{\Gamma}{\Delta}I(r) \tag{4.7}$$

$$\Gamma_{sc}(r) = \frac{3\pi c^2}{2\hbar\omega_0^3}\left(\frac{\Gamma}{\Delta}\right)^2 I(r). \tag{4.8}$$

Eq. 4.7 shows that below an atomic resonance("red detuning", $\Delta < 0$) the dipole potential is negative and the interaction thus attracts the atoms into the laser field. Potential minima occurs at the positions with maximum intensity. Above resonance ("blue detuning", $\Delta > 0$) the dipole interaction repels atoms out of the laser field, the potential minima correspond to the minima of intensity. Eq. 4.7 and Eq. 4.8 show that the dipole potential scales as I/Δ, whereas the scattering rate scales as I/Δ^2. So ODTs use large detuning and high intensities to keep scattering rate as low as possible at a certain potential depth.
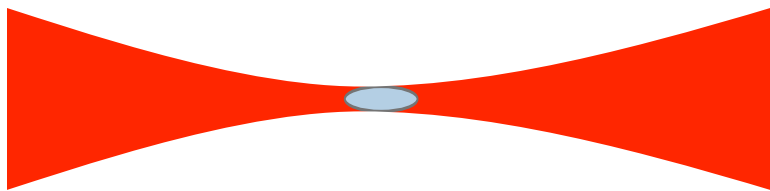
Figure 4.4: For the red detuned ODT the atoms are trapped at the focus. The blue blob represents atoms and the red shape represents a focussed laser beam.

We use two ODTs in our experiment. The first ODT (in a traveling wave configuration) is used to transport atoms from the MOT to our experimental region. The

atoms are then transferred to a second ODT (in a standing wave configuration). The EDM experiment is performed with the atoms trapped in the standing wave ODT inside a tube made of glass.

4.4 Optical Pumping

To prepare the polarization of the atoms transverse to the B field we use an optical pumping scheme. The following figure shows the scheme.

$m_F = -1/2$ ——— $^1P_1$ (F=1/2) ——— $m_F = +1/2$

483 nm

σ_+

$m_F = -1/2$ ——— $^1S_0$ (F=1/2) ——— $m_F = +1/2$
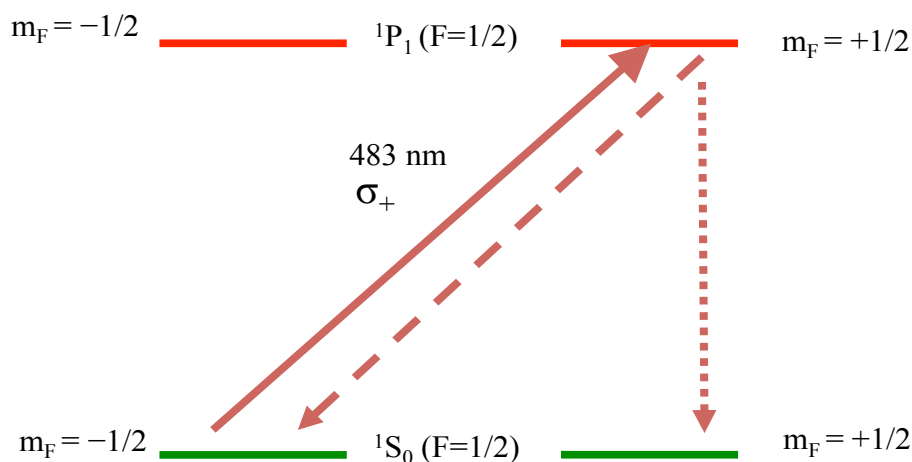
Figure 4.5: The optical pumping scheme.

As shown in Fig. 4.5, initially atoms in the cloud are equally populated among the two ground state Zeeman sub levels with $m_F = \pm 1/2$. A circularly polarized "pump" laser pulse (for σ_+) selectively excites a transition from the $m_F = -1/2$ ground state (the bright state) to the $m_F = +1/2$ excited state with $\Delta m_F = +1$. The atoms in the excited state can decay to either $m_F = -1/2$ or $m_F = +1/2$ ground state by spontaneous emission or by collisions with background gas molecules. Because of angular momentum conservation (σ_+ light only excites transitions with $\Delta m_F = +1$) the atoms in the $m_F = +1/2$ ground state (the dark state) do not interact with the

"pump" laser pulse. The atoms that decay to the bright state can again absorb the "pump" laser pulse and pump out of this state. Eventually after a few absorption and decay cycles all the atoms are transferred to the dark state with $m_F =+1/2$ and the atom cloud becomes transparent to further pulses of "pump" laser light. This ground state population imbalance created by optical pumping corresponds to the spin polarization of the atom cloud.

When the "pump" pulse is turned off the spin polarization decays as e^{-t/T_2} where T_2 is the transverse spin relaxation time and t is time after polarization.

In our experiment we use a circularly polarized (σ) blue (483 nm) "pump" laser beam pulse directed perpendicular to the B field. The frequency of the "pump" pulse is tuned to the non cycling $7s^2$ $^1S_0$ F=1/2 $\rightarrow$7p $^1P_1$ F=1/2 transition.

4.5   Larmor Precession
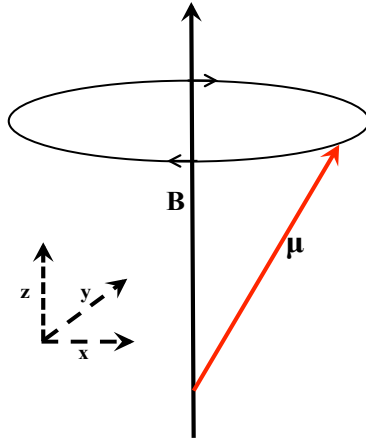
Figure 4.6: A classical magnetic moment μ placed in a B field experiences a torque. In this representation the torque is out of the plane of the paper.

A classical magnetic moment $\boldsymbol{\mu}$ placed in a $\mathbf{B}$ field experiences a torque τ given

33

by

$$\boldsymbol{\tau} = \boldsymbol{\mu} \times \boldsymbol{B} = \gamma \boldsymbol{J} \times \boldsymbol{B} \tag{4.9}$$

where γ is the gyromagnetic ratio and $\mathbf{J}$ is the angular momentum. The torque can be written as change in total angular momentum ($\boldsymbol{\tau} = \frac{d\mathbf{J}}{dt}$). Assuming the $\mathbf{B}$ field is in the $\hat{z}$ direction we can write

$$\boldsymbol{\tau} = \frac{d\mathbf{J}}{dt} = \gamma B \boldsymbol{J} \times \hat{z} \tag{4.10}$$

Separating this equation into components along the $\hat{x}$, $\hat{y}$ and $\hat{z}$ directions we can write

$$\frac{dJ_x}{dt} = \gamma B J_y \tag{4.11}$$

$$\frac{dJ_y}{dt} = -\gamma B J_x \tag{4.12}$$

$$\frac{dJ_z}{dt} = 0 \tag{4.13}$$

Differentiating eq. 4.11 and putting it into eq. 4.12 we obtain

$$\frac{d^2 J_x}{dt^2} = -\gamma^2 B^2 J_x \tag{4.14}$$

with initial conditions $J_y=0$ and $J_x = J_{x0}$ at t=0 we find

$$J_x = J_{x0} \cos(\omega t) \tag{4.15}$$

$$J_y = -J_{x0} \sin(\omega t) \tag{4.16}$$

where $\omega = \gamma B$. This means the projection of angular momentum precesses around the $\mathbf{B}$ field at the angular frequency ω.

4.6 Measurement of Larmor Precession Frequency

To measure the Larmor precession frequency we measure the absorbed fraction of a circularly polarized blue "probe" laser beam. We use the same laser beam with same polarization and frequency but with different intensity and pulse duration to "pump" and "probe" the atom cloud. If we quantize the angular momentum along the direction of propagation of the "probe" light (the $-\hat{x}$ direction) atoms with angular momentum pointed along the $+\hat{x}$ direction corresponds to the $m_F = +1/2$ state and atoms with angular momentum pointed along the $-\hat{x}$ direction corresponds to the $m_F = -1/2$ state. Referring to Fig. 4.5, if the "probe" pulse is of σ_+ polarization there is a maximum possibility of absorption of photons when the atoms are in the $m_F = -1/2$ state and there is no possibility of absorption of photons when the atoms are in the $m_F = +1/2$ state. This means that if the probability of the atoms being in the $m_F = -1/2$ state modulates with time the absorption probability will also modulate with time.

In our experiment we polarize the atoms transverse to the $\mathbf{B}$ field. Due to the $\mathbf{B}$ field the atoms undergo Larmor precession and correspondingly the probability of absorption of photons modulates at the Larmor frequency. For a spin $1/2$ particle with its angular momentum oriented in the xy plane at an angle ϕ from the $+\hat{x}$ direction, the state can be written as

$$|\phi(0)\rangle = \frac{1}{\sqrt{2}}|m_F = +1/2\rangle + \frac{1}{\sqrt{2}}e^{i\phi}|m_F = -1/2\rangle \tag{4.17}$$

Using matrix notation

$$|\phi(0)\rangle = \frac{1}{\sqrt{2}}\begin{pmatrix} 1 \\ e^{i\phi} \end{pmatrix} \tag{4.18}$$

At time t the state can be written as

$$|\phi(t)\rangle = \frac{e^{-i\omega t/2}}{\sqrt{2}} \begin{pmatrix} 1 \\ e^{i\phi + \omega t} \end{pmatrix} \tag{4.19}$$

The probability of the spin being the in the $m_F = -1/2$ state can be written as

$$\left| \frac{1}{\sqrt{2}} \begin{pmatrix} 1, & -1 \end{pmatrix} e^{-i\omega t/2} \begin{pmatrix} 1 \\ e^{i\phi + \omega t} \end{pmatrix} \right|^2 = \frac{1}{2}\left(1 - \cos(\phi + \omega t)\right) \tag{4.20}$$

where ω is the precession frequency given by $\omega = \mu/\hbar$. For ^{225}Ra in the $^1S_0$ ground state (I=1/2) the precession frequency becomes $\omega = \mu/\hbar$ where $\mu = -0.7338\mu_N$ [14]. The absorption probability of photons modulates at the precession frequency given by ω.

For an atomic cloud the polarization of the cloud can be defined as

$$\mathrm{P} = \rho_+ - \rho_- \tag{4.21}$$

where ρ_+ and ρ_- are the fraction of atoms in the $m_F = +1/2$ and $m_F = -1/2$ states respectively and

$$\rho_+ + \rho_- = 1. \tag{4.22}$$

If at t = 0, all the atoms are in $m_F = +1/2$ then $\phi = 0$, and Eq.4.20 can be generalized as

$$\frac{A}{1 + \mathrm{P}}\left(1 - \mathrm{P}\cos(\omega t)\right) \tag{4.23}$$

with A as a normalization constant that is used to correct for the decay of the signal due to T_2.

To analyze the data from our experiment we use the eq. 4.23. We measure absorption of the "probe" light by the atoms as a function of time after a "pump" pulse for three different configurations of the E and the B fields: E field off and only

B field, E field on and parallel to the B field, E field on and anti-parallel to the B field. The B field is kept on during the measurements and the E field was tuned on momentarily between the "pump" and the "probe" pulses. An EDM will produce an E- field polarity dependent phase shift in the absorption curves. In presence of the E field and a non-zero EDM d eq. 4.23 will change to

$$y_{\uparrow\uparrow/\uparrow\downarrow}(t) = \frac{A}{1+P}[1 - P\cos(\omega t + \theta \pm \Delta\phi/2)], \qquad (4.24)$$

where $y_{\uparrow\uparrow}(t)$ represents the configuration "E field parallel to the B field", and $y_{\uparrow\downarrow}(t)$ represents the configuration "E field anti-parallel to the B field" and $\Delta\phi$ is the E field polarity dependent phase shift depended on the EDM. From this the EDM can be found from $d = \hbar\Delta\phi/4E\tau$, where τ is the duration of the E field and θ is a phase generated due to effects common to both of the E field configurations.

Chapter 5 The Apparatus

The radium atoms are trapped and manipulated in a vacuum chamber made of stainless steel and glass. The experimental setup can be divided into three regions. The source region contains the radium oven that produces the atomic beam, the atom collection region is where the radium atoms are collected from the atomic beam and the experimental region is where the EDM experiment is performed. In this chapter I describe our apparatus and some of its components.

5.1 The Vacuum System

Fig. 5.1 shows a diagram of the vacuum system in which the radium atoms are trapped and manipulated.
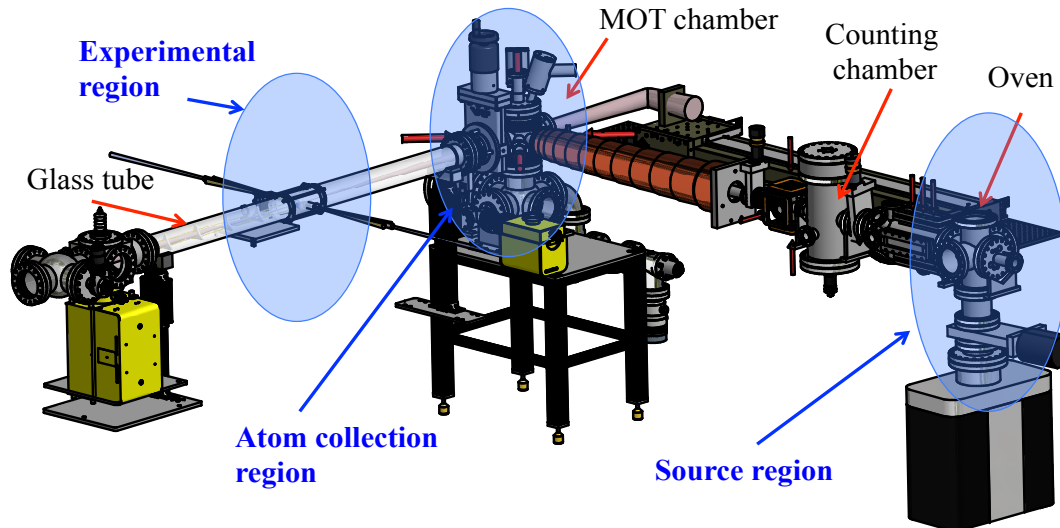
Figure 5.1: An engineering drawing of the vacuum system showing the pumps that continuously pump the system. The glass tube is 2 m long.

The vacuum system is mainly constructed using Type-304 stainless steel (obtained from MDC Vacuum Products LLC [6]). The glass tube is made of Corning 7740 Borosilicate glass. The system is pumped with a combination of several pumps. There are three ion pumps connected to the system: under the oven (Varian, Vacion150), under the MOT chamber (Gamma Vacuum, 45S) and at the end of the glass tube (Gamma Vacuum 150T with a Titanium Sublimation Pump (TSP)). The MOT chamber is also connected to a TSP and a getter pump (SAES, GP200). A similar model getter pump is connected to the end of the glass tube and another getter pump (SAES capacitor D 2000) is connected under the counting chamber. Three residual gas analyzers (RGAs) are connected to the system to monitor the gas composition: on the left side of the oven, under the MOT chamber, and at the end of the glass tube. These RGAs are not shown in Fig. 5.1. Two ion gauges, one connected to a port between the counting chamber and the Zeeman slower and the other under the MOT chamber is used to monitor the pressure. Typical pressure in the MOT chamber ranged from 9.5×10^{-10} Torr to 1.5×10^{-10} Torr. The pressure in the glass tube region is monitored by reading the current from the ion pump connected to the end of the glass tube. Pressures in the range of 2×10^{-10} Torr to 3×10^{-10} Torr were obtained in the glass tube region.

5.2 The Oven

The source region contains the radium oven. An effusive oven is used to generate the atomic beam of radium. The oven is made of titanium and it is radiatively heated using copper filaments that surround the oven assembly. A thermocouple at the back of the sample reservoir measures the temperature. A water cooled copper cooling jacket is put arround the filaments. This cooling jacket acts as a heat shield

between the filaments (typically at (450-550)°C) and the steel vacuum chamber. The following figure (Fig. 5.2) shows a schematic of the oven. Details of the oven can be found in ref. [102].
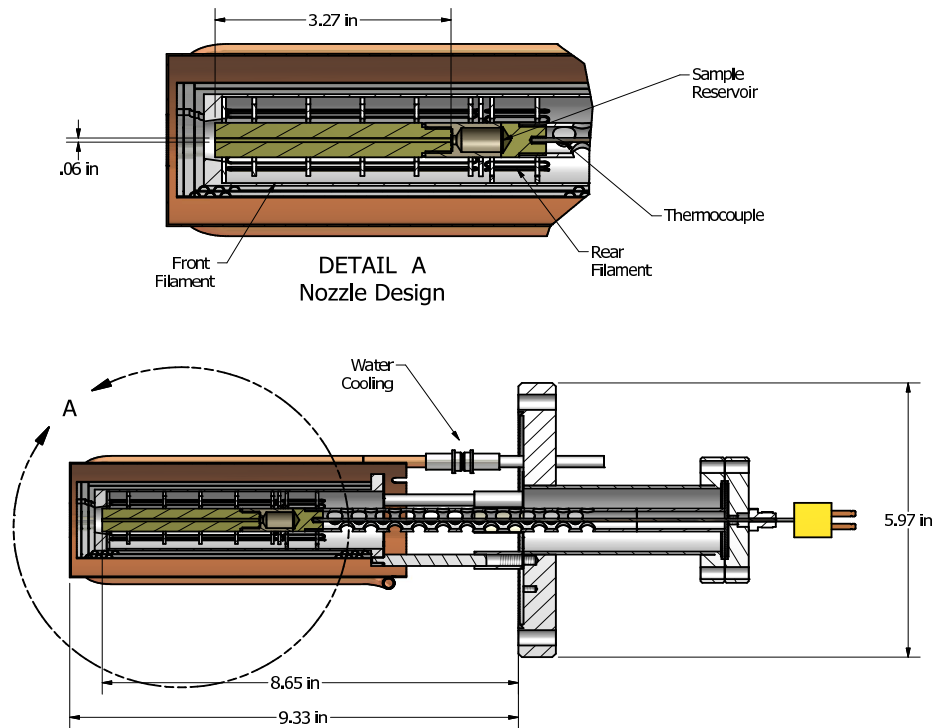
Figure 5.2: An engineering drawing of the oven.

5.3   Atomic Beam Detection System

The first step in trapping radium atoms in our system is the confirmation of the existence of a radium atomic beam coming out of the oven. A beam monitoring system is used to confirm the presence of atomic beam of radium after each new load of radium into the oven. After each new load of radium sample we monitor the atomic beam flux by using the beam monitoring system. The beam monitoring

system is located after the transverse cooling region and right before the counting chamber. Fig. 5.3 shows a schematic of this atomic beam monitoring system.
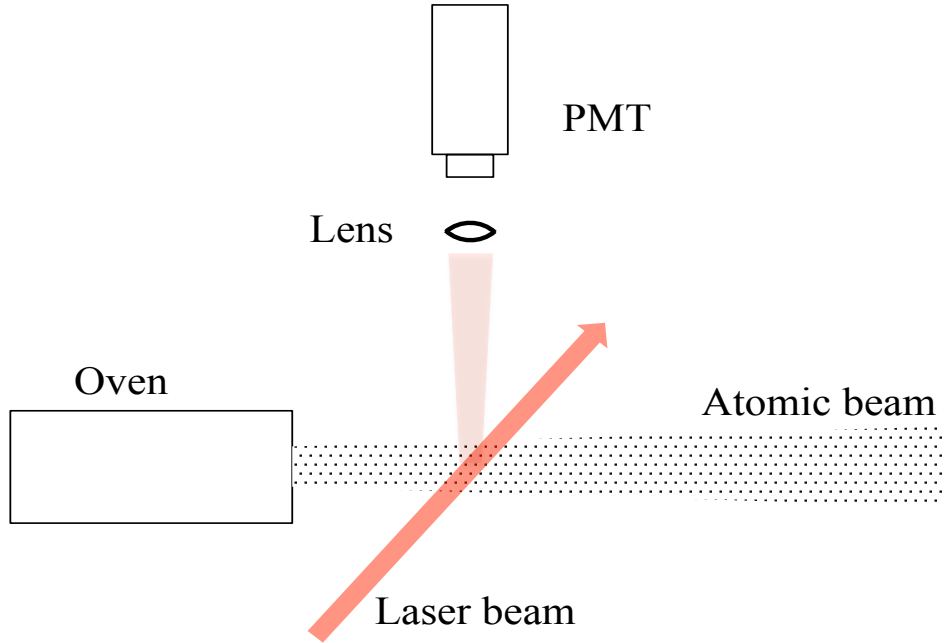
Figure 5.3: Monitoring fluorescence from the atomic beam. The laser beam is sent perpendicular to the atomic beam. Frequency of the laser beam is scanned and the fluorescence from the atoms is focussed onto a photomultiplier tube (PMT) using a lens. The PMT and the laser beam are arranged perpendicular to each other.

A 714 nm laser beam (of power ∼400 μW) with ∼4 mm diameter transversely intersects the atomic beam. A 2″ diameter, 10 cm focal length lens placed at 10 cm from the axis of the vacuum pipe collects the resultant fluorescence of the atoms from the atomic beam and focusses it onto a photomultiplier tube (PMT) (Hamamatsu, H7421-50). The data from the PMT is sent to a data aquisition (DAQ) card (NI-USB6341). A LabVIEW program is used to program a counter on the DAQ card and process the PMT data. The LabVIEW program instructs the counter to perform a measurement using the linear encoder method. To detect the radium atoms in the

atomic beam, the laser frequency is scanned using the AOM that is used to offset the laser frequency going to a ULE cavity (described in a later section). The laser beam is chopped at 1 MHz with 50% duty cycle using another AOM in double pass configuration. The 1 MHz frequency is determined by the 420 ns lifetime of the atoms in the $^3P_1$ state so that the laser is on for 500 ns and off for 500 ns. The fluorescence data is collected when the laser is off to reduce background signal due to scattered light. The following figure (Fig. 5.4) shows the signal connections to the counter on the DAQ card.

Counter	Input signal
SRC	PMT signal
GATE	1 MHz TTL
AUX	20 MHz TTL
OUT	5 V
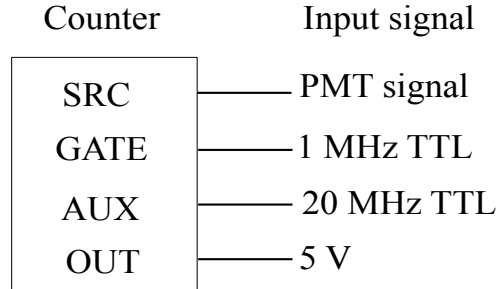
Figure 5.4: Connections to the counter on the NI-USB6341 card.

The 5 V DC signal sets the counter so that counts from the counter are increased when the counter sees both a PMT input signal and the 20 MHz TTL (50% duty cycle) input signal is high. The 1 MHz TTL (2% duty cycle) signal resets the counter after 1 μs. As mentioned, during this 1 μs the laser is off for 50% of the time. Counts from the counter are integrated for 1s at each set frequency of the laser. The integrated number of counts when the laser is off is displayed in a plot as a function of the set frequency of the scanning AOM. The following plot (Fig. 5.5) shows a typical output plot from the beam fluorescence monitoring system. The data for this plot were generated using the ^{226}Ra atomic beam and scanning the 714 nm laser frequency once across resonance. After a load of radium sample in the oven

42

data similar to that shown in Fig. 5.5 are obtained at different oven temperatures. As the temperature of the oven is increased the peak PMT counts at the resonance frequency increases with temperature, indicating increase in radium atom flux.
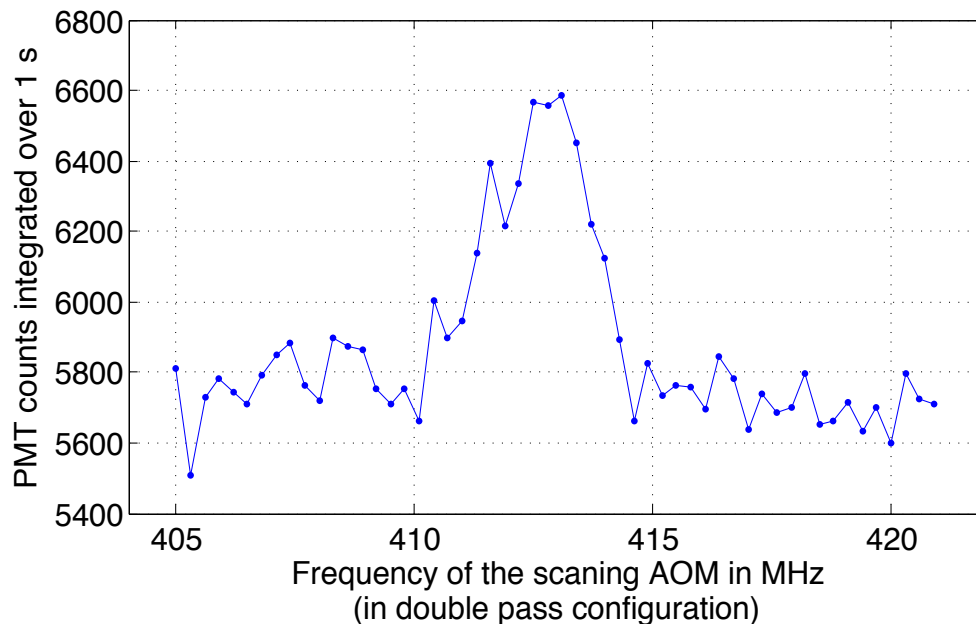
Figure 5.5: Integrated PMT counts as a function of laser frequency. At each frequency the laser beam is chopped at 1 MHz and data is collected for 1 s. PMT counts are integrated when the laser beam is off. The PMT counts reach a peak when the laser is resonant with the radium atoms in the atomic beam.

5.4   Laser Systems

We use five different laser systems in our experiment. Three lasers (one 714 nm, two 1428 nm) are used for laser cooling and trapping the atoms, and two lasers (1550 nm) are used to form the ODTs. The lasers are kept on separate tables from the vacuum system for the radium atoms. The laser light is sent to the experiment by using optical fibers.

5.4.1 The 714 nm Laser

A Titanium:Sapphire laser (Matisse, developed by Spectra-Physics) is used to obtain laser light at 714 nm. During the first phase of the experiment we pumped the Titanium:Sapphire laser using a 15 W green laser at 532 nm (Millenia Prime, developed by Spectra-Physics). However, the green laser power deteriorated over time and in the later phase of the experiment we used a 18 W green laser (Sprout-G, developed by Lighthouse Photonics) to pump the Titanium:Sapphire laser. Typically we use $\sim$(9-12) W of pump power to obtain $\sim$1.3 W of 714 nm light. This 714 nm light is distributed to the transverse cooling, the Zeeman slower and to the MOTs (3D and 1D) after appropriate frequency shifting using acousto optic modulators (AOMs) in double pass configuration (see appendix A).

5.4.2 The 1428 nm Laser

Two diode lasers with fiber coupled Fabry-Bragg-Grating (FBG) (developed by Fara-Banafsh Lasers) are used to generate the laser light at 1428 nm. The light from one laser is sent to the MOT chamber along vertical direction from top of the MOT chamber and the light from the other laser is sent along the MOT and the Zeeman slower axis. We obtain $\sim$300 mW of 1428 nm light by operating the lasers at $\sim$1500 mA of current.

5.4.3 The 483 nm Laser

The 483 nm laser light is obtained by frequency doubling a 966 nm laser beam using a PPLN waveguide (made by HC photonics). A homebuilt diode laser system in the Littrow configuration produces the 966 nm light. We obtain $\sim$1.5 mW of 483 nm light from the waveguide with $\sim$80 mW of 966 nm light.

5.4.4 The 1550 nm Laser

We used two 1550 nm lasers to generate the two ODTs. The atoms are transported using an ODT formed by a 50 W laser (ELR-50-AC, developed by IPG photonics) focussed down to 100 μm diameter. We trap the atoms in the experimental region for the EDM measurement by using a 30 W laser (ELR-30-1550-LP-SF, developed by IPG photonics) also focused down to 100 μm diameter. The 50 W laser is randomly polarized and the 30 W laser is linearly polarized.

5.5 Laser Frequency Stabilization Systems

We use the Pound-Drever-Hall (PDH) method [22] to stabilize the frequency of the 714 nm, 966 nm, and one of the 1428 nm lasers. In this method a laser's frequency is continuously measured by using a stable Fabry-Perot cavity and the measurement is fed back to the tuning port of the laser to keep the laser's frequency stable at the desired value. The cavity acts as a reference. A single Zerodur block is used to form the spacer for the two Fabry-Perot cavities for the 966 nm and the 1428 nm lasers (the spacer was purchased from Cidra Precision Services, LLC). Two sets of mirrors were purchased and added to the spacers to construct these cavities for the 966 nm and 1428 nm lasers. The second 1428 nm laser is locked to the Zerodur cavity stabilized first 1428 nm laser. The laser locking scheme involved creating a beat between the two lasers and keeping the beat frequency stable [95]. A Fabry-Perot cavity made of ultra low expansion glass (ULE, the cavity was manufactured by ATFilms) is used for stabilizing the 714 nm laser.

5.5.1   Cavity for the 714 nm Laser

We used a hemispherical cavity (one mirror is flat and the other is curved) as a reference for the 714 nm laser. The mirrors and the spacer of this cavity are made of ULE glass. The mirrors are 2.54 cm in diameter and they are separated by 10 cm. The radius of curvature of the curved mirror is 50 cm. We usually send ~2 mW of 714 nm light to the cavity. An AOM in double pass configuration (see appendix A) is used to offset the frequency of the 714 nm laser beam coupled to the cavity w.r.t. the resonance frequency of the radium atoms in the MOT.

To keep the resonance of the ULE cavity stable over a long period of time it is necessary to maintain a stable separation between the two mirrors. The separation can change mainly due to temperature fluctuations and coupling of mechanical vibrations to the cavity. Also air pressure changes inside the cavity can lead to change in the refractive index of light and change the resonance. To minimize the changes in resonance of the cavity due to these causes, the cavity is housed inside a vibration isolated and temperature controlled steel vacuum chamber. The vacuum chamber is fitted with anti reflection (AR) coated windows for 714 nm light. The pressure in the vacuum chamber is maintained at ~$4.5{\times}10^{-8}$ Torr by continuously pumping it with an ion pump (Gamma Vacuum, 3S-CV-CU-OV-N-N). An aluminum V-shaped holder keeps the cavity in place inside the vacuum chamber. A viton O-ring is used to prevent the aluminum holder from touching the steel surface. The O-ring also helps in dampening mechanical vibrations that reach the cavity. The vacuum chamber and the pump are wrapped with a copper heating wire, and then covered with aluminum foils to evenly distribute the heat. The vacuum chamber is placed on a bakelite frame and mounted on an aluminum platform. To isolate the system from mechanical vibrations the aluminum platform is fitted with rubber feet and mounted

on an optical table. A rectangular copper enclosure covers the setup. Thermal insulating foam is used on both inside and outside wall of the copper enclosure. The following figures (Fig. 5.6, Fig. 5.7, and Fig. 5.8) show the setup.
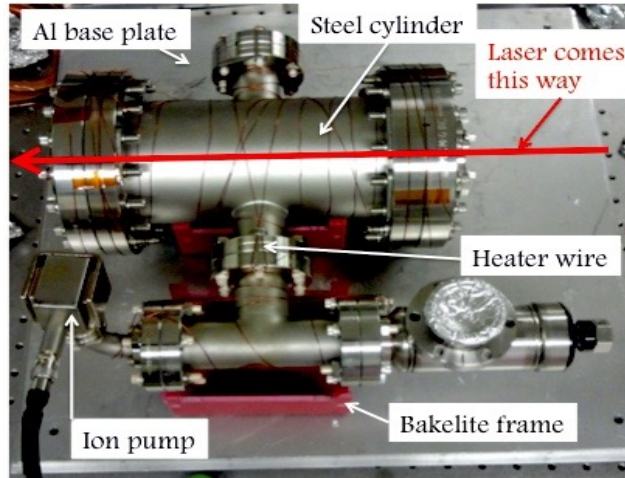
Figure 5.6: Top view of the steel vacuum chamber. The larger flanges on the left and right are 6″ in diameter.
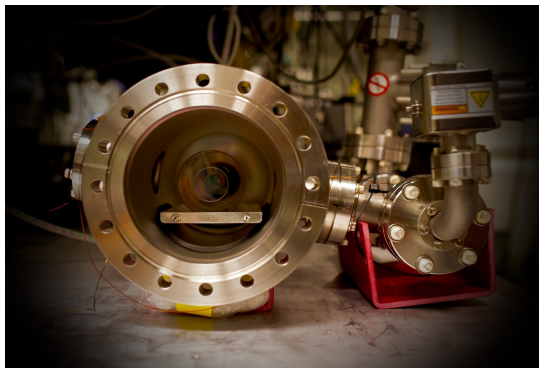
Figure 5.7: The ULE cavity inside the steel vacuum chamber.
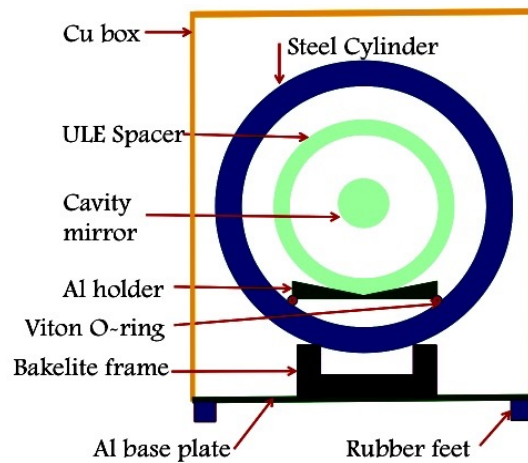
Figure 5.8: Schematic looking directly into the steel cylinder.

47

To minimize the effects of temperature on the cavity resonance, we try to maintain the temperature of the ULE cavity system near a value where the thermal expansion coefficient of ULE glass is lowest. This temperature for our cavity was determined by ATFilms to be $T_c = 32 \pm 1°$C. To maintain the cavity at this temperature a two stage temperature control setup is used.

In the first stage, the temperature of the copper enclosure is stabilized using a commercial diode laser temperature controller (ILXLightwave model: LDT5525). A 100 kΩ thermistor is used as a temperature sensor and two thermoelectric coolers (TECs) in series are used as the heat exchanging elements. The temperature sensor and the TECs are placed on the top surface of the copper enclosure. This arrangement works best for controlling the temperature of the top surface of the enclosure only. Temperature differences of up to 1K (the sensors were not calibrated) are seen with the other surfaces of the copper enclosure. The temperature stabilized copper enclosure provides a relatively stable thermal environment for the steel cylinder compared to the room environment.

In the second stage, the steel cylinder is temperature stabilized using a home built temperature control system. This system can only heat the cylinder and cannot provide cooling. Fig. 5.9 shows an electronic circuit diagram of the temperature sensing and feedback circuit of the temperature control system. This circuit is powered using a bench-top power supply. The 100 kΩ thermistor continuously measures the temperature of the cylinder. The temperature is set by tuning the potentiometer A. Any change in temperature from the set-point causes an imbalance in voltage across the instrumentation amplifier (INA128P) input which then outputs a nonzero voltage. This voltage is amplified and integrated and then sent to the tuning port of an external current supply (HP 3245). The external current supply provides current to the copper heater wire that is wrapped around the steel cylinder and the pump.
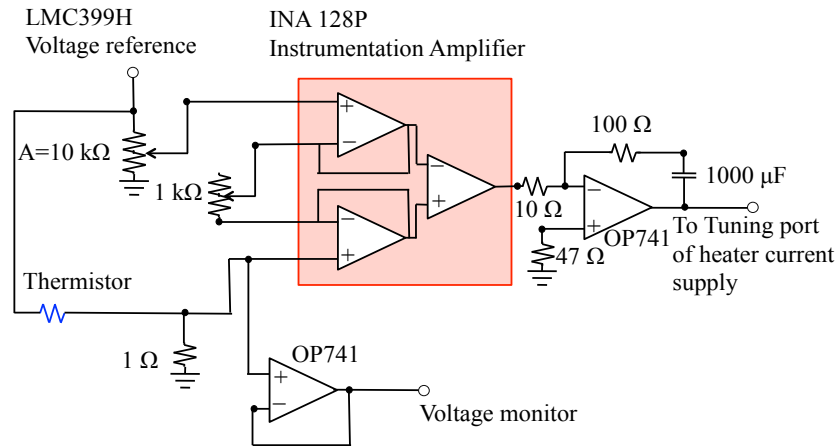
Figure 5.9: Electronic circuit diagram of the temperature sensing and feedback circuit of the temperature control system used for the steel cylinder.

The following figure shows the temperature measured by a thermistor placed at the middle of the cylindrical surface of the chamber. The average temperature is higher than T_c. Data for the plot was taken after the temperature was stabilized.
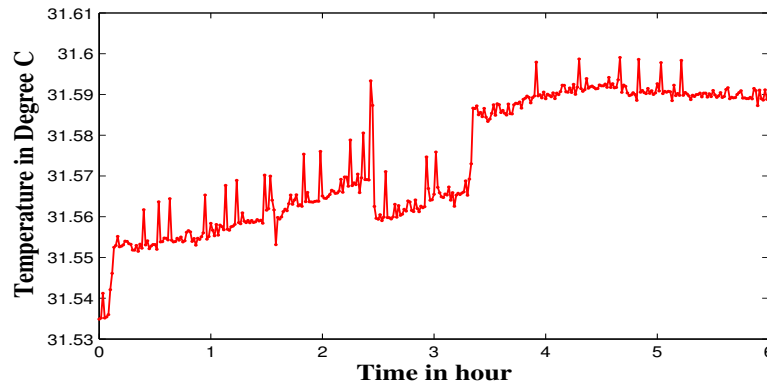
Figure 5.10: Temperature measurements done by the feedback thermistor placed on the middle of the cylindrical surface of the steel chamber. A voltage measurement is converted to temperature. Voltage can spike due to pick up of unwanted signals from other electronic instruments in the lab. The spikes seen in this plot are too fast to be caused due to actual changes in temperature.

5.5.2 Cavity For the 1428 nm and The 966 nm Lasers

The ULE cavity system worked very well for us. Often we could lock the 714 nm laser to the cavity for a whole day without needing any tuning. After using the ULE cavity lock for about a year we changed the laser frequency stabilization systems for the 1428 nm and the 966 nm lasers to cavity based systems. We used a single block of Zerodur glass to make the reference cavities for these two lasers. The following figure shows an engineering drawing of the Zerodur block.
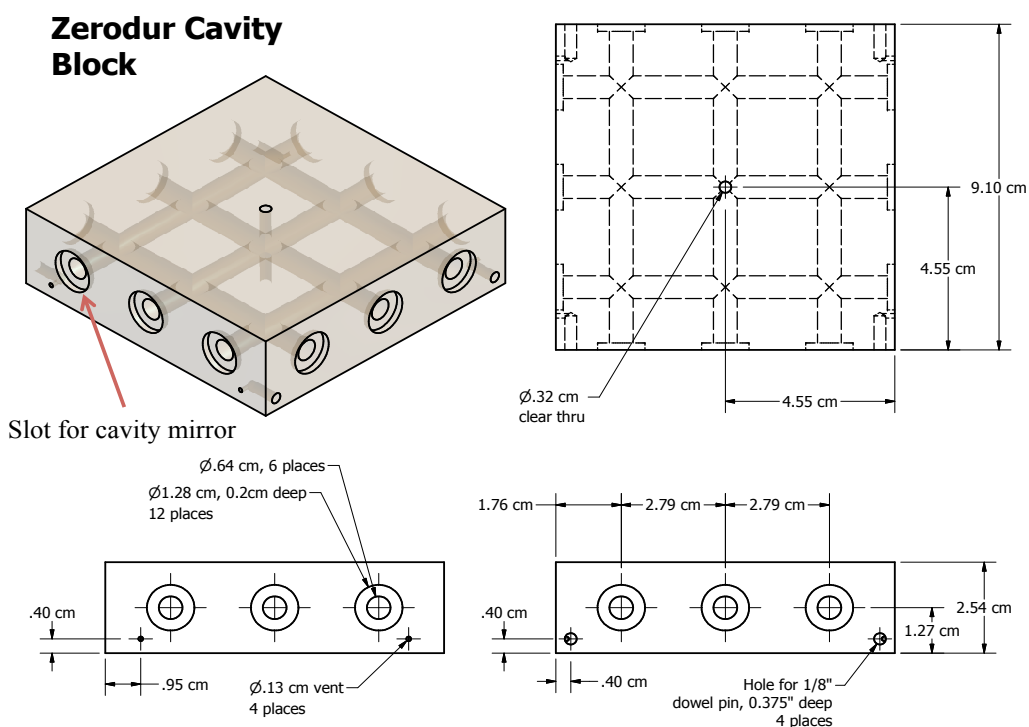
Figure 5.11: Engineering drawing of the Zerodur block that is used to form the spacers for the cavities for the 966 nm and the 1428 nm lasers. The mirrors are secured to the block using stainless steel frames.

The mirrors for the cavity are put in the mirror slots. To secure the mirrors they are pressed against the block using a stainless steel frame. We used 0.5″ diameter

mirrors to make two hemispherical cavities, one for the 966 nm and the other for the 1428 nm laser. The curved mirrors of the two cavities had similar focal length of 10 cm. The Zerodur block is designed to accommodate six different cavities. The block is placed inside a steel vacuum chamber. Plastic dowel pins are used to hold the block inside the chamber to prevent direct contact of the block with the vacuum chamber. An ion pump (Gamma Vacuum, 3S-CV-1V-5K-N-N) continuously pumps the vacuum chamber to maintain a pressure of $\sim 2 \times 10^{-7}$ Torr inside the chamber. The light input port of the chamber is fitted with $1''$ diameter AR coated windows. A Teflon frame presses the windows against the steel surface. Viton O-rings are used to seal the windows. The following figures (Fig. 5.12 and Fig. 5.13) show the Zerodur cavity system.
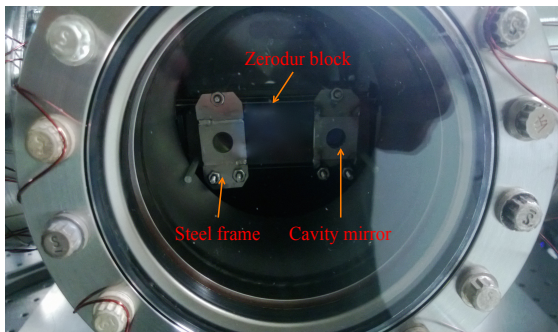
Figure 5.12: The Zerodur cavity inside the steel vacuum chamber. (Looking from the output port).
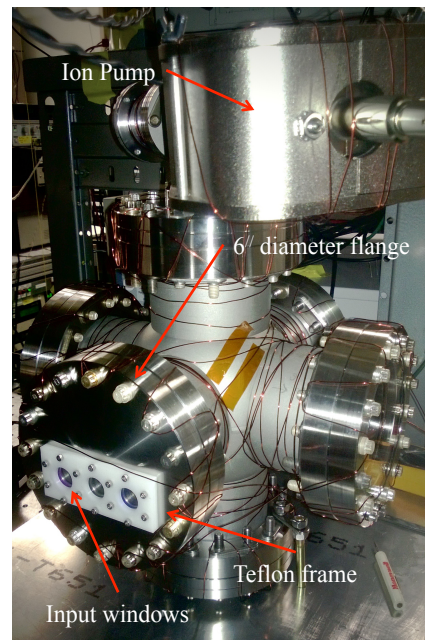
Figure 5.13: The steel vacuum chamber that houses the Zerodur block.

To maintain the cavity at constant temperature, a temperature controller similar to Fig. 5.9 is built. Copper heater coils are wrapped around the vacuum chamber and the chamber is covered with aluminum foils. The vacuum chamber is secured on an aluminum platform. The aluminum platform is mounted on an optical table using rubber feet. This setup is covered with a rectangular enclosure made of thermally insulating foam.

These thermally and mechanically stabilized cavities are used as the frequency references to construct the laser frequency stabilization systems using the PDH method.

5.5.3 The PDH Setup

A general block diagram of the PDH setups that are used for the laser frequency stabilization system is shown in Fig. 5.14.
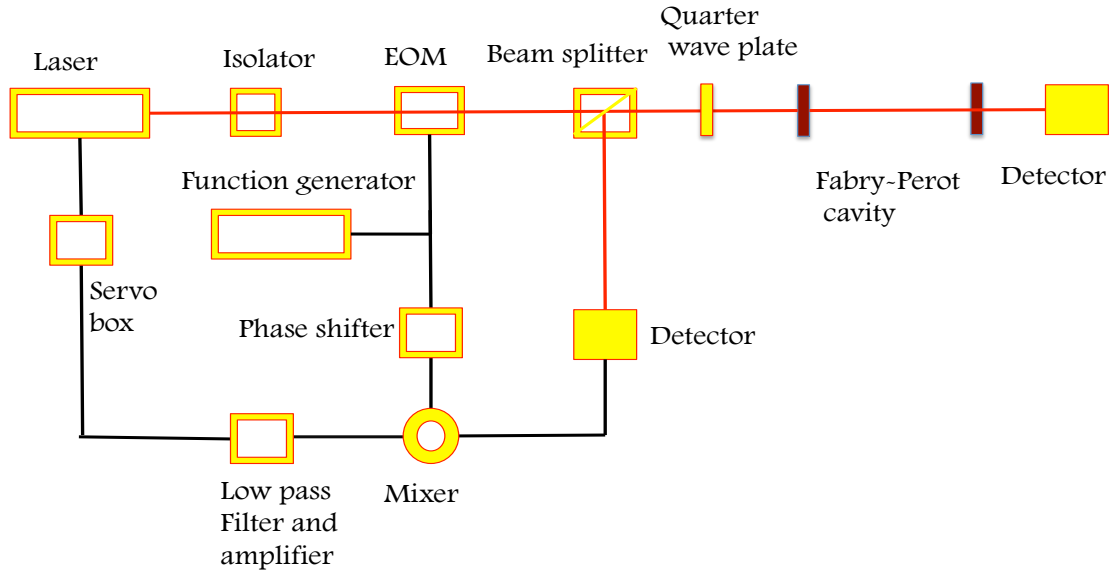
Figure 5.14: Block diagram of the setups used to stabilize the frequency of the 714 nm, the 966 nm, and one of the 1428 nm lasers. The red lines show the laser beam path and the black lines show electronic signal path.

To implement the PDH scheme the laser beam is coupled to a stable Fabry-Perot cavity and the frequency of the laser beam is modulated. To obtain frequency modulation of the laser beam we use Electro-Optic-Modulators (EOMs) which modulate the phase of the laser beam for the 714 nm laser (at 11.6 MHz using Thorlabs EO-PM-NR-C1) and the 1428 nm laser (at 15 MHz using EOSPACE Inc., PM-0K5-10-PFU-PFU-1480-UL). To modulate the frequency of the 966 nm laser we modulate the current of the laser diode by adding an AC component (at 25 MHz) to the diode current. A bias tee (Mini Circuits Laboratories, ZFBT-282-1.5A+) is used to add the AC and the DC currents. This modulation generates sidebands with definite phase relationship to the incident beam and the beam reflected from the cavity. These sidebands are interfered with the reflected beam, the sum displays a beat pattern at the modulation frequency (see appendix B). The optical isolator reduces reflection from the optical elements going back to the laser. As shown in Fig. 5.14 the interfered beam is detected using a photo detector. The detector signal at the modulation frequency is isolated using the mixer and a low pass filter. This generates an error signal for a servo. The output signal from the servo is fed back to the laser's tuning port (a piezo controlled mirror for the Ti:Sapphire laser and the tuning port of the laser diode current supplies for the diode lasers). This arrangement locks the frequency of the laser to a cavity mode. The transmission from the cavity is monitored using a photo detector. As an example, Fig. 5.15 shows an oscilloscope trace of the error signal generated from the 714 nm laser stabilization system. To generate these plots the frequency of the Ti:Sapphire laser is scanned over a cavity resonance. The transmission from the cavity is monitored using a photodiode and displayed on the oscilloscope (the red trace). The two smaller peaks on both side of the larger peaks show the generated sidebands. The blue trace shows the error signal generated from the stabilization system.
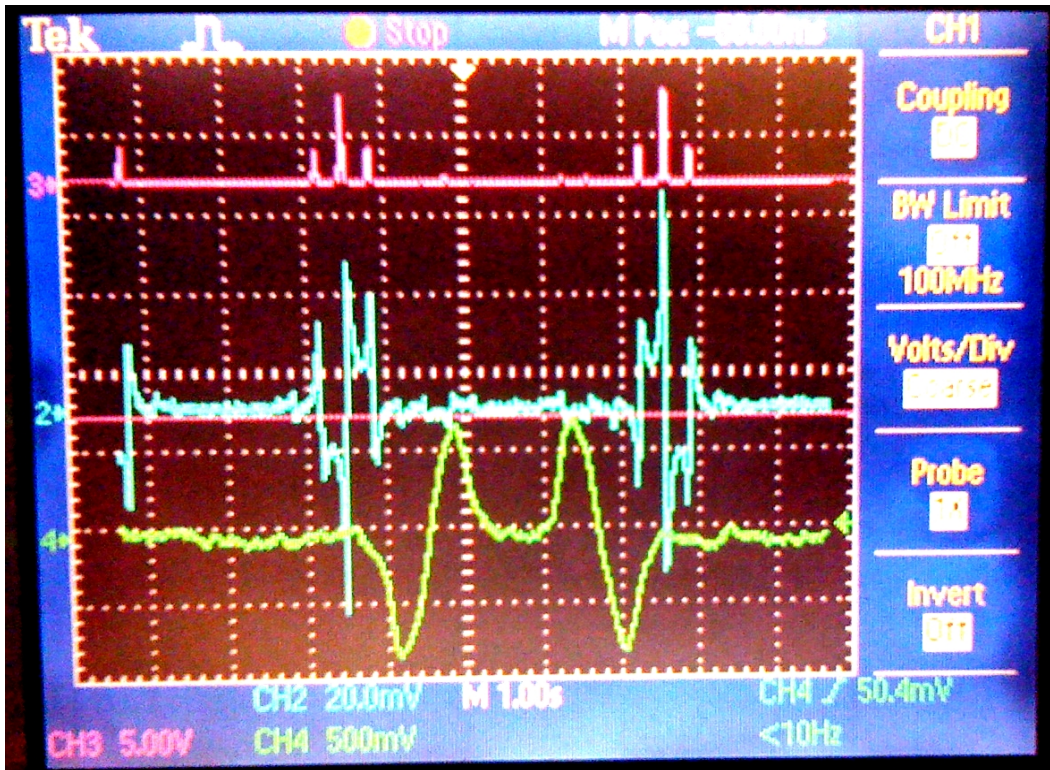
Figure 5.15: Oscilloscope trace showing the error signal (blue) obtained with the ULE cavity. This error signal is the input for the servo loop. The green error signal is obtained from an old stabilization system that used a temperature stabilized Iodine cell as a frequency reference. The red trace shows the sidebands generated at 11.6 MHz.

5.5.4 Long Term Stability of the 714 nm Laser Lock

We observed a long term drift of the resonance of the ULE cavity. The frequency of the offset double pass AOM that brings the 714 nm laser simultaneously to resonance of the ^{226}Ra atoms in the MOT chamber, and to the $TEM_{0,0}$ mode of the cavity was recorded over time. The following figure shows a plot of this set point as a function of time over a period of about 4 years. The ULE cavity resonance has drifted about 10 MHz w.r.t. the resonance of the ^{226}Ra atoms in the MOT in these 4 years.
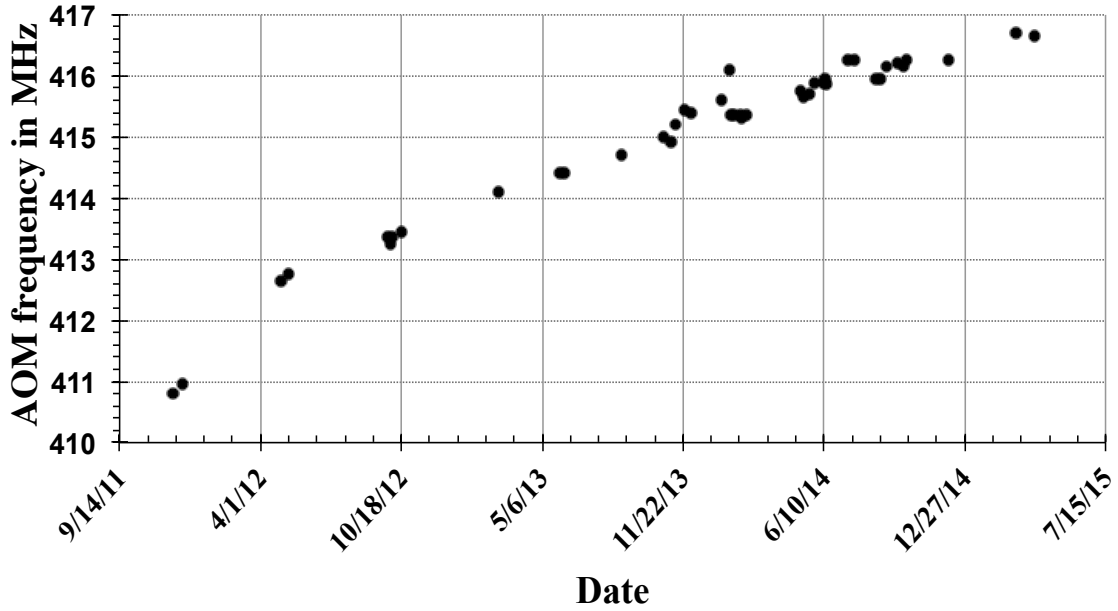
Figure 5.16: Double pass AOM set point frequency needed to bring the 714 nm laser to resonance of the $7s^2\ ^1S_0 \rightarrow 7s7p\ ^3P_1$ transition of ^{226}Ra in the MOT as a function of time. For this transition $\Gamma = 2\pi \times 380$ kHz.

5.5.5 Frequency Stabilization Scheme for the Second 1428 nm Laser

To stabilize the frequency of the second 1428 nm laser to the Zerodur cavity stabilized first 1428 nm laser we followed a scheme described in [95]. The scheme is based on the frequency dependent phase shift experienced by the beat note of two laser frequencies when it propagates through a coaxial cable. Because the time delay introduced by the cable is independent of the frequency, the phase shift is proportional to the beat frequency and it provides an error signal for a servo loop.

We used a single optical setup with two different sets of electronics to build two separate (one to trap ^{226}Ra and the other to trap ^{225}Ra) frequency stabilization systems. Fig. 5.17 and Fig. 5.18 show schematics of the two beat lock systems. The photo detector detects the beat note of frequency $\Delta\nu$, resulting from the interference

55
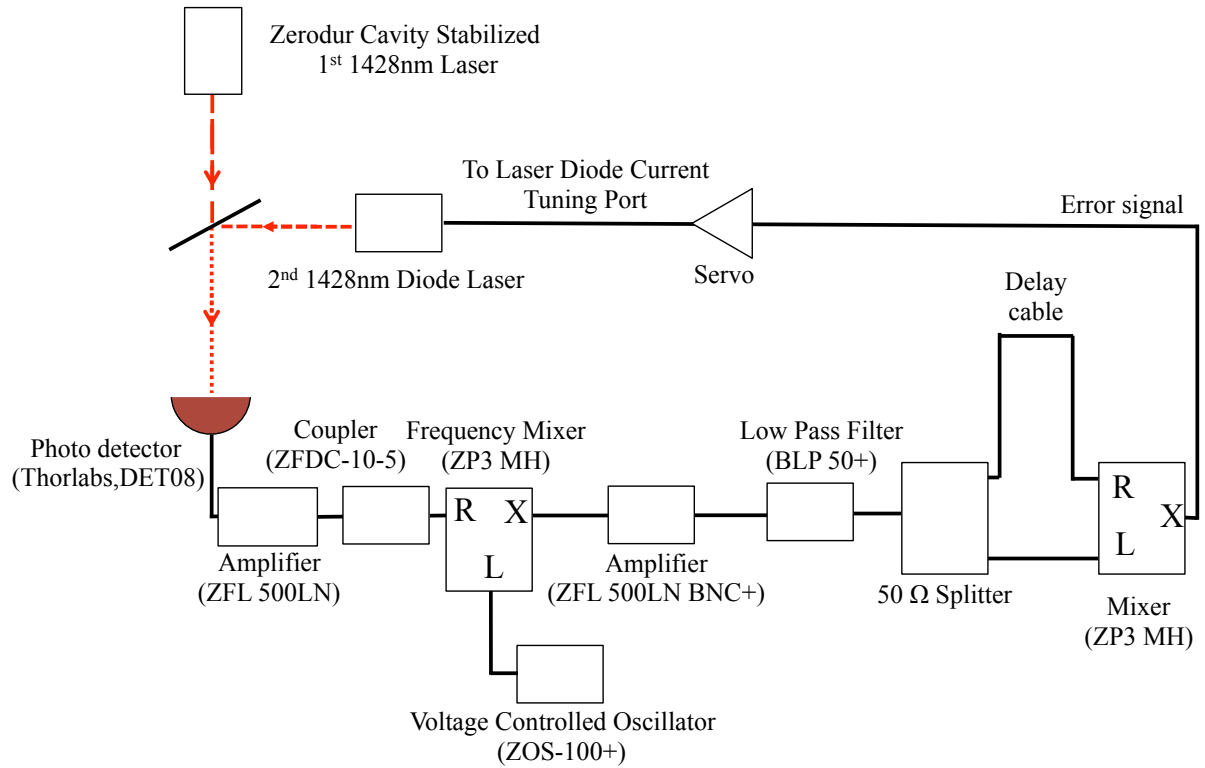
Figure 5.17: Beat locking scheme for the second 1428 nm laser used for experiments with ^{226}Ra. The red arrows represent laser direction and the black lines represent electronic signals. The RF parts were purchased from Mini-Circuits.

of the two 1428 nm lasers. This beat note signal is amplified and mixed with an RF signal of frequency ν_{VCO} from a voltage controlled oscillator (VCO). The difference signal (between $\Delta\nu$ and ν_{VCO}) output from the mixer is split. One part of the split signal is sent through a delay cable and mixed with the other part of the split signal in a mixer. The output of the mixer is the error signal which varies as $\cos\phi$, where the phase shift ϕ introduced by the cable is given by $\phi = 2\pi(\Delta\nu - \nu_{VCO})\tau$, τ is the time delay introduced by the cable. This error signal is sent to a servo. The output of the servo is sent to the current tuning port of the laser diode current supply for

the second 1428 nm laser. This feedback loop keeps the difference between the beat note frequency $\Delta\nu$, and the VCO frequency ν_{VCO} constant. By changing the VCO frequency ν_{VCO}, the locking point of the second 1428 nm laser can be tuned.
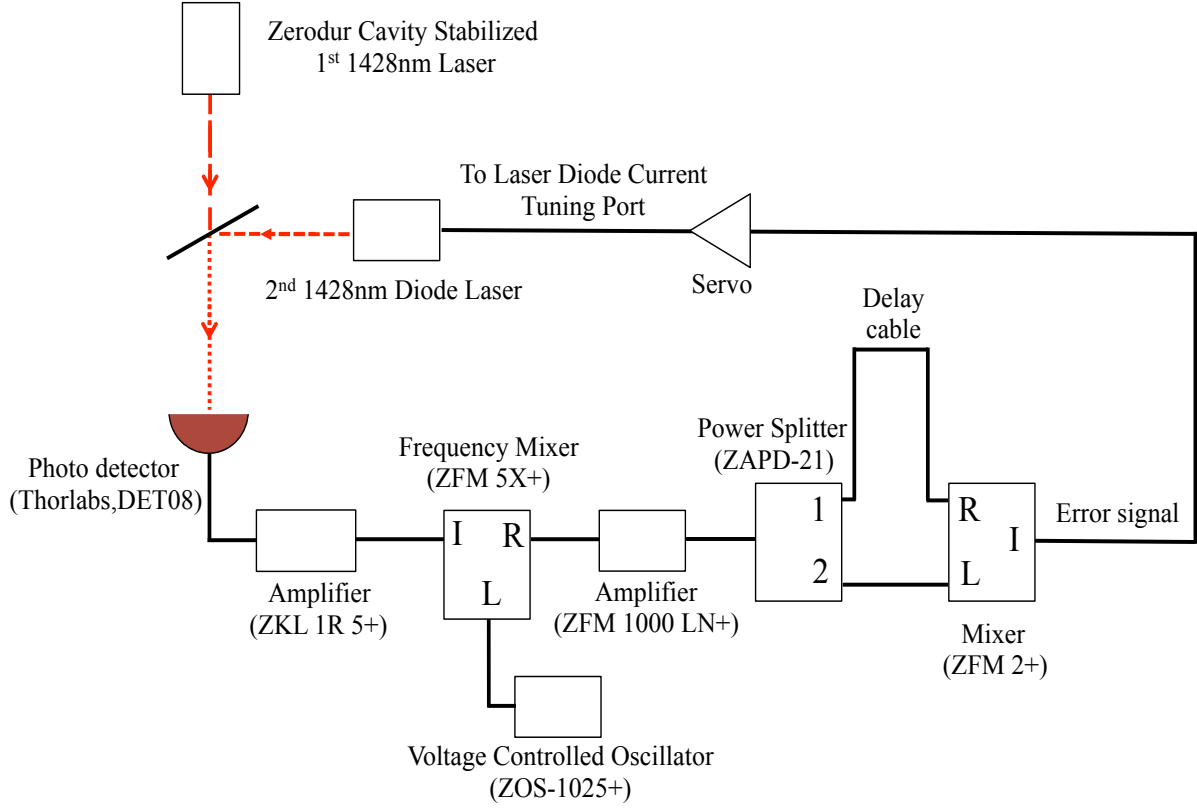
Figure 5.18: Beat locking scheme for the second 1428 nm laser used for experiments with ^{225}Ra.

5.6 Generation of the Electric Field

The electric field necessary for the EDM experiment is generated in a 2.3 ± 0.1 mm gap between a pair of copper electrodes held parallel in vacuum inside the glass tube.

As we see from eq. 1.12 that the sensitivity of an EDM experiment increases with increase in the applied E field. In order to generate the high E field we built an electric field generating system. The large electric field creates a DC stark shift of the atoms. The DC stark shift is not known experimentally. The theory calculations suggest a shift of 64 KHz/(kV/cm)^2 for the ground state of radium. A gradient of the E field can lead to a position dependent stark shift of the atoms generating a force. The atoms in the experimental region are trapped in a weak potential of depth of the order of 500 μK created by the standing wave ODT. Therefore, in order to keep the atoms in the trap the electric field gradient has to be less than 10%/mm, which is easily achieved. If the E field is ramped up after the atoms are loaded into the trap a field gradient can also move the atoms in the trap. A leakage current flowing through the gap will create an E field dependent B field. This can cause EDM like effects by a change in precession frequency that depends on the direction of E field. A conservative estimate indicate that to reach an EDM sensitivity of 10^{-26} e·cm this current should be less than 80 pA.

In order to generate the necessary E field, one of the electrodes is connected to a high voltage (HV) system and the other electrode is connected to a current measuring circuit. The electrodes were designed to maximize field homogeneity in the horizontal plane and to avoid field enhancement due to sharp corners. The electrodes were electropolished (by ABLE Electropolishing). To minimize sparking at HV, the electrodes were conditioned. The conditioning procedure involved gradually ramping the voltage on one electrode and measuring the current on the other electrode. When a spark was observed the voltage was ramped down to a lower value. After keeping the voltage at this lower value for a fixed time (of the order of 10s of minutes) the voltage was ramped up again to a higher value. We kept on increasing the voltage until we observe a spark. On observing a spark the voltage was ramped down again. The

procedure was repeated until the sparks appear at higher and higher voltages. Our conditioned electrodes were able to hold an E field of 100 kV/cm without sparking. The gap between the electrodes was measured in situ and the measurement technique is described in a later section. Two 1 m long copper rods connect the two electrodes to two separate copper feedthroughs connected to two adjacent faces of the six way cube at the end of the glass tube (Fig. 5.1). The feedthroughs were specially designed to avoid sharp edges. Fig. 5.19 shows an engineering drawing of the copper electrodes and Fig. 5.20 shows an image of one of the HV feedthroughs.
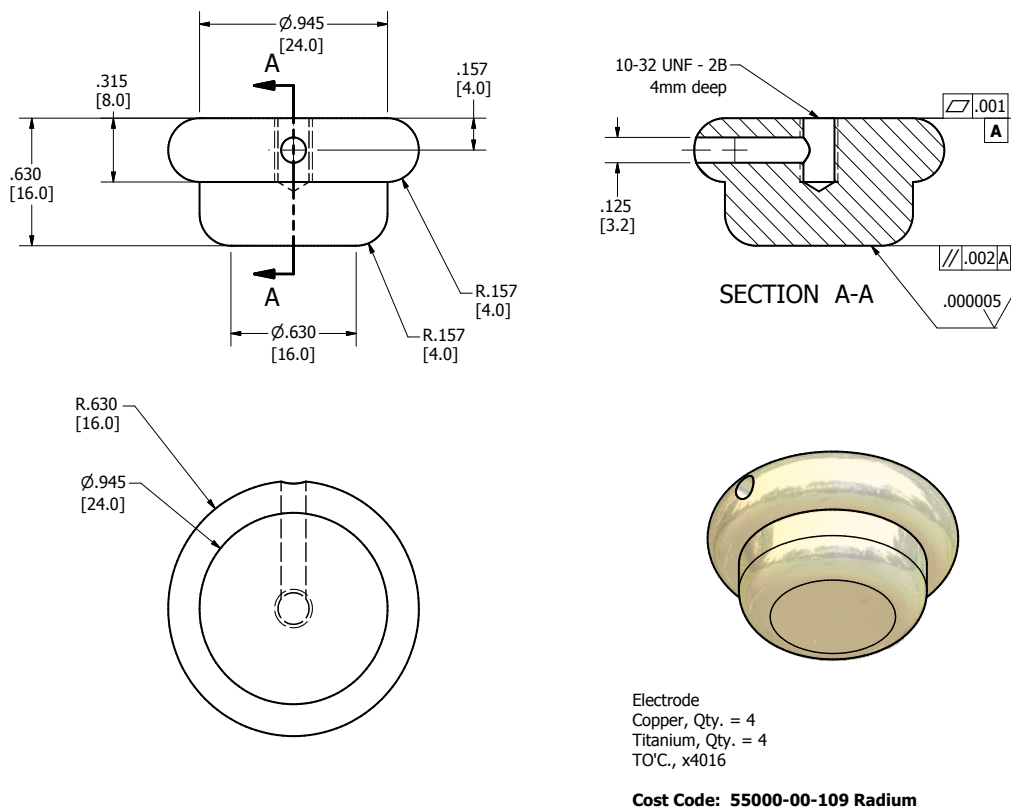
Figure 5.19: Engineering drawing of the copper electrodes.

59
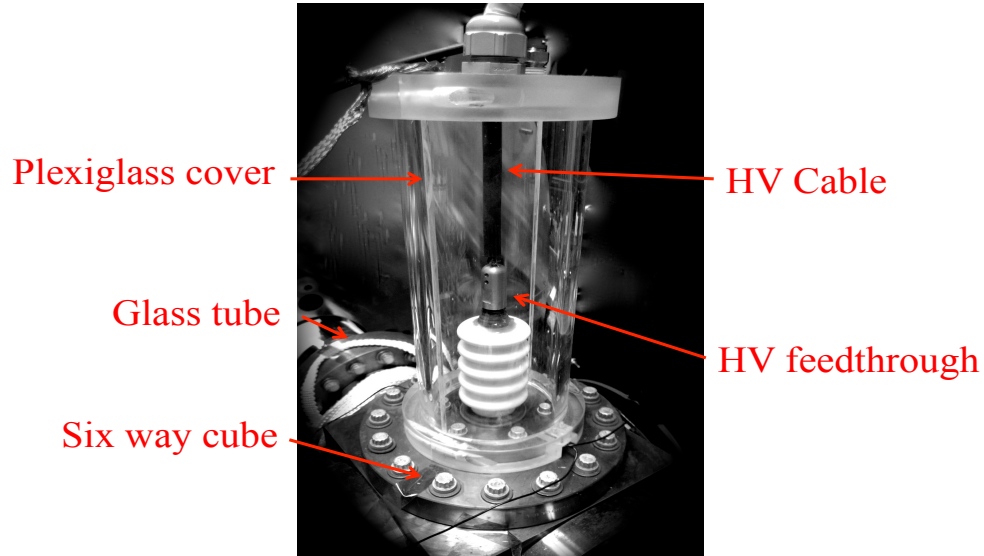
Figure 5.20: Picture of one of the HV feedthroughs connected to a six way cube with 10″ diameter flanges located at the end of the glass tube (see also Fig. 5.1).

Fig. 5.21 and Fig. 5.22 show an engineering drawing and a photo of the electrode setup.
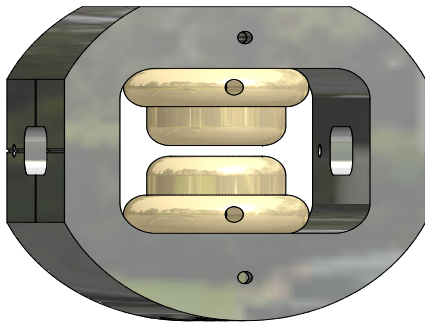
Figure 5.21: Engineering drawing of the copper electrodes in their macor holder.
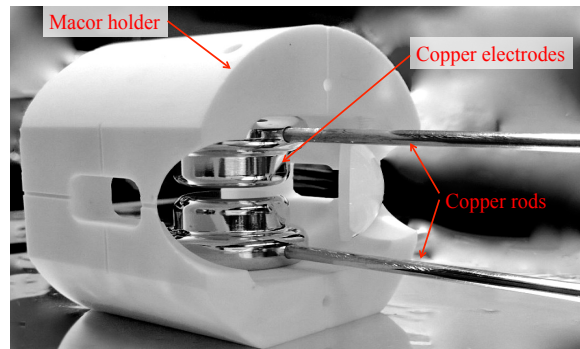
Figure 5.22: Photo of the electrodes in their macor holder.

During the EDM experimental run, the bottom electrode was connected to the

60

high voltage (HV) system and the top electrode was connected to the current measuring circuit via the copper feedthroughs. The connections to the feedthroughs were covered by plexiglass enclosures. 25 feet long shielded co-axial cables (Claymont, Model: Mammoflex M1 type) were used to make the connections to the feedthroughs.

Fig. 5.23 shows a circuit diagram of the HV system.
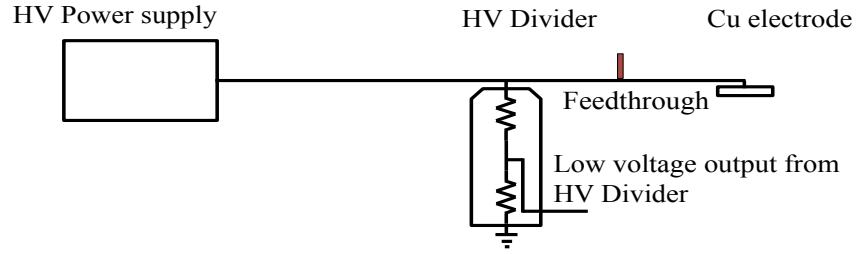
Figure 5.23: Circuit diagram of the HV system.

The HV system consists of a commercial HV power supply (Spellman HV, Model: CZE 2000) and a precision HV divider (Ross engineering, Model: V30-8.3-A). The HV divider is used to measure the output of the HV power supply. The current flowing to the other electrode, not connected to the HV system, is measured using a current to voltage converter circuit. These components are housed inside a $60'' \times 24'' \times 24''$ sized grounded aluminum box. The size of the box was determined by the consideration of maintaining a minimum separation of 2 cm/kV between exposed components at HV and the ground. The door of the aluminum box is interlocked to a +24 VDC power supply that powers the HV power supply. The HV power supply is controlled and monitored by using a DAQ card (National Instruments, PCI-MIO-16E4) installed in a Windows 7 computer. The same DAQ card is also used to monitor the low voltage output of the HV divider and the output voltage of the current measuring circuit. The DAQ card is programmed using a LabVIEW program. The output polarity of the HV power supply is controlled by using an

external TTL signal. The output voltage (0 to a maximum of ± 30 kVDC) of the HV power supply is controlled by a $0 \rightarrow 10$ VDC control signal applied from one of the analog output ports of the DAQ card. During the EDM experiment this control signal is triggered by using an external TTL signal. Two separate $0 \rightarrow 10$ VDC output signals from the HV power supply act as full scale voltage and current monitor signals. These signals are monitored and recorded using the analog input port of the DAQ card. Analog isolation amplifier (Bur-Brown, Model: ISO122JP) circuits are used to galvanically isolate, control and, monitor signals between the HV power supply and the DAQ card. During the EDM experiment the bottom electrode was ramped to a set HV in a 1/e time of 90 ms. The same control signal was used to the ramp voltage to positive and negative HV resulting in voltages of -15.598 ± 0.001 kV for the negative HV and $+15.488 \pm 0.009$ kV for the positive HV. The difference between negative and positive HV was <0.7%.

The current measuring circuit consists of a current to voltage converter circuit, constructed using an ultra low input current opamp (Texas Instruments, LMC6001). This circuit is similar to a circuit used in ref.[7]. To protect this circuit when a spark happens between the components at HV and the ground, several methods were tried. These methods included use of Zehner diodes, transient voltage suppressor diodes, charge arresters, transistors, and RF chokes. However, all these methods failed to protect the opamp during sparking. Therefore, we had to replace the opamp after every spark. After the electrodes were conditioned in the EDM setup, the frequency of sparking reduced (no sparks were detected after September 2014 and during the EDM experimental runs in October and December of 2014 for E fields of up to 67 kV/cm). Fig. 5.24 shows a circuit diagram of the current to voltage converter circuit. The current measured by this circuit is found to be <80 pA after the bottom electrode was ramped to ± 15.5 kV.
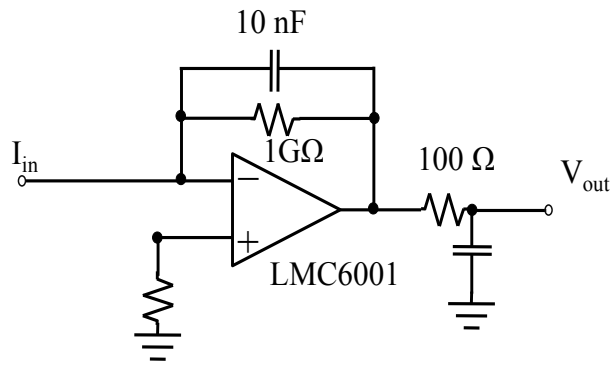
Figure 5.24: The current measurement circuit. The opamp has ultra low input leakage current rating ($<$ 25 fA). The circuit is powered by a $\pm$ 6 V battery pack.

The current measurement circuit is powered by a $\pm$ 6V battery pack. The battery pack and the circuit are housed inside the grounded aluminum box. Fig. 5.25 shows a photo of the grounded aluminum box including the components inside it.
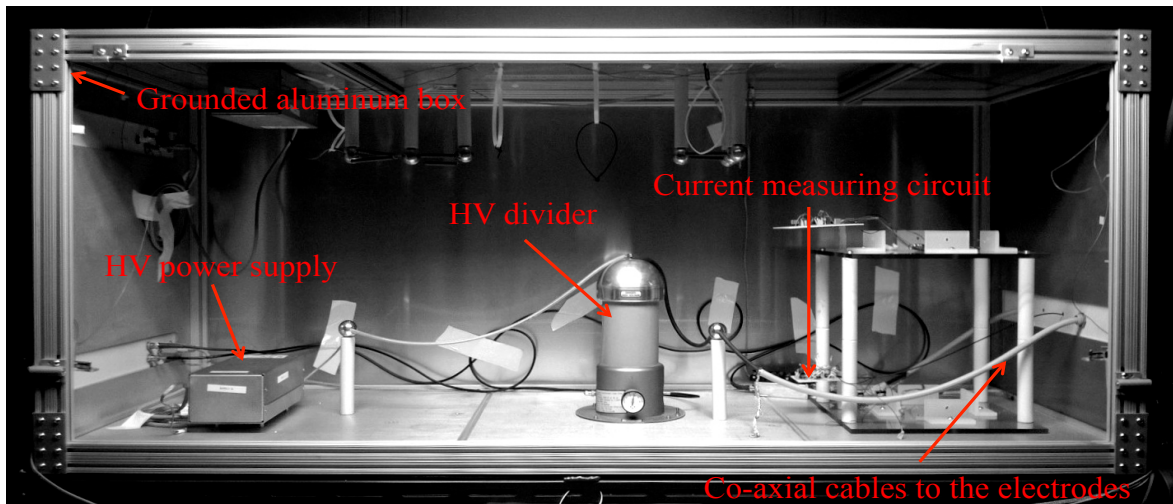
Figure 5.25: Picture of the HV system, brass balls with screws were used to make connections in order to avoid sharp edges of exposed parts at HV. The grounded Al box is designed to maintain a minimum distance of 2 cm/kV between the parts at HV and the ground.

63

5.7 Measuring the Gap Between the Electrodes

In order to know the E field we need to know the separation between the electrodes. The HV applied to the electrodes is measured by the voltage divider. The gap between the copper electrodes was measured in-situ in the EDM setup. Fig. 5.26 illustrates the arrangement that we had used to measure the gap.
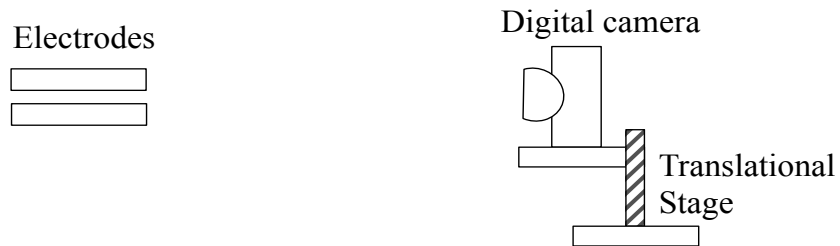
Figure 5.26: The arrangement of the setup that was used to measure the gap between the electrodes in-situ.
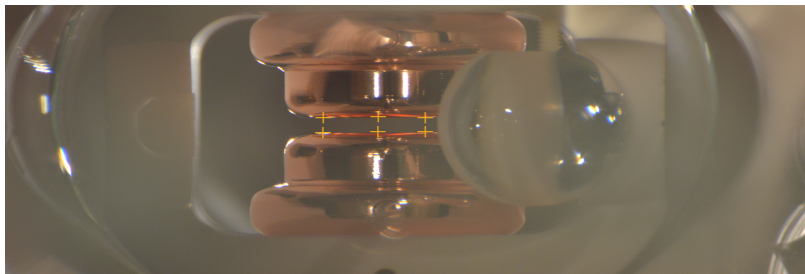
Figure 5.27: Image of the gap taken using a digital camera looking along the glass tube axis through a window on the six way cube. The crosses show approximate location of the focussing points.

A digital camera fitted with a zoom lens was used to obtain a live image (Fig. 5.27) of the gap. The camera images along the glass tube through a window on the six-way cube. To measure the gap, first the camera was focussed to the edge of one of the electrodes. The angle of the translational stage was adjusted to make sure

that the camera images the electrode parallel to its flat surface. After this step a cross hair on the camera's live display panel is fixed to an edge on the electrode. The reading on the translational stage is recorded. This is the first position of the camera. The translational stage is then moved vertically until the cross hair aligns with the edge of the second electrode. The reading on the translational stage is recorded. This is the second position of the electrode. The difference between the first position of the camera and the second position of the camera gives the measurement of the gap. The gap was measured at three different places on the set of electrodes. These numbers were averaged to obtain the gap between the electrodes. To test this method we measured the gap in a test electrode setup and compared the results with a measurement of the same gap done with an optical comparator. These two results agree within < 1 % of each other. Using this method we measured the gap between the electrodes used in the EDM experiment to be 2.276 ± 0.025 mm. Based on this measurement a conservative estimate of 2.3 ± 0.1 mm is used for the final EDM calculations. This results in 4% uncertainty in the E field.

5.8 Generation of the Magnetic Field

For the EDM experiment we need a stable and uniform B field. The B field is generated by using a cosine-theta coil wound on an aluminum cylinder of 0.32 m in diameter and 0.65 m in length. The current in the cosine-theta coil follows a cosine-theta distribution, where theta is the angle with the vertical direction. A photo of the coil is shown in Fig. 5.28.

The coil is powered by a stable power supply during the EDM experimental run. During the first run of the experiment in October we used a power supply that was made by the authors of ref. [27]. The output current of that supply is limited to
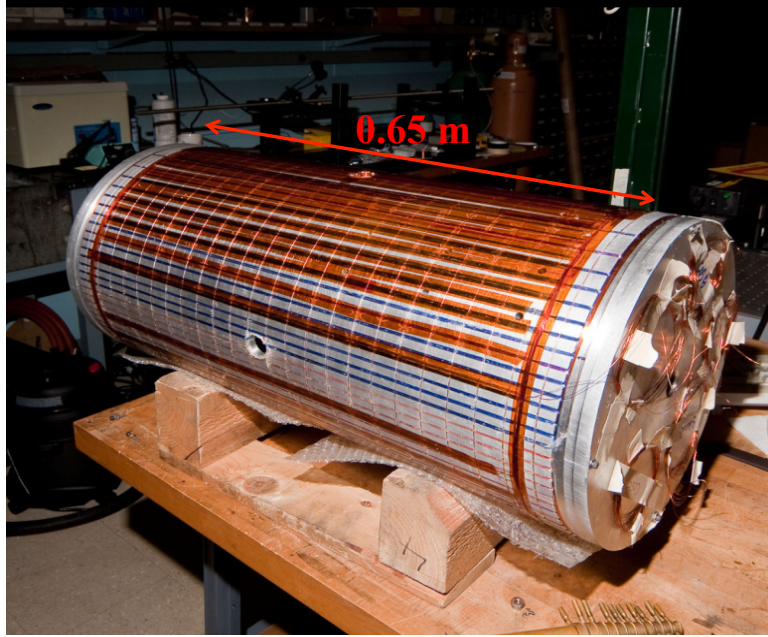
Figure 5.28: Image of the cosine-theta coil wound on an aluminum cylinder.

15 mA. We decided to use a lager magnetic field during the experimental run in December. During this run we used a commercial laser diode power supply (ILX Lightwave LDC3724B) to power the coil. The current between these runs was varied between 15-30 mA. A sufficiently large noise of the current supply generating the B field can hide the EDM signal. For example, if we want to do an EDM measurement at the sensitivity of 1×10^{-25} e·cm with a I= 30 mA current source, then on average $\Delta I/I$ has to be better than 10^{-7}. The following plots show the output of the current supplies as a function of time and the corresponding Allan deviation analysis. $\Delta I/I$ for the 30 mA current supply that we used in December is found to be $<3\times10^{-6}$ when averaged over 50 s. However, at this stage of the experiment we are not limited by noise of the current supply. Analysis of the output of the current supplies are shown in figures Fig. 5.29 to Fig. 5.32.

66
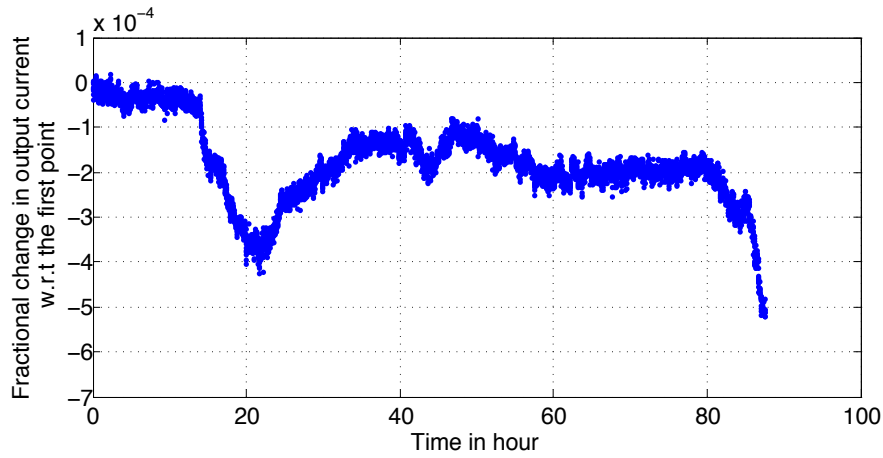
Figure 5.29: Fractional change of the output current of the power supply (with respect to the first point in the graph= 16.2194 mA) used in the experimental run in October as a function of time.
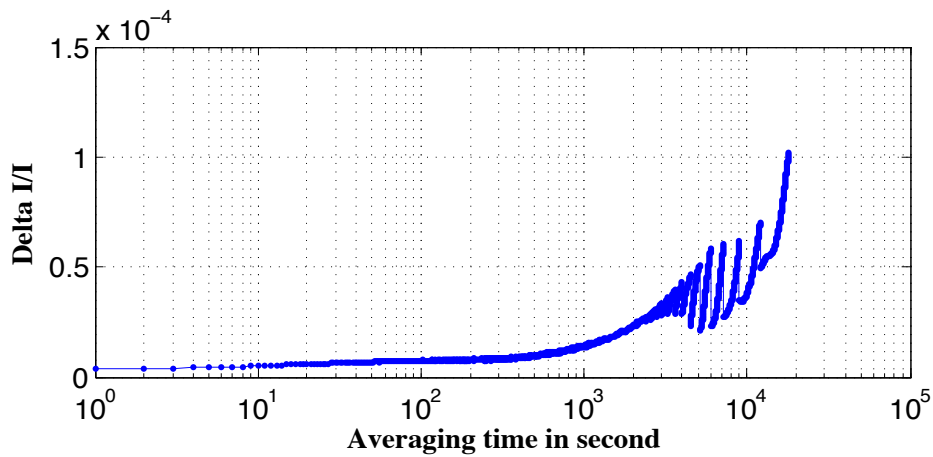
Figure 5.30: Allan deviation of the output current of the power supply used in the experimental run in October.

During the EDM experimental runs no magnetometers were present to measure the magnetic field in the experimental region. The magnetic field inside the shields, generated by the cosine-theta coil was tested using a Rb magnetometer [58]. For

67
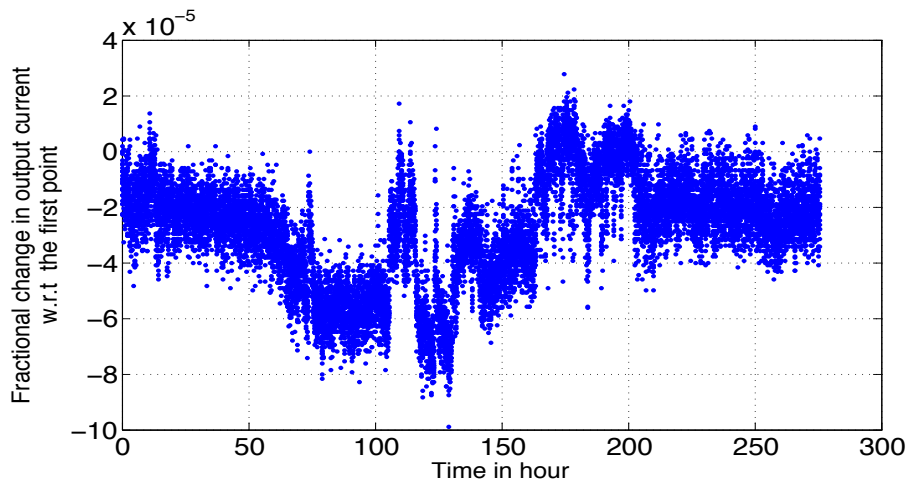
Figure 5.31: Fractional change of the output current of the LDC3724B power supply (with respect to the first point in the graph= 29.94233 mA) used in the experimental run in December as a function of time.
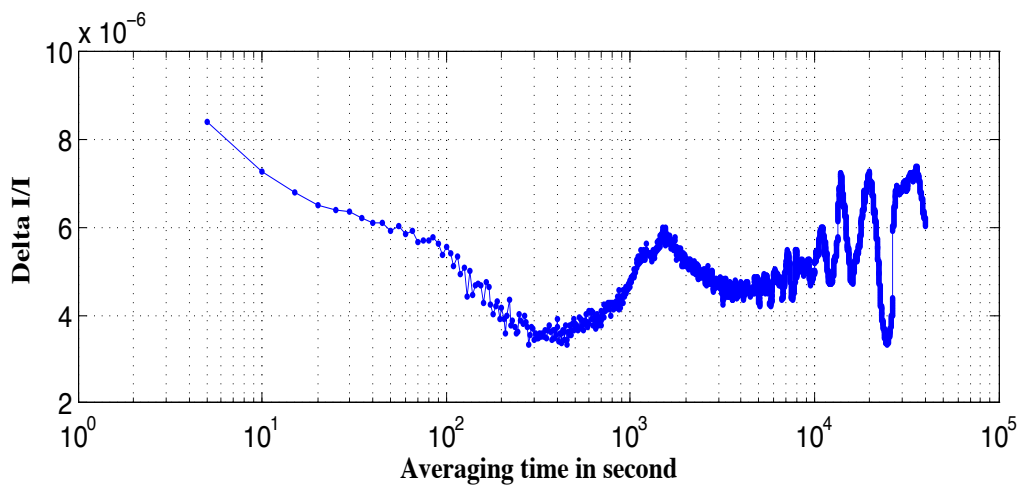
Figure 5.32: Allan deviation of the output current of the ILXLightwave LDC3724B power supply used in the experimental run in December.

these tests the cosine-theta coil was powered by the current supply that was used in October. The instability was measured to be <0.01% when averaged over a measure-

ment cycle of 50 s. The spatial variation of the field was measured by a Hall probe to be <1%/cm. The atoms are held in region of volume $\sim100\mu$m$\times100\mu$m$\times100\mu$m.

5.9   The Experimental Region

The EDM experiment is performed in the gap between the copper electrodes inside the glass tube. This region is surrounded by three layers of μ-metal shields. A photo of the EDM experimental region is shown in Fig. 5.33. To take the photo the ends caps were taken off.
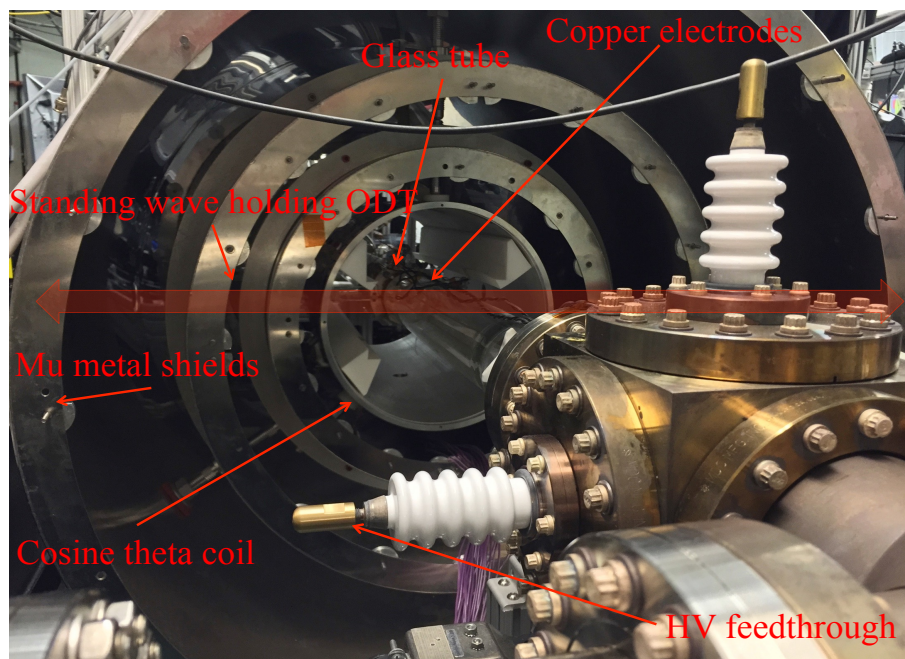
Figure 5.33: The EDM experimental region surrounded by three layers of μ-metal shields. The EDM experiment takes place inside the glass tube.

1″ diameter holes on the left and right side of the shields (Fig. 5.33) allow the access for the 1550 nm laser to form the standing wave holding ODT, and the 483 nm laser to polarize and detect the polarization of the atoms.

The shields were degaussed before the EDM experimental runs by sending a 50 Hz AC current of exponentially decaying amplitude from a bipolar power supply, and through a degaussing coil. The control voltage to the power supply was sent from the output channel of a DAQ card controlled by a LabVIEW program. The degaussing coil surrounds the three layers of shields. After degaussing, the degaussing coils were disconnected from the power supply. These shields reduce external magnetic fields by a factor of 2×10^4 when measured in the vertical direction. An Allan deviation plot of the magnetic field in the vertical direction inside the shields without the B field of the cosine-theta coil is shown in Fig. 5.34. The B field was measured using a fluxgate magnetometer.
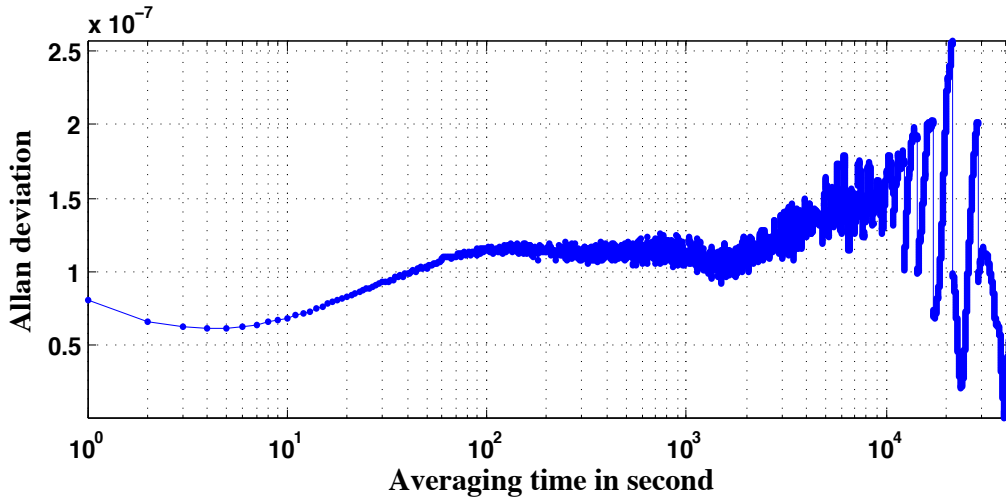
Figure 5.34: Allan deviation plot of the magnetic field in the vertical direction inside the shields without application of the B field due to the cosine-theta coil.

The stability of the B field inside the shields without any applied field was found to be $< 1 \times 10^{-7}$ when averaged over 50 s (based on Allan deviation analysis at 50 s). The stability of the B fields are expected to be of similar order of magnitude in the horizontal direction. Since we polarize the atoms transverse to a relatively stronger

70

vertical B field (of magnitude 15 mG to 30 mG) the EDM experiment is insensitive to the instabilities in the horizontal direction. Instabilities in the horizontal direction will only affect the contrast of the precession signal and will not affect the frequency of precession.

Chapter 6 The Experiment

Using the techniques described in the previous chapter we transported the atoms from the oven to a standing wave ODT placed between the high-voltage (HV) electrodes in the experimental region. Fig. 6.1 shows an engineering drawing of the radium EDM apparatus, highlighting some of the components relevant for the discussions in this chapter. In this chapter I discuss the methods that we had used to manipulate the radium atoms in our experiment.
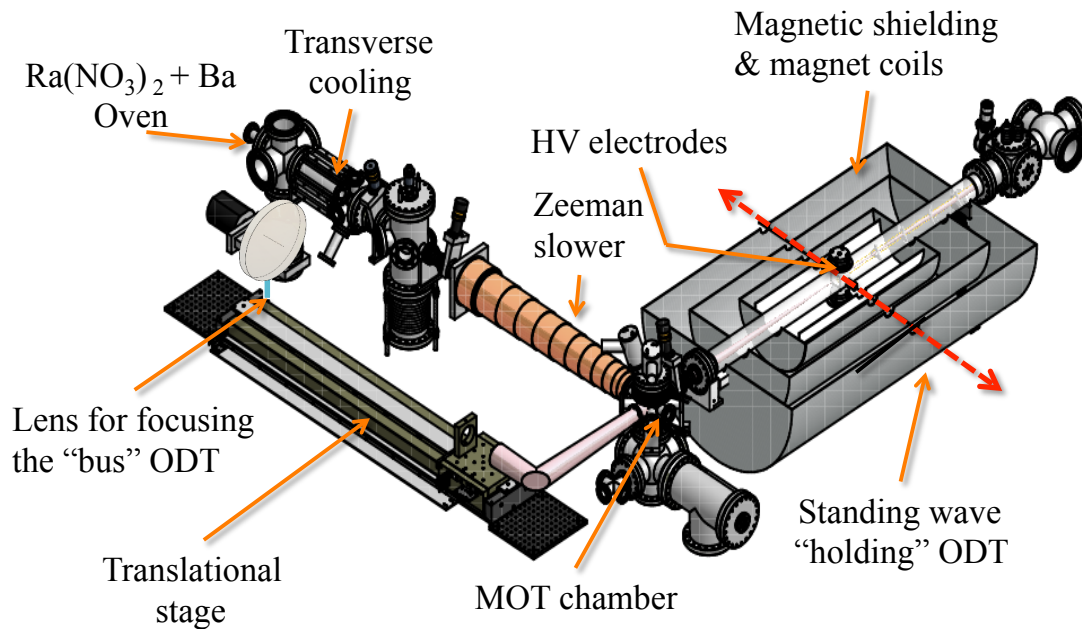
Figure 6.1: Engineering drawing of the radium EDM apparatus. The Zeeman slower is 1 m long. The lens has a focal length of 2 m. The distance from the center of the MOT chamber to the middle of the gap between the HV electrodes is 1 m.

6.1 Transporting Radium Atoms From the Oven to the Experimental Region

The effusive oven is typically heated to about $(450\text{-}550)°$C. This results in a hot atomic beam coming out of the oven. This atomic beam is first collimated (using laser cooling in transverse direction), slowed (using the Zeeman slower) and collected (in the MOT). The details of slowing of the atomic beam and capturing of the slowed radium atoms are discussed in previous publications from our group in references [53], [**Sulai**], and [77]. Some parts of this chapter are based on materials published in these references. The electronic transitions used in our experiment to manipulate the radium atoms are again shown in Fig .6.2 for easier reference.

For laser cooling along the transverse direction and trapping the atoms in the MOT, the 7s^2 $^1S_0$ →7p $^3P_1$ intercombination transition is used at 714 nm ($\Gamma = 2\pi\times380$ kHz [96], I_{sat}=140 μW/cm^2). For ^{226}Ra we excite along $(J = 0)\rightarrow(J' = 1)$ and for ^{225}Ra we excite along $(F = 1/2)\rightarrow(F' = 3/2)$. Measurements done with ^{226}Ra atoms indicate that the transverse cooling stage provides a gain of $\sim(70\text{-}80)$ in the trapping efficiency of the atoms in the MOT.

The 7s^2 $^1S_0$ →7p $^3P_1$ intercombination transition that is used to form the MOT of the radium atoms is weak compared to the E1 transitions typically used in laser cooling and trapping experiments. However, this intercombination transition in radium is nearly closed with a branching ratio of 4×10^{-5} leaking to 7s6d $^3D_1$ [21, 36]. Atoms in the 7s6d $^3D_1$ are repumped to the the 7s7p $^1P_1$ level (with the 1429 nm laser) which quickly decays back to the 7s^2 $^1S_0$ ground state. Two 1429 nm repump lasers are used. One repump laser beam is sent along the Zeeman slower axis and the other repump laser beam is sent to the atoms in the MOT from the top of the MOT chamber along the vertical axis. Due to weakness of the laser force in the inter-
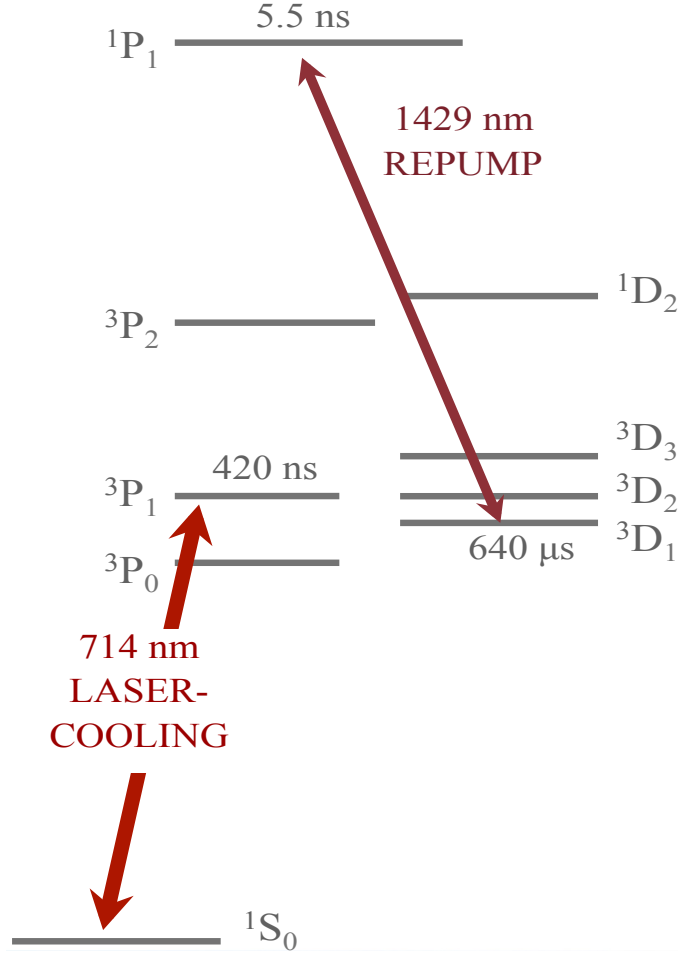
Figure 6.2: Electronic energy level diagram of radium, showing the electronic transitions that are used to laser cool and trap the neutral radium atoms. The lifetime of the relevant atomic states are also shown. (This figure is similar to fig.3.2)

combination transition the trapping efficiency of the radium atoms from the oven to the MOT is only 1×10^{-6}. Typically 10^5 ^{226}Ra and 10^3 ^{225}Ra atoms are accumulated over the MOT lifetime of 40 s and cooled to 40 ± 15 μK.

The atoms in the MOT are imaged by collecting the 714 nm fluorescence light from the atom cloud. A 10 cm focal length lens placed inside the vacuum system and

10 cm away from the center of the MOT chamber (with numerical aperture of 0.009) focusses the fluorescence light onto a charge coupled device (CCD) camera (Andor, Luca). The camera is controlled and the data from the camera is processed using a LabVIEW program. The data from the CCD camera is converted in the LabVIEW program to a matrix form. The element number in the matrix represents the pixel number in the camera. The value of each element represents the analog to digital converter (ADC) counts in each pixel proportional to the intensity of light falling on that pixel. The data is displayed in a 2D color plot to form the image of the atoms. The brighter color represents more intensity and the darker color represents less intensity of light. Typical images of the cloud of ^{226}Ra and ^{225}Ra atoms captured in the MOT are shown in Fig. 6.3 and Fig. 6.4. As already mentioned we use and trap a factor of ∼100 less number of ^{225}Ra atoms compared to ^{226}Ra atoms. Therefore, when we take images of the ^{225}Ra atoms, we usually turn on the bus ODT and use a longer exposure time of the camera in order to improve the signal to noise (SNR).
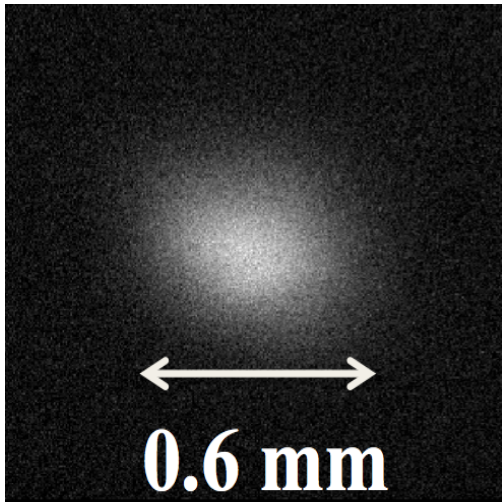
Figure 6.3: Typical image of a cloud of ^{226}Ra atoms in the MOT.
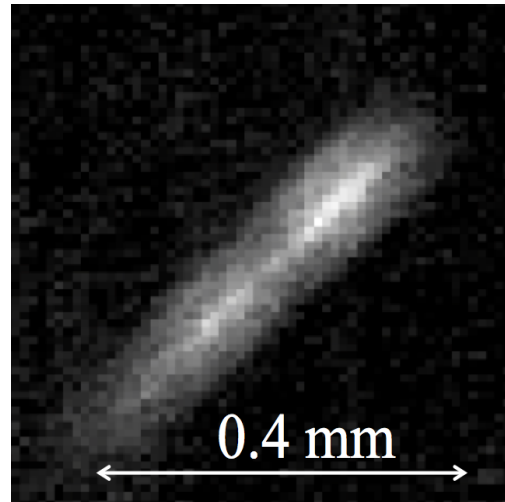
Figure 6.4: Typical image of a cloud of ^{225}Ra atoms in the MOT+ODT.

We divide the MOT part of the experiment into a loading phase (for transferring atoms from the atomic beam to the MOT), a probing phase (for diagnostic imaging of the MOT), and a cooling phase (for transferring the atoms from the MOT to the ODT). To improve the overall efficiency of the trap and transfer atoms from the MOT to the ODT we optimize each phase independently. During the loading phase the laser intensity is typically 1.7 mW/cm^2, the detuning is 2.8 MHz to the red of resonance and the magnetic field gradient is 1 G/cm. During the probing phase the laser intensity is decreased to typically 500 μW/cm^2, the detuning is decreased to 2 MHz and the magnetic field gradient is increased to 2.5 G/cm. During the cooling phase the laser intensity is further decreased to typically 40 μW/cm^2 and the detuning from resonance is decreased to 1.1 MHz, with no change in the magnetic field gradient.

During the cooling phase the atoms from the MOT are transferred to a horizontal traveling wave ODT (referred as the "bus" ODT). This bus ODT is formed by the 1550 nm 40 W unpolarized fiber laser (IPG ELR-50-1550). This laser is first expanded and then focussed to 100 μm diameter by using a 10 cm diameter, 2 m focal length lens. The lens is mounted on an air-bearing magnetically actuated translational stage (Aerotech ABL2000). To transfer the atoms from the MOT to the bus ODT the focus of the bus ODT is overlapped with the MOT. The bus ODT produces a conservative trap with a trap depth of 500 μK. We have observed the lifetime of the atoms in the bus ODT to be dependent on the pressure in the MOT chamber. For a pressure of 4$\times$ 10^{-10} Torr in the MOT chamber the lifetime is about 8 seconds. The large atomic mass of radium and the low longitudinal trap frequency (5.5 Hz) requires alignment of the bus ODT with respect to gravity to better than 10 mrad. The 1550 nm laser is nearly magic for the 714 nm cooling transition meaning the differential light shift of the ground and the excited state are comparable to the

natural linewidth [37]. We can transfer the atoms from the MOT to the bus ODT with a typical efficiency of 80%. The cloud of atoms in the bus ODT is 1 cm long and 100 μm across.

The next step of the experiment involves transporting the atoms from the MOT chamber to the experimental region 1037 mm away, using the bus ODT. To do this we first turn off the 714 nm laser after the cooling phase. The atoms at this stage are trapped in the focus of the bus ODT by the potential of the ODT only. The bus ODT focus is then moved from the center of the MOT chamber to approximately middle of the HV electrodes in the science chamber by translating the bus ODT focussing lens. The radium atoms trapped at the focus of the bus ODT move along with the focus.

The functional form of the lens position vs time was optimized experimentally. The optimum functional form was found to be sinusoidal. Fig. 6.5 shows the data of position as a function of time during the experiment.

In the experimental region the atoms are transferred to a separate standing wave ODT (referred as the "holding" ODT) in the horizontal direction and perpendicular to the bus ODT as shown in Fig. 6.1. The focus of the holding ODT lies between the HV electrodes. The holding ODT is formed by a retroreflected 10 W 1550 nm laser beam focussed to 100 μm diameter (IPG ELR-30-1550-LP-SF). The holding ODT is linearly polarized in the horizontal direction. To improve the transfer efficiency of the atoms from the bus ODT to the holding ODT a temporal 1D MOT formed along the bus ODT axis is used. This 1D MOT is formed by a quadrupole coil and a pair of opposite circularly polarized 714 nm laser beam along the bus ODT axis. The atoms are trapped along the bus ODT axis by the 1D MOT. The atoms are trapped along the transverse direction to the bus ODT axis by the conservative force of the bus ODT. Typically the 1D MOT is turned on for 150 ms after the bus ODT

77
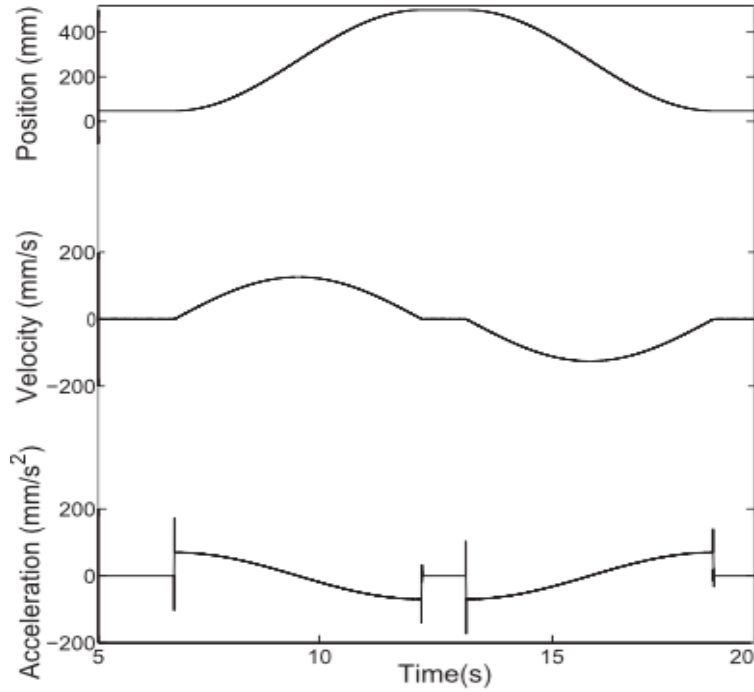
Figure 6.5: Example data from the translational stage, for a transport distance of 460 mm in 5.7 s. The top, middle, and the bottom graphs are position vs time, velocity vs time, and acceleration vs time for a round trip. Position data is obtained from a linear encoder on the stage; differentiation yields the velocity and acceleration profiles.

overlaps with the holding ODT. The 1D MOT changes the aspect ratio of the atom cloud from 100:1 to 1:1. The resultant cloud is 60 μm in diameter and remains in this size after the bus ODT is turned off. After the atoms are loaded into the holding ODT the current to the quadrupole coils are set to zero and a relay opens to circuit to make sure no current flows after the 1D MOT is turned off. The atoms not loaded into the holding ODT are lost. Ideally, for efficient loading the center of the 1D MOT should lie at the overlap region of the bus ODT and the holding ODT. The position of the 1D MOT is coarsely tuned by adjusting the position of the quadrupole

78

coil and the position is fine tuned by adjusting the position of the retroreflected 714 nm laser beams with respect to each other. The overall efficiency of transport of atoms from the 3D MOT to the holding ODT was 5%. The residual magnetization in the experimental region after the quadrupole field was turned off was measured using a fluxgate magnetometer. No residual magnetization was detected and residual magnetic fields were found to be less than the measurement sensitivity of 300 nG.

6.2 Imaging Radium Atoms in the Experimental Region

The radium atoms in the experimental region are imaged using an imaging system shown schematically in Fig. 6.6.
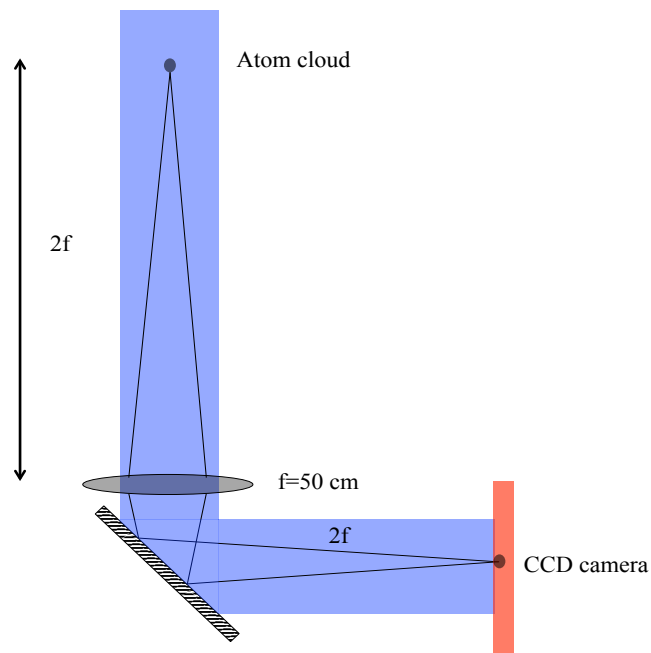
Figure 6.6: A schematic of the imaging system used to image the radium atoms in the experimental region. The purple band represents the 483 nm laser beam used to probe the atoms.

The atoms in the experimental region are probed by a blue laser beam tuned to the resonance of the $7s^2$ $^1S_0 \to$ 7s7p $^1P_1$ transition at 483 nm, co-propagating along the holding ODT. For ^{225}Ra we excite along the $7s^2$ $^1S_0$ F=1/2 $\to$ 7s7p $^1P_1$ F=3/2 transition. This transition can cycle for an average of about 1000 times before leaking to lower D states. The shadow produced by the resonant absorption is imaged onto a CCD camera (Andor, Clara) [8] with unity magnification by using a 50 cm focal length lens. The camera [8] has a quoted quantum efficiency (QE) of $\approx 60\%$ at 483 nm and a measured gain of 1.7. The resolution of our imaging system is 5.8 μm (Rayleigh criterion) with pixel area of (6.45 μm $\times$ 6.45 μm) in the image plane. To produce an absorption image the blue beam is pulsed for 1.45 ms during which each ^{225}Ra atom absorbs on average 100 photons. The camera is exposed for 3 ms (minimum exposure time allowed for our typical camera setting). The typical atom number (about 200 ^{225}Ra atom) results in a weak raw absorption image signal dominated by noise. To suppress the effects of noise a background subtraction scheme is used.

6.2.1 Background Subtraction

The noise in the raw absorption image signal originates from fringes due to diffraction and interference of the probe beam by optical elements. The fringe pattern fluctuates shot to shot due to vibration of these elements. Therefore a simple background subtraction scheme involving subtraction of a single reference signal without atoms from an image with atoms does not work very well for noise reduction. To reduce the noise due to fluctuating fringe pattern, a fringe removal algorithm described in ref. [76] is used.

The algorithm involves composing a matching optimal reference image Q, con-

structed as a linear combination of many reference images R_k within a set, $Q = \sum_k c_k R_k$. This is done for each absorption image A. The coefficients c_k are obtained by minimizing the least square difference between the absorption and reference images $\sum_x m_x (A_x - Q_x)^2$, where x indicates each pixel, within a specified background region ($m_x = 1$) excluding the signal region ($m_x = 0$). Setting partial derivatives with respect to c_j to zero, we obtain a linear system of equations, $\sum_k c_k B_{j,k} = \sum_x m_x R_{x,j} A_x$, with the square matrix $B_{j,k} = \sum_x m_x R_{x,j} R_{x,k}$, which is solved for c_k. A typical data obtained during the EDM experiment contains 500-1000 absorption images. $B_{j,k}$ is decomposed once using LU or singular value decomposition and then substituted to obtain c_k for each absorption image.

Following this algorithm a software program in LabVIEW was written for live processing of absorption signal data obtained from the CCD camera during the tuning phase of the experiment. A separate MATLAB [71] program that implements the same fringe removal algorithm is used for offline processing of absorption signal data.

To estimate the noise in the imaging of the atoms using the background subtraction scheme a region of interest (ROI) is defined in a background subtracted image. Then, the ADC counts of each pixel in that ROI is added to obtain a total number of counts for that Image. This is done for a set of background subtracted images using a same size ROI. The standard deviation of the total number of counts in the ROIs in the image set is an estimate of the noise in our imaging scheme. The photon shot noise limit is estimated by taking the square root of the mean of the total counts in the ROIs of the same image set but without background subtraction. It is found that the noise in the background subtracted image reaches about 1.2 times the photon shot noise limit.

An example of a typical result, obtained after application of the background subtraction algorithm is represented in figures (Fig. 6.7 and Fig. 6.8). The side by

side figures show the images of a cloud of ^{225}Ra atoms before and after the background subtraction. For this particular raw image, 240 reference images are used to create the background for the background subtraction.
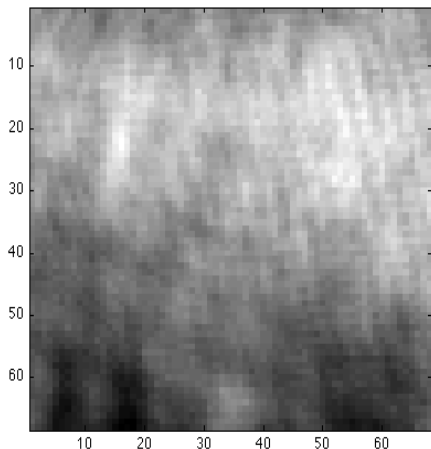
Figure 6.7: A raw shadow image of ^{225}Ra atoms loaded into the holding beam before background subtraction. The horizontal and vertical scales show the pixel numbers in the CCD camera. The size of the image is 68 pixels × 68 pixels.
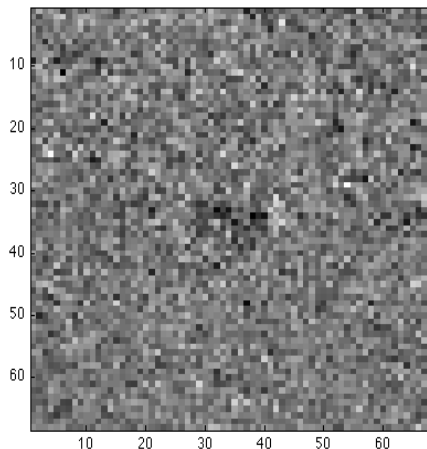
Figure 6.8: The result after background subtraction of the image shown in Fig. 6.7. The dark spot in the middle of the image is the shadow of a cloud of about 300 ^{225}Ra atoms. The area of a single pixel is 6.45 μm × 6.45 μm.

Using this background subtraction scheme we image the radium atoms in the experimental region. Because of the low number of available ^{225}Ra atoms we use ^{226}Ra atoms to tune the efficiencies of transporting the atoms from the oven to the holding ODT in the experimental region. In the MOT region we use a simple background subtraction scheme involving subtraction of an image without atoms from an image with atoms in it. This simple scheme works in the MOT region because of relatively large atom numbers in the MOT compared to that in the experimental region.

Fig. 6.9 shows a typical image of ^{226}Ra atoms in the bus ODT in the experimental

region. These kinds of images are used to tune the transfer of atoms from the bus ODT to the holding ODT. The first step in the tuning process involves improving the compression of atoms due to the 1D MOT. This is done by adjusting the parameters of the 1D MOT such as the power and the frequency of the 714 nm 1D MOT beam, the alignment of these beams with respect to each other and to the bus beam. To improve the transfer of the atoms from the bus beam to the holding beam the first step is to overlap the 1D MOT with the holding beam. We usually overlap the first pass of the holding beam with the middle of the 1D MOT and then using the retroreflector mirror for the holding beam we align the second pass of the holding beam to the 1D MOT. After this initial alignment, the fine tuning is done by making sure the first pass and the second pass of the holding beam overlaps with each other. The quality of the holding beam is continuously monitored using an interferometer formed by the first pass and the second pass of the holding beam.
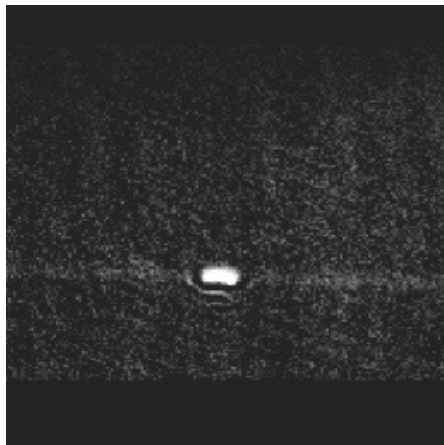
Figure 6.9: Image of ^{226}Ra atoms in the overlap of the bus ODT and the holding ODT in the experimental region. Atoms that are not in the overlap region are also seen. The image is inverted to make bright appearance for the shadow. The dark bands at the top and bottom show the copper electrodes.

6.3 Obtaining the Absorption Signal

To measure the absorption of the 483 nm blue probe light by the atoms we first take a raw absorption image of the atoms. We then subtract a reference background image from the raw absorption image. The reference background image is generated using the subtraction algorithm. In the background subtracted image, we define an ROI covering the shadow of the atoms. The absorption signal is the integrated ADC counts in the ROI. This idea is illustrated in Fig. 6.10 using a background subtracted shadow image of ^{226}Ra atoms loaded into the holding ODT.
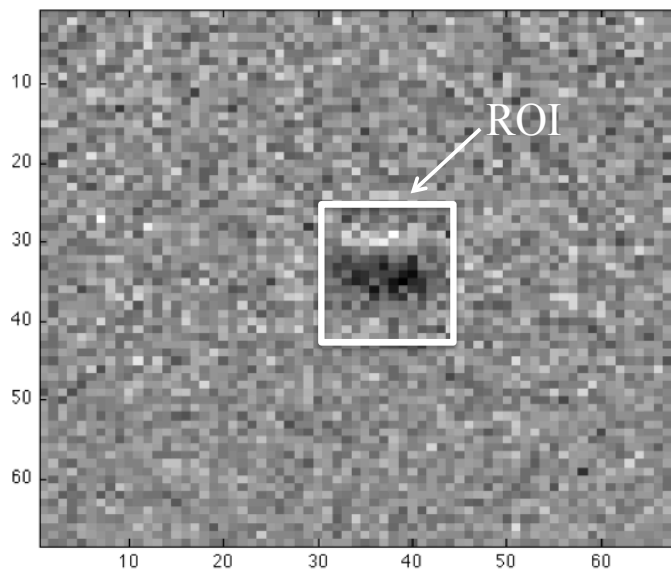
Figure 6.10: Example of a background subtracted shadow image of ^{226}Ra atoms loaded into the holding ODT showing the ROI.

The white rectangle in the image in Fig. 6.10 is the ROI. The integrated ADC counts in the ROI is a measure of the absorption of the blue light and this is the absorption signal that is used for the EDM measurement. During the EDM measurement we crop the CCD image into a 68 pixels $\times$ 68 pixels area in order to improve

the data transfer speed between the camera and the computer.

By measuring the absorption signal of the blue probe light as a function of time we can also measure the lifetime of the atoms in the holding beam. The following figure (Fig. 6.11) shows a plot of the absorption signal of the blue probe light from ^{226}Ra atoms loaded into the holding beam as a function of time. The error bars are statistical only. During the EDM experimental runs the lifetime of the radium atoms in the holding beam was found to be 4 ± 1 s.
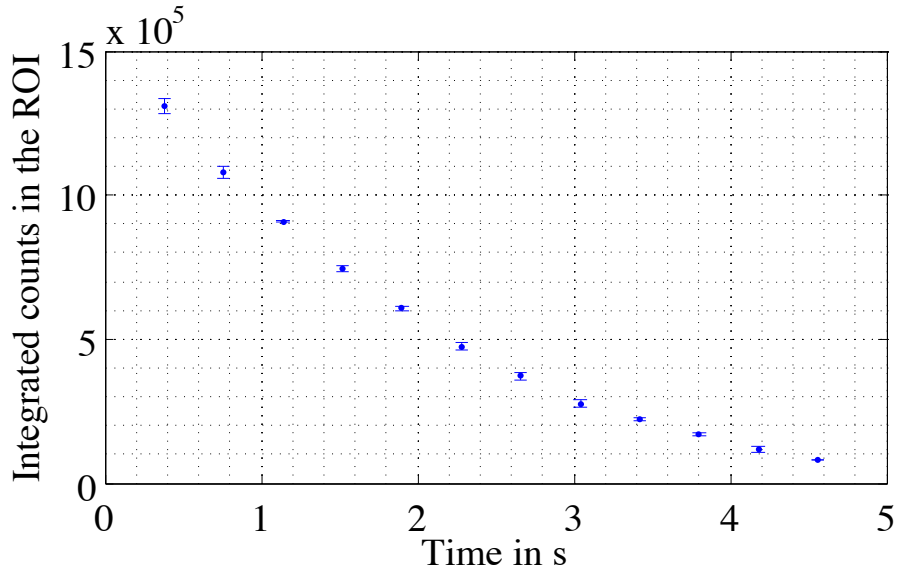
Figure 6.11: Absorption of the blue probe light from ^{226}Ra atoms loaded into the holding beam as a function of time.

Chapter 7 The EDM Experiment

We performed a series of EDM experiments in October and December of 2014. As I have discussed so far, we developed an experimental setup for these measurements. In this setup, neutral ^{225}Ra atoms are collected in a MOT. The collected atoms are transported 1 meter using an ODT, and then the atoms are transferred to a second standing wave ODT in between a pair of copper electrodes in our experimental chamber. An uniform magnetic field is also applied to the atoms. The experimental chamber is magnetically shielded. The atoms are then optically polarized and allowed to Larmor precess in parallel and antiparallel electric and magnetic fields. The difference between the Larmor precession frequency for parallel and antiparallel fields is experimentally determined to measure the EDM. In this chapter I explain the details of the EDM experiments that we performed and discuss the results obtained from these experiments. The results of these two experimental runs have been recently published in ref. [78].

7.1 Collection of the EDM Data

To collect the EDM data we ran the experiment in cycles. A single EDM experimental cycle lasted for 50 s. During the first 40 s of the cycle the atoms are loaded into the MOT. In the next 10 s the atoms are transported from the MOT to the experimental region (typically in 6.5 s), then they are loaded into the holding ODT, and finally the spin precession measurement of the atoms trapped in the holding ODT was performed. During each experimental cycle reference images without any trapped atoms are taken to use in the background subtraction algorithm. In each

86

experimental cycle, a total of 25 reference images are taken; 5 images before precession measurement and 20 images after the precession measurement. This EDM experimental cycle is repeated to build up statistics of the experiment.

The spin precession measurement period consisted of several events as shown in the form of a chart in Fig. 7.1. We collect spin precession data for both "E field on" and "E field off" configurations during this measurement period.

Time

½ precession period

2 s
"E field on"

2 s
"E field off"

Image #1 — Detect spin after loading atoms into ODT using 60 μs long 483 nm pulse.

Pol. #1 — Polarize atoms using 1.45 ms long 483 nm pulse.

Image #2 — Detect spin after half precession period using 60 μs long 483 nm pulse.

Pol. #2 — Polarize atoms using 1.45 ms long 483 nm pulse.

Image #3 — Detect spin to collect "E-field" on data using 60 μs long 483 nm pulse.

Pol. #3 — Polarize atoms using 1.45 ms long 483 nm pulse.

Image #4 — Detect spin to collect "E-field off" data using 60 μs long 483 nm pulse.

Figure 7.1: Sequence of the events during the EDM measurement period in an experimental cycle. Time in this chart increases from top to bottom. After each polarizing event the time is reset to zero.

During the spin precession measurement period we used two kinds of 483 nm blue

87

laser pulses generated by an aquosto optic modulator (AOM) switch: 1.45 ms long pulses to polarize the atom cloud and 60 μs long pulses to measure the number of atoms in the opposite spin state (in order to detect the spin). The durations of these pulses were determined experimentally. The durations of the short pulses were optimized to improve the signal-to-noise ratio of the absorption image and the duration of the long pulses were optimized to maximize the polarization of the atoms in the atom cloud. After each pulse, the laser was blocked by using a mechanical shutter within 1 ms to prevent decoherence of the precessing atoms by light leaking through the AOM switch. Three polarizing pulses were used and five images were recorded in each measurement period. The first image was taken without any polarization pulse. The second image was taken after about one half period of the spin precession period following a polarization pulse. The third image was taken 2 s after the second polarization pulse. During this time the E field was applied. After the third image the atoms were again polarized using the third polarization pulse. 2 s after the third polarization pulse the fourth image was taken, this time without applying any E field in between. A fifth image was used as a diagnostic and not used in the final analysis of the EDM experimental data. The direction of the E field was reversed at alternate experimental cycles. The B field in the experimental region was kept on for the complete duration of the EDM experiment.

Usually a single run of the experiment involves $60-70$ EDM experimental cycles. After each run the efficiency of the setup was checked and tuned (if needed) by switching the lasers to trap ^{226}Ra. Fig. 7.2 shows a typical plot obtained after an EDM experimental run consisting of 64 experimental cycles. The plot shows the average number of integrated counts in an ROI of 2 pixels $\times$ 2 pixels area inside the shadow of the atoms in the background subtracted images, as a function of image number. The error bars were determined according to $\sigma/\sqrt{n}$, where σ is the standard

88

deviation of the integrated counts in the ROI and n is the number of measurements. This integrated number of counts in the ROI is the absorption signal. In this example image number three is taken at 2003 ms after the polarizing pulse number two and image number four is taken 1989 ms after polarizing pulse number three.
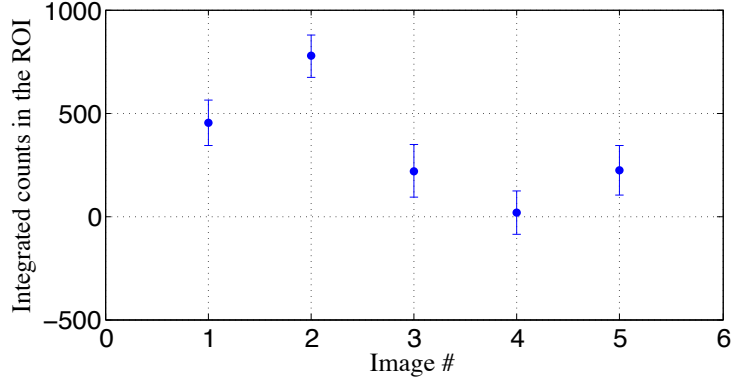
Figure 7.2: Plot showing results of an experimental run consisting of 64 experimental cycles of a single sequence. The "E field on" data was obtained from the third image and the "E field off" data was obtained from the fourth image. See also Fig. 7.1.

Plots similar to that shown in Fig. 7.2 were generated by changing the delay time of the third image after the second polarizing pulse for each polarity of the HV, and by changing the delay time of the fourth image after the third polarizing pulse. The absorption signals in the third and the fourth image are normalized to the absorption signal in the second image in order to reduce the sensitivity to atom number fluctuations. The weighted average of the absorption signal in the third image as a function of delay time after the preceeding polarization pulse is used to generate the precession curve for the "E field on" data for each polarity of the HV (Anti-parallel data and parallel data w.r.t. the B field). Similarly, the weighted average of the absorption signal in the fourth image is used to generate the precession curve for the "E field off" data. The statistical error (according to

89

$\sigma/\sqrt{n}$) obtained after each run is used as the weight. The precession data obtained using this procedure in October 2014, and collected using a 3 mCi sample of ^{225}Ra are shown in Fig. 7.3.
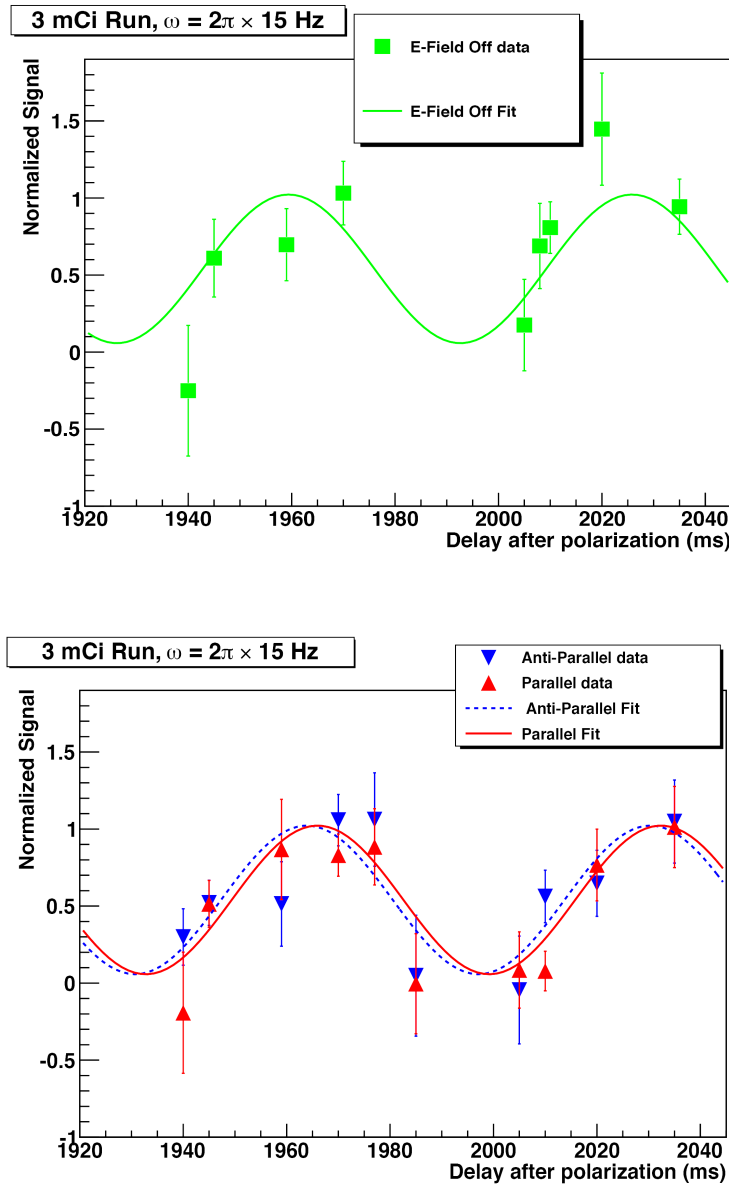
Figure 7.3: Precession curves from experimental run in October 2014.

Fig. 7.4 show the precession data obtained in December 2014 using a 6 mCi sample of ^{225}Ra.
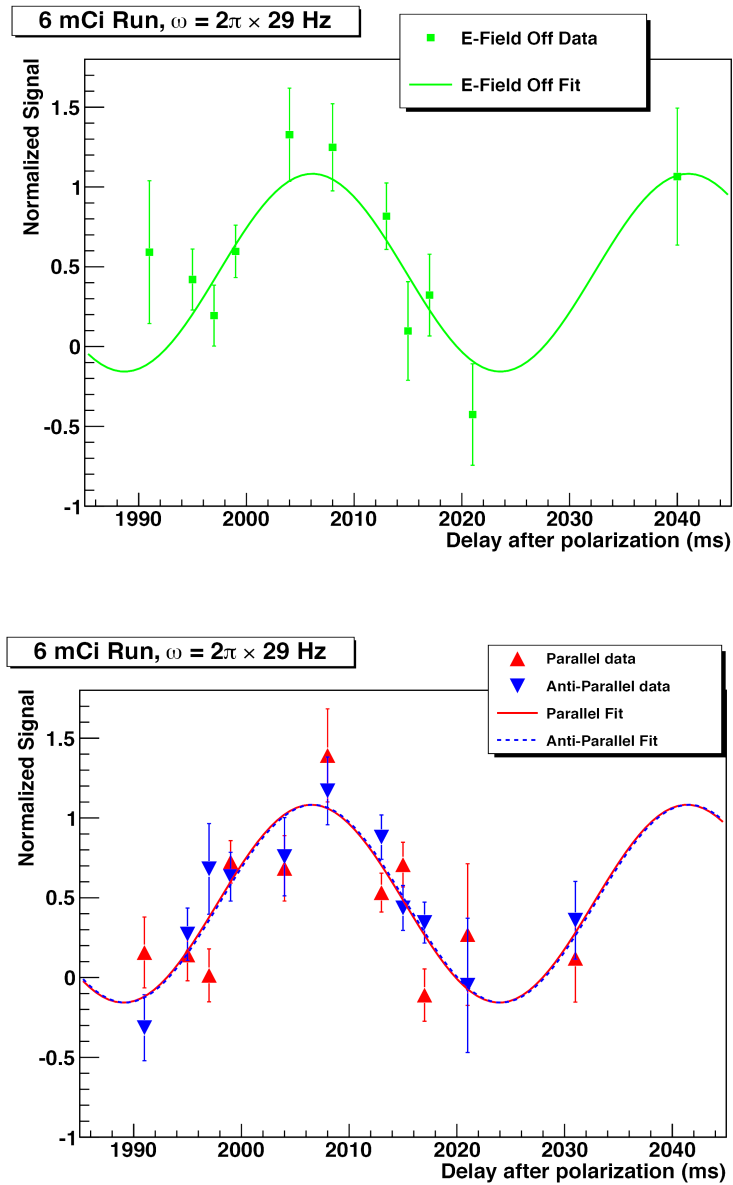
Figure 7.4: Precession curves from experimental run in December 2014.

7.2   Analysis of the EDM Data

Fig. 7.3 and Fig. 7.4 show the spin precession data with "E field on" and pointing parallel to the B field or anti-parallel to the B field, or with "E field off". Each data point was corrected for trap losses using the measured trap lifetime. Data taken under the three E field configurations were fitted (the solid lines in Fig. 7.3 and Fig. 7.4) simultaneously to a combined set of equations:

$$y_0(t) = \frac{\text{A}}{1+\text{P}}[1 - \text{P}\cos(\omega t)] \tag{7.1}$$

$$y_{\uparrow\uparrow/\uparrow\downarrow}(t) = \frac{\text{A}}{1+\text{P}}[1 - \text{P}\cos(\omega t + \theta \pm \Delta\phi/2)], \tag{7.2}$$

where $y_0(t)$ represents the configuration "E field off", $y_{\uparrow\uparrow}(t)$ represents the configuration "E field parallel to the B field", and $y_{\uparrow\downarrow}(t)$ represents the configuration "E field anti-parallel to the B field". Five parameters A (normalization), P (atom polarization), ω (precession frequency with "E field off"), θ (overall phase offset caused by effects common to both E field polarities) and $\Delta\phi$ (polarity dependent phase shift induced by an EDM) were fitted without constraints. A computer program written in ROOT [9] was used for the fitting. The program uses the Minuit function minimization tool [10] to minimize the combined χ^2 of the three sets of data ("E field off", "E field parallel to the B field" and "anti-parallel to the B field") to obtain the best values of the five fit parameters. The following table (Table 7.1) shows the results of the fits to the data obtained in the 3 mCi and the 6 mCi runs.

The EDM of ^{225}Ra is calculated using the values of the fit parameters shown in table 7.1. The EDM is given by $d = \hbar\Delta\phi/4E\tau$, where τ=1.2 s is the spin precession time, E=67 kV/cm is the applied E field, and $\hbar$ is the Planck constant. The EDM of ^{225}Ra was found to be consistent with zero for both runs: $-(4.0 \pm 5.2) \times 10^{-22}$

$e \cdot$cm in the 3 mCi run and $(0.6 \pm 2.9) \times 10^{-22}$ $e \cdot$cm in the 6 mCi run, where the uncertainties are statistical only.

	A	P	ω (radian)	θ (radian)	$\Delta\phi$ (radian)	Reduced χ^2
3 mCi run	1.022 ± 0.074	0.945 ± 0.120	$2\pi\times(15.056$ ± 0.000)	-0.524 ± 0.234	−0.195 ± 0.253	$\chi^2/24$ = 1.11
6 mCi run	1.083 ± 0.075	1.157 ± 0.078	$2\pi\times(28.662$ ± 0.000)	−0.081 ± 0.155	0.031 ± 0.140	$\chi^2/28$ = 1.35

Table 7.1: Values of the five parameters obtained after the fits to the EDM data obtained in October and December of 2014.

7.3 Analysis of the Systematic Effects

Several possible systematic effects were considered to put limits on false EDM signals. Effects due to correlations between the high voltage and the current supply for the bias B field, the blue probe frequency, external B fields, and the standing wave ODT power were considered. Some of these studies were performed by Matt Dietrich and this section is written with help from him.

A shift in the output current of the power supply for the bias B field correlated with the high voltage can mimic an EDM like signal. The output current was measured by a digital multimeter. The false EDM can be written as $d_F = \frac{\mu B_0}{E_0} \frac{\Delta I}{I}$. The E field was ramped to 70 kV/cm in both polarities and the slope of the current output with applied E field is measured. The slope is consistent with zero and the upper limit on the slope is measured as 2×10^{-6} A/(kV cm^{-1}) leading to a possible false EDM of 0.6×10^{-24} $e \cdot$cm.

A change in the blue laser frequency correlated with the HV can change the scattering rate of the laser light by the radium atoms resembling an EDM like signal.

The transmission of the blue laser through the Zerodur cavity on resonance was measured for both polarity of the E field at 70 kV/cm using a battery powered photodiode. The fractional shift in the transmission was measured to be 235×10^{-6} /(kV cm^{-1}). This measurement was converted into a limit on the laser frequency shift. From the transmission measurement the change of the blue laser frequency correlated with applied E field was obtained. Any correlation was found to be less than the measurement sensitivity. The upper limit on the false EDM due to this effect was found to be 7.4×10^{-24} $e \cdot$cm. However, when we detect the spin the E field is mostly off (the time between E field ramp off signal and the absorption image is 390 ms). Therefore this effect is further suppressed. Assuming a suppression of 100 the upper limit on the false EDM is at the level of $\sim 10^{-25}$ $e \cdot$cm.

Changes in the holding beam power correlated with the E field can lead to an EDM like effect if the holding beam has some residual ellipticity. The changes in the energy levels of the atom due to the interaction of the holding beam light can be separated into vector and tensor shifts [54]. The vector shift can be expressed in terms of an effective magnetic field directed along the k vector of the holding beam laser [89]. The vector shift for a 10 W circularly polarized standing wave is expected to be 100 Hz. The false EDM can be written as

$$d_F = \eta \frac{\Delta \nu}{2\pi} \frac{\Delta P}{P_0} \frac{\hbar}{2E}, \tag{7.3}$$

where η represents a suppression factor. The vector shift is zero for linearly polarized light. If the k vector of the laser light is perpendicular to the B field the vector shift is zero to the first order. The change in holding beam power is measured with a photodiode correlated with each polarity of the E field at 70 kV/cm and the upper limit of the false EDM is estimated to be at 4×10^{-26} $e \cdot$cm assuming a suppression of 10^{-4}.

The correlation of the external magnetic field with the E field is measured using a fluxgate magnetometer while ramping the E field to 70 kV/cm at each polarity. The magnetometer is placed outside the μ-metal shields. The false EDM is calculated using

$$d_F = \eta \frac{\mu \Delta B}{E} \tag{7.4}$$

η is the suppression factor and is set equal to the measured shielding of 20,000 of the μ-metal shields. The external magnetic field was measured to be 250 mG and the upper limit of the correlation was found to be at 96 ppm level. The upper limit on the false EDM is found to be $0.7 \times 10^{-24} e \cdot$cm.

The false EDM signal that can appear due to leakage current, induced B fields due to E field pulsing, $\mathbf{E} \times \mathbf{v}$ effects, and the geometric phase were modeled.

The leakage current between the electrodes changes sign with the polarity of the E field . Hence the B field created by the leakage current will change sign correlated with the E field and it can mimic an EDM like signal. To put a limit on the systematic effect due to leakage current, a model is used where the current flows as a narrow beam between the gap, and it passes through the outer edge of the radium cloud. If the direction of current is perpendicular to the electrodes it will not cause any systematic effect. Also if the current passes through the center of the cloud the average field is zero and hence the systematic effect will be zero. The leakage current will produce a systematic effect if the current flows at an angle w.r.t the normal to the electrode surface. To put a conservative limit on this systematic effect, we assume that the electrons forming the leakage current leave at zero initial velocity parallel to the electric field lines with the speed of light. Then the time to travel to the other electrode can be written as

$$\frac{1}{2} \frac{eV_0}{lm_e} t^2 = l \tag{7.5}$$

95

The maximum angle (w.r.t. the normal to the electrode surface) of the current flow is given by

$$\tan\theta = \frac{ct}{l} = \sqrt{2m_e c^2/eV_0} \tag{7.6}$$

If the radius of the radium cloud is given by r, then the frequency shift is given by,

$$\frac{2d_F E}{\hbar} = \frac{2\mu}{\hbar}\frac{\mu_0 I}{2\pi r}\sin\theta$$
$$d_F = \frac{\mu}{E}\frac{\mu_0 I}{2\pi r}\sin\theta. \tag{7.7}$$

Using V_0=16 kV, E=80 kV/cm, r=50 μm, and I=79 pA the upper limit on the false EDM is d_F=9×10^{-26} e·cm.

In the holding ODT the atoms are in motion. When we apply the E field, then according to special relativity a magnetic field B_m is generated in the frame moving with the atoms. To the first order this "motional B field" is given by,

$$\mathbf{B}_m = \frac{\mathbf{v}}{c^2} \times \mathbf{E}. \tag{7.8}$$

Where $\mathbf{v}$ is the velocity of the atoms and c is the speed of light. The direction of the "motional B field" changes with the direction of the E field. This can mimic an EDM like signal. This will cause a problem if the E and B fields are not parallel to each other. However, for a perfect harmonic trap this kind of effect will average out to zero and does not produce any systematics. The motional field is about 440 nG for an atom moving with 40 cm/s (at 50 μK).

The above analysis indicate that the combined effects due to these possible systematics is smaller than 1×10^{-25} e·cm. All these considered effects are linear in the E field.

We have also considered EDM like effects that can arise due to quadratic dependence on the E field. The effects quadratic in E field do not produce EDM like signal,

unless the E field reversal is imperfect. We have used our spin precession data to put a limit on these effects. The E field imbalance was found to be 0.7%. Using our data for "E field parallel", "E field antiparallel", and "E field off", we have measured the linear and quadratic dependence of the phase on the E field. For this measurement the values of $\Delta\phi$ from table 7.1 were fitted to a function that contained two terms: a term linear in the E field, and a term quadratic in the E field. From this fit we obtain the value of the quadratic term and by using this value we placed a limit on the potential E^2 effects. The quadratic effect was found to be below $2\times10^{-23}e\cdot$cm for the 3mCi run and below $5\times10^{-24}e\cdot$cm for the 6mCi run. The quadratic effects currently generate the leading order systematics in our experiment. This is mainly due to statistical limitation of our spin precession data. With increase in the statistical sensitivity of the spin precession data, the limits placed on the E^2 effects will also improve.

7.4   Current Limit on the EDM of ^{225}Ra and Future Improvements

We carried out two experimental runs to search for the EDM of ^{225}Ra. In both of the experimental runs the EDM of ^{225}Ra was found to be consistent with zero: $-(4.0 \pm 5.2) \times 10^{-22}$ $e\cdot$cm in the 3 mCi run and $(0.6 \pm 2.9) \times 10^{-22}$ $e\cdot$cm in the 6 mCi run, where the uncertainties are statistical only. We have considered several possible systematic effects. For now all the systematic effects are found to be below our statistical sensitivity. From these two experimental runs we have measured the EDM $d(^{225}$Ra$) = -(0.5 \pm 2.5_{\text{stat.}} \pm 0.2_{\text{syst.}})\times10^{-22}$ $e\cdot$cm and set an upper limit at $d(^{225}$Ra$)$ $<5.0\times10^{-22}$ $e\cdot$cm (95% confidence level). Analysis shown in ref. [26] indicates that an EDM measurement of ^{225}Ra at the sensitivity level of 10^{-25} $e\cdot$cm will start to constrain several parameters of the pion nucleon interaction. The implications of the

97

current results our measurement have been discussed in ref. [97].

Our experimental results represent the first ever measurement of the EDM of the ^{225}Ra atom. These current EDM results are limited by the statistical sensitivity of our experiment. Based on our experience with these EDM measurements we have identified several aspects of our experimental system that can be improved in order to increase the statistical sensitivity. In the next paragraphs of this section I discuss about some of these improvements that can be made in our experimental system for the next generation of EDM experiments of the ^{225}Ra atom.

The maximum value of the E field in our EDM experiments was limited to 67 kV/cm due to HV sparking beyond 67 kV/cm. E field up to 87 kV/cm without sparking had been demonstrated in the current set of electrodes in a test chamber. The electrodes were exposed to air during the installation in the EDM setup. Further HV conditioning of the electrodes in the EDM setup have the potential to improve the performance of the electrodes to hold higher voltage without sparking. The EDM sensitivity increases directly with increase in the E field (Eq.1.12).

In both of the EDM experimental runs the E field was on for 1.2 s. The duration of the E field was limited by the short lifetime of the atoms in the standing wave ODT. This is mainly due to limitation of the vacuum in the glass tube (typically 2×10^{-10} Torr to 3×10^{-10} Torr). We have identified a leak in the vacuum system near the feedthroughs for the HV. Recently this leak has been fixed and we expect an order of magnitude improvement in the vacuum and as a result we expect to increase the lifetime of the atoms in the holding ODT to 15-20 s. The EDM sensitivity improves as the square root of the precession time of the atoms in the E field (Eq.1.12).

The efficiency of detecting the spin state was limited by low number of scattered photons per atom (during the detection pulse the atoms get optically pumped to the dark state after scattering 2-3 photons). The number of scattered photons can

be increased by using an atom shelving technique before spin detection. Stimulated Raman Adiabatic Passage (STIRAP) technique [20] can be used to transfer population from one of the spin states to the long lived $^3D_1$ state. This scheme will need application of two more laser pulses before a detection pulse. The idea is illustrated in Fig. 7.5. One way of using this technique can be the transfer of population of the atoms in the $7s^2$ $^1S_0$ F=1/2, $m_F=-1/2$ state to the $7s6d^3D_1$ state without disturbing the atoms in the $m_F=1/2$ state by the use two STIRAP pulses at 483 nm and 1429 nm. After the population transfer the spin detection step converts into an atom number detection step. During the number detection step the atoms can be made to scatter 1000 photons instead of 3 using a detection pulse along the $7s^2$ $^1S_0$ F=1/2 $\rightarrow$ $7s7p$ $^1P_1$ F=3/2. Successful implementation of the STIRAP scheme has the potential to improve the EDM sensitivity up to a factor of 20.
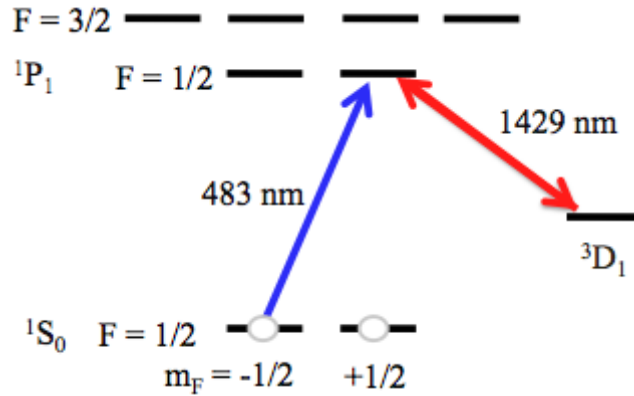
Figure 7.5: A scheme for using STIRAP in the ^{225}Ra atom. By varying the duration and timing of the 483 nm and the 1429 nm laser pulses the population in the m_F=-1/2 state can be transferred to the $^3D_1$ state. The 1429 nm laser pulse will preceed the 483 nm laser pulse.

The number of atoms in the MOT and subsequently in the holding ODT can be increased by using the $7s^2$ $1S_0$F=1/2$\rightarrow$ $7s7p$ $1P_1$ $F = 3/2$ blue transition for

transverse cooling and slowing. Our current 1 m long Zeeman slower based on the 714 nm red transition is designed to capture atoms moving at 60 m/s. A slower based on the blue transition can be designed to capture atoms moving at 300 m/s. The Maxwell distribution of the atoms peaks at a velocity of about 300 m/s for our typical oven temperature of (450-550)°C. This slower can be added to the system before the current red slower. The blue transition is a factor of 100 stronger than the red transition. This scheme however will require two more repump lasers.

Along with increasing the efficiency of the trapping scheme, the EDM experiment will benefit from more and frequent supply of ^{225}Ra. A single ^{225}Ra source was available for us every two months. Usually a single source was gradually spent over a period of about 10 days in the experimental runs. Starting this year (2015) it will be possible to obtain one source of ^{225}Ra every month. Stronger sources of ^{225}Ra are under development at various nuclear physics facilities, including the Facility for Rare Isotope Beams [17]. Estimates for the spallation of a thorium target induced by a 1 mA beam of deuterons at 1 GeV indicates yield of ^{225}Ra at the rate of 10^{13} s^{-1}, which is 5 orders of magnitude stronger than the currently available supply.

7.5 Summary and Conclusions

We have developed an experimental system to search for the EDM of the ^{225}Ra atom. The experimental system uses the techniques of laser cooling and trapping. Using this experimental system we have performed the first ever measurement of the EDM of the ^{225}Ra atom and set an upper limit at $d(^{225}$Ra$) <5.0{\times}10^{-22}$ $e{\cdot}$cm (95% confidence level). This is the first measurement of an EDM in an octupole deformed nucleus. Based on the experience of our recent EDM measurements we have identified several possible improvements to the current system. Some of these

improvements are currently being implemented. According to eq. 1.12 if we use E field E=100 kV cm^{-1}, number of atoms N=1$\times$10^6 atoms, spin precession time of τ=100 s and detection efficiency of ϵ=1 then according to Eq. 1.12 EDM sensitivity of 3$\times$10^{-28} e·cm can be reached in $T = 100$ days.

Chapter A Optical Arrangements

A.1 Double pass AOM

The optical arrangement for using an AOM in the double pass configuration. This kind of arrangements were used in the paths of several of the laser beams used in the experiment. e.g. in the path of laser beams going to the MOT, the 1D MOT, the ULE cavity etc.
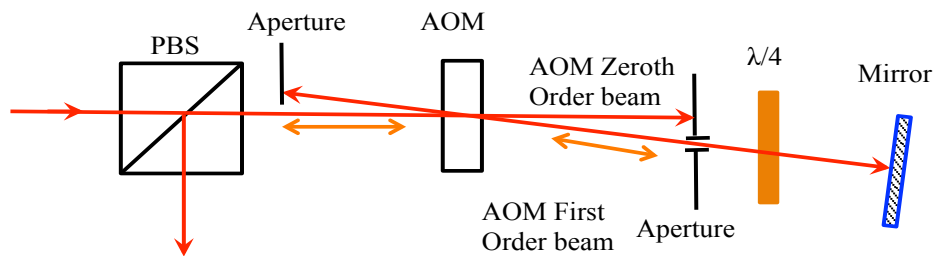
Figure A.1: AOM in double pass configuration.

Chapter B Laser Stabilization Scheme

B.1   Fabry Perot Cavity and the PDH Method

A Fabry-Perot cavity is a pair of highly reflective mirrors mounted on a stable spacer. Incident light can pass through the cavity if twice the length of the cavity is equal to an integer multiple of wavelength of light. In the case of a free space cavity, the free spectral range(FSR), which is the spacing between resonant frequencies is given by

$$\Delta\nu_{FSR} = \frac{C}{2L} \tag{B.1}$$

where C is the velocity of light and L is the distance between the mirrors.
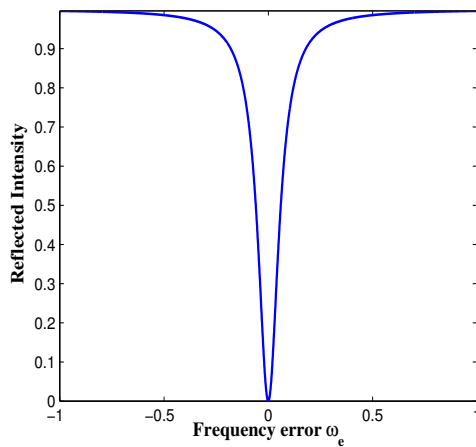
Figure B.1: Magnitude of reflection coefficient
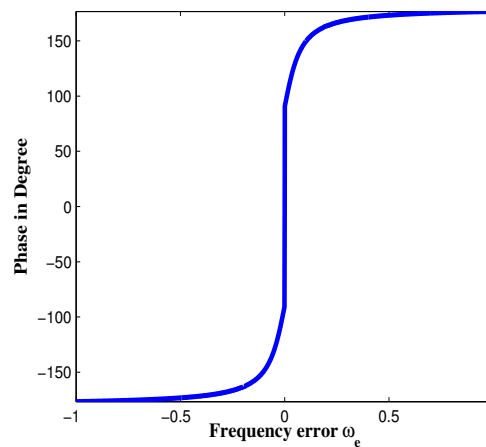
Figure B.2: Phase of reflection coefficient

The reflection coefficient $F(\omega)$ is the ratio of reflected light and incident light and it can be written as a function of incident light frequency ω and the cavity resonance

103

frequency ω_0 as follows

$$F(\omega_e) = \frac{E_{ref}}{E_{inc}} = \frac{r\left(exp(i\frac{\omega_e}{\Delta\nu_{FSR}}) - 1\right)}{1 - r^2 exp(i\frac{\omega_e}{\Delta\nu_{FSR}})} \tag{B.2}$$

where r is the amplitude reflection coefficient of each mirror and $\omega_e = \omega - \omega_0$.

The above figures show plots of the intensity and phase of the reflection coefficient around resonance. The phase of the reflected beam is antisymmetric above and below resonance. The PDH method provides a way of indirectly measuring the phase and thereby tells which side of cavity resonance the frequency of the laser is.

In the PDH method the frequency of the incident laser beam is modulated. The modulation generates sidebands with definite phase relationship to the incident and the reflected beams. These sidebands are interfered with the reflected beam, the sum displays a beat pattern at the modulation frequency and the phase can be measured.

Frequency modulation of the incident laser beam is achieved by modulating the phase using an Electro-Optic-Modulator(EOM). After the beam passes through the EOM its electric field is phase modulated and can be written as

$$E_{inc} = E_0 e^{i(\omega t + \beta \sin \Omega t)}. \tag{B.3}$$

This can be expanded using Bessel functions, to

$$E_{inc} \approx [J_0(\beta) + 2iJ_1(\beta) \sin \Omega t]e^{i\omega t} \quad = E_0[J_0(\beta)e^{i\omega t} + J_1(\beta)e^{i(\omega+\Omega)t} - J_1(\beta)e^{i(\omega-\Omega)t}]$$

From the above equation it can be seen that beams with three different frequencies are incident on the cavity, a carrier with frequency ω and two side bands with frequencies $\omega \pm \Omega$. Ω is the phase modulation frequency (11.6 MHz in our case) and β is the modulation depth.

With one carrier at ω and two sidebands at $\omega \pm \Omega$ the total reflected beam can be written as

$$E_{ref} = E_0[F(\omega)J_0(\beta)e^{i\omega t} + F(\omega + \Omega)J_1(\beta)e^{i(\omega+\Omega)t} - F(\omega - \Omega)J_1(\beta)e^{i(\omega-\Omega)t}]. \tag{B.4}$$

104

The reflected power detected by a photodetector is $P_{ref}{=}|E_{ref}|^2$

$$P_{ref} = P_c|F(\omega)|^2 + P_s\left(|F(\omega + \Omega)|^2 + |F(\omega - \Omega)|^2\right) + 2\sqrt{P_cP_s}\Big(Re[F(\omega)F^*((\omega + \Omega)$$
$$-F^*(\omega)F(\omega - \Omega)]\cos\Omega t + Im(F(\omega)F^*(\omega + \Omega) - F^*(\omega)F(\omega - \Omega\sin\Omega t\Big) + \mathcal{O}(2\Omega) \text{(B.5)}$$

P_c and P_s are the power in the carrier and sidebands respectively. The Ω terms arise from the interference between the carrier and the sidebands and the 2Ω terms come from the sidebands interfering with each other. The interesting terms are the terms that are oscillating at the modulation frequency Ω because they sample the phase of the reflected carrier. A photodetector detects all the terms in Eq.B.5. The term of interest at Ω is isolated using a mixer and a low pass filter and this signal is the error signal. This error signal is the input to a servo which tries to keep this signal at zero.

B.2   ULE Cavity

We bought the ULE cavity from ATFilms. The specifications of the cavity can be found in the following catalogue from AT Films,

SECTION A-A

SECTION B-B

2X Mirrors
⌀25.4mm

⌀D1

L

L/2

1mm X 45° CHMFR

6 mm TYP

R1

R2

⌀D2 (vent)

⌀D3

Notes:

- Mirrors to be optically contacted

- R1, R2 are mirror curvatures (PL/CC)
- See Table 1 for Dash No's and Dimensions

Table #1 - Dash No.'s: Cylinder Cavity Assembly Specifications
(Table dimensions are in mm unless otherwise specified)

DASH NO	SPACER MAT'L	D1	D2	D3	L	R1	R2
-1	Premium Grade ULE	100.00	5.0	10.0	100	Plano	50cm
-2	Premium Grade ULE	70.00	6.0	12.7	100	Plano	50cm
-3	Premium Grade ULE	60.00	6.0	12.7	100	Plano	50cm
-4	Premium Grade ULE	50.00	6.0	12.7	100	Plano	50cm

REVISIONS

ZONE	REV.	DESCRIPTION	DATE	APPROVED
	-	Modeled from ATF5503	12-12-07	AOK

Advanced Thin Films

TITLE: Cylinder Cavity, Assembly Of

DRAWN: AOK 12-12-07

SIZE **B** | DWG. NO. ATF 6010 | REV —

SCALE: 1.25:1 | WEIGHT: | SHEET 1 OF 1

MATERIAL: See Table #1

FINISH: As Noted

Our cavity has the specification of row 1 of Table # 1.

Chapter C Timing Sequence

The following table shows the times after the polarizing pulses for the second, third and fourth pulses in units of ms that was used to collect data for the EDM experiment performed in October of 2014. The first number in each sequence represents the time of the second image after the first polarization pulse. Similarly the second and the third number represents the time of the third and fourth images after the second and the third polarization pulse respectively.

$$
\begin{aligned}
\text{Sequence1} \quad &\rightarrow [\ 20\ 2010\ 1949\ ] \\
\text{Sequence2} \quad &\rightarrow [\ 20\ 1949\ 2010\ ] \\
\text{Sequence3} \quad &\rightarrow [\ 20\ 2025\ 1935\ ] \\
\text{Sequence4} \quad &\rightarrow [\ 20\ 1935\ 2025\ ] \\
\text{Sequence5} \quad &\rightarrow [\ 20\ 1960\ 2000\ ] \\
\text{Sequence6} \quad &\rightarrow [\ 20\ 2000\ 1960\ ] \\
\text{Sequence7} \quad &\rightarrow [\ 20\ 1930\ 1995\ ] \\
\text{Sequence8} \quad &\rightarrow [\ 20\ 1995\ 1930\ ] \\
\text{Sequence9} \quad &\rightarrow [\ 20\ 1975\ 1949\ ] \\
\text{SequenceI10} \quad &\rightarrow [\ 20\ 1967\ 1998\ ]
\end{aligned}
$$

Table C.1: EDM sequences used in October.

The following table show the times in ms of the pulses that was used to collect data for the EDM experiment performed in December of 2014.

The time, at which the third and fourth images were taken was varied to measure absorption at different times after polarization. The third image is used to build up the "E field on" precession curve and the fourth image is used to build up the "E field off" precession curve of the ^{225}Ra atoms in the holding ODT.

Sequence1   → [17 1991 2021]
Sequence2   → [17 2021 1991]
Sequence3   → [17 1995 2017]
Sequence4   → [17 2017 1995]
Sequence5   → [17 1999 2013]
Sequence6   → [17 2013 1999]
Sequence7   → [17 2004 2008]
Sequence8   → [17 2008 2004]
Sequence9   → [17 2015 1997]
Sequence10   → [17 1997 2015]
Sequence11   → [17 2031 2040]

Table C.2: EDM sequences used in December.

Bibliography

[1] URL: http://www.universe-cluster.de/fierlinger/xedm.html.

[2] URL: http://www.ag-heil.physik.uni-mainz.de/60_ENG_HTML.php.

[3] URL: http://www.bnl.gov/edm/.

[4] URL: http://www.nndc.bnl.gov/chart/moveCenter.jsp?move=down.

[5] URL: https://www.isotopes.gov.

[6] URL: http://www.mdcvacuum.com/MDCMain.aspx.

[7] URL: http://hdl.handle.net/1773/9760.

[8] URL: http://www.andor.com/scientific-cameras/clara-interline-ccd-series/clara.

[9] URL: https://root.cern.ch/drupal/.

[10] URL: http://seal.web.cern.ch/seal/snapshot/work-packages/mathlibs/minuit/.

[11] R. Aaij et al. "First Observation of CP Violation in the Decays of B_s^0 Mesons". In: *Phys. Rev. Lett.* 110 (22 2013), p. 221601.

[12] K. Abe et al. "Observation of Large CP Violation in the Neutral B Meson System". In: *Phys. Rev. Lett.* 87 (9 2001), p. 091802.

[13] S.A. Ahmad et al. "Mean square charge radii of radium isotopes and octupole deformation in the 220228Ra region". In: *Nuclear Physics A* 483.2 (1988), pp. 244 –268.

[14] E. Arnold et al. "Direct measurement of nuclear magnetic moments of radium isotopes". In: *Phys. Rev. Lett.* 59 (7 1987), pp. 771–774.

[15] N. Auerbach, V. V. Flambaum, and V. Spevak. "Collective T - and P -Odd Electromagnetic Moments in Nuclei with Octupole Deformations". In: *Phys. Rev. Lett.* 76 (23 1996), pp. 4316–4319.

[16] C. A. Baker et al. "Improved Experimental Limit on the Electric Dipole Moment of the Neutron". In: *Phys. Rev. Lett.* 97 (13 2006), p. 131801.

[17] A. B. Balantekin et al. "Nuclear theory and science of the facility for rare isotope beams". In: *Modern Physics Letters A* 29.11 (2014), p. 1430010. eprint: `http://www.worldscientific.com/doi/pdf/10.1142/S0217732314300109`.

[18] S.M. Barr and William J. Marciano. "Electric Dipole Moments". In: *CP Violation.* Chap. 12, pp. 455–499. eprint: `http://www.worldscientific.com/doi/pdf/10.1142/9789814503280_0012`.

[19] G. W. Bennett et al. "Improved limit on the muon electric dipole moment". In: *Phys. Rev. D* 80 (5 2009), p. 052008.

[20] K. Bergmann, H. Theuer, and B. W. Shore. "Coherent population transfer among quantum states of atoms and molecules". In: *Rev. Mod. Phys.* 70 (3 1998), pp. 1003–1025.

[21] J. Biero, P. Indelicato, and P. Jnsson. "Multiconfiguration Dirac-Hartree-Fock calculations of transition rates and lifetimes of the eight lowest excited levels of radium". English. In: *The European Physical Journal Special Topics* 144.1 (2007), pp. 75–84.

[22] Eric D. Black. "An introduction to PoundDreverHall laser frequency stabilization". In: *American Journal of Physics* 69.1 (2001), pp. 79–87.

[23] J. H. Christenson et al. "Evidence for the 2 pi Decay of the K_2^0 Meson". In: *Phys. Rev. Lett.* 13 (4 1964), pp. 138–140.

[24] Steven Chu. "Nobel Lecture: The manipulation of neutral particles". In: *Rev. Mod. Phys.* 70 (3 1998), pp. 685–706.

[25] Timothy Chupp and Michael Ramsey-Musolf. "Electric Dipole Moments: A Global Analysis". In: (2014). arXiv:`1407.1064` `[hep-ph]`.

[26] Timothy Chupp and Michael Ramsey-Musolf. "Electric dipole moments: A global analysis". In: *Phys. Rev. C* 91 (3 2015), p. 035502.

[27] C. Ciofi et al. "Ultra low-noise current sources". In: *Instrumentation and Measurement, IEEE Transactions on* 47.1 (1998), pp. 78–81.

[28] A. G. Cohen, A. De Rjula, and S. L. Glashow. "A Matter-Antimatter Universe?" In: *The Astrophysical Journal* 495.2 (1998), p. 539.

[29] Claude N. Cohen-Tannoudji. "Nobel Lecture: Manipulating atoms with photons". In: *Rev. Mod. Phys.* 70 (3 1998), pp. 707–719.

[30] The ACME Collaboration et al. "Order of Magnitude Smaller Limit on the Electric Dipole Moment of the Electron". In: *Science* 343.6168 (Jan. 2014), pp. 269–272.

[31] CJ Copi, DN Schramm, and MS Turner. "Big-bang nucleosynthesis and the baryon density of the universe". In: *Science* 267.5195 (1995), pp. 192–199. eprint: `http://www.sciencemag.org/content/267/5195/192.full.pdf`.

[32] Andrzej Czarnecki and Bernd Krause. "Neutron Electric Dipole Moment in the Standard Model: Complete Three-Loop Calculation of the Valence Quark Contributions". In: *Phys. Rev. Lett.* 78 (23 1997), pp. 4339–4342.

[33] V. F. Dmitriev, R. A. Sen'kov, and N. Auerbach. "Effects of core polarization on the nuclear Schiff moment". In: *Phys. Rev. C* 71 (3 2005), p. 035501.

[34] V.F. Dmitriev and R.A. Sen'kov. "P-and T-violating Schiff moment of the mercury nucleus". English. In: *Physics of Atomic Nuclei* 66.10 (2003), pp. 1940–1945.

[35] J. Dobaczewski and J. Engel. "Nuclear Time-Reversal Violation and the Schiff Moment of ^{225}Ra". In: *Phys. Rev. Lett.* 94 (23 2005), p. 232502.

[36] V A Dzuba and V V Flambaum. "Calculation of energy levels and transition amplitudes for barium and radium". In: *Journal of Physics B: Atomic, Molecular and Optical Physics* 40.1 (2007), p. 227.

[37] V A Dzuba and V V Flambaum. "Calculation of energy levels and transition amplitudes for barium and radium". In: *Journal of Physics B: Atomic, Molecular and Optical Physics* 40.1 (2007), p. 227.

[38] V. A. Dzuba et al. "Electric dipole moments of Hg, Xe, Rn, Ra, Pu, and TlF induced by the nuclear Schiff moment and limits on time-reversal violating interactions". In: *Phys. Rev. A* 66 (1 2002), p. 012111.

[39] S. Eckel, A. O. Sushkov, and S. K. Lamoreaux. "Limit on the Electron Electric Dipole Moment Using Paramagnetic Ferroelectric $Eu_{0.5}Ba_{0.5}TiO_3$". In: *Phys. Rev. Lett.* 109 (19 2012), p. 193003.

[40] J. Engel, J. L. Friar, and A. C. Hayes. "Nuclear octupole correlations and the enhancement of atomic time-reversal violation". In: *Phys. Rev. C* 61 (3 2000), p. 035502.

[41] Jonathan Engel, Michael J. Ramsey-Musolf, and U. van Kolck. "Electric dipole moments of nucleons, nuclei, and atoms: The Standard Model and beyond". In: *Progress in Particle and Nuclear Physics* 71.0 (2013). Fundamental Symmetries in the Era of the {LHC}, pp. 21 –74.

[42] E. S. Ensberg. "Experimental Upper Limit for the Permanent Electric Dipole Moment of Rb^{85} by Optical-Pumping Techniques". In: *Phys. Rev.* 153 (1 1967), pp. 36–43.

[43] F. J. M. Farley et al. "New Method of Measuring Electric Dipole Moments in Storage Rings". In: *Phys. Rev. Lett.* 93 (5 2004), p. 052001.

[44] Richard Feynman. *The Feynman Lectures on Physics.* 1963,2006,2010. URL: http://www.feynmanlectures.info.

[45] V. V. Flambaum and J. S. M. Ginges. "Nuclear Schiff moment and time-invariance violation in atoms". In: *Phys. Rev. A* 65 (3 2002), p. 032113.

[46] Christopher J. Foot. *Atomic Physics.* Oxford University Press Inc. New York, 2005.

[47] Stephen Barr Fortson Norval Sandars Patrick. "The Search For Permanent Electric Dipole Moment". In: *Physics Today* 56 (4 2003), p. 33.

[48] Mary K. Gaillard, Paul D. Grannis, and Frank J. Sciulli. "The standard model of particle physics". In: *Rev. Mod. Phys.* 71 (2 1999), S96–S111.

[49]   Richard L. Garwin, Leon M. Lederman, and Marcel Weinrich. "Observations of the Failure of Conservation of Parity and Charge Conjugation in Meson Decays: the Magnetic Moment of the Free Muon". In: *Phys. Rev.* 105 (4 1957), pp. 1415–1417.

[50]   J.S.M. Ginges and V.V. Flambaum. "Violations of fundamental symmetries in atoms and tests of unification theories of elementary particles". In: *Physics Reports* 397.2 (2004), pp. 63 –154.

[51]   W. C. Griffith et al. "Improved Limit on the Permanent Electric Dipole Moment of ^{199}Hg". In: *Phys. Rev. Lett.* 102 (10 2009), p. 101601.

[52]   Rudolf Grimm, Matthias Weidemller, and Yurii B. Ovchinnikov. "Optical Dipole Traps for Neutral Atoms". In: ed. by Benjamin Bederson and Herbert Walther. Vol. 42. Advances In Atomic, Molecular, and Optical Physics. Academic Press, 2000, pp. 95 –170.

[53]   J. R. Guest et al. "Laser Trapping of ^{225}Ra and ^{226}Ra with Repumping by Room-Temperature Blackbody Radiation". In: *Phys. Rev. Lett.* 98 (9 2007), p. 093001.

[54]   W. Happer and B. S. Mathur. "Effective Operator Formalism in Optical Pumping". In: *Phys. Rev.* 163 (1 1967), pp. 12–25.

[55]   W. C. Haxton and E. M. Henley. "Enhanced T-Nonconserving Nuclear Moments". In: *Phys. Rev. Lett.* 51 (21 1983), pp. 1937–1940.

[56]   Xiao-Gang He, Bruce H. J. Mckellar, and Sandip Pakvasa. "Errata and Addendum: The Neutron Electric Dipole Moment". In: *International Journal of Modern Physics A* 06.06 (1991), pp. 1063–1066. eprint: `http://www.worlds cientific.com/doi/pdf/10.1142/S0217751X91002628`.

[57]   Peter Herczeg. "T-violation in nuclear interactions An overview". English. In: *Hyperfine Interactions* 43.1-4 (1988), pp. 75–93.

[58]   J. M. Higbie, E. Corsini, and D. Budker. "Robust, high-speed, all-optical atomic magnetometer". In: *Review of Scientific Instruments* 77.11, 113106 (2006), pp. –.

[59]   J. J. Hudson et al. "Improved measurement of the shape of the electron". In: *Nature* 473.7348 (May 2011), pp. 493–496.

[60]   John David Jackson. *Classical electrodynamics.* 3rd ed. New York, NY: Wiley, 1999.

[61]   I.B. Khriplovich. "The quark electric dipole moment and the induced -term in the Kobayashi-Maskawa model". In: *Physics Letters B* 173.2 (1986), pp. 193 –196.

[62]   I.B. Khriplovich and A.R. Zhitnitsky. "What is the value of the neutron electric dipole moment in the Kobayashi-Maskawa model?" In: *Physics Letters B* 109.6 (1982), pp. 490 –492.

[63]   Lamoreaux Steve Khriplovich Iosif B. *CP Violation Without Strangeness.* Heidelberg Germany: Springer.

[64]   T Kibdi and R.H Spear. "Reduced Electric-Octupole Transition Probabilities, B(E3;01+31)An Update". In: *Atomic Data and Nuclear Data Tables* 80.1 (2002), pp. 35 –82.

[65]   Makoto Kobayashi and Toshihide Maskawa. "CP-Violation in the Renormalizable Theory of Weak Interaction". In: *Progress of Theoretical Physics* 49.2 (1973), pp. 652–657. eprint: `http://ptp.oxfordjournals.org/content/49/2/652.full.pdf+html`.

[66] V. Alan Kostelecký and Neil Russell. "Data tables for Lorentz and *CPT* violation". In: *Rev. Mod. Phys.* 83 (1 2011), pp. 11–31.

[67] Andreas S. Kronfeld et al. "Project X: Physics Opportunities". In: (2013). Ed. by Andreas S. Kronfeld. arXiv:`1306.5009` [`hep-ex`].

[68] S K Lamoreaux and R Golub. "Experimental searches for the neutron electric dipole moment". In: *Journal of Physics G: Nuclear and Particle Physics* 36.10 (2009), p. 104002.

[69] L. Landau. "On the conservation laws for weak interactions". In: *Nuclear Physics* 3.1 (1957), pp. 127 –131.

[70] T. D. Lee and C. N. Yang. "Question of Parity Conservation in Weak Interactions". In: *Phys. Rev.* 104 (1 1956), pp. 254–258.

[71] MATLAB. *version 7.10.0 (R2010a)*. Natick, Massachusetts: The MathWorks Inc., 2010.

[72] Harold J. Metcalf and Peter van der Straten. *Laser Cooling and Trapping of Neutral Atoms*. Wiley-VCH Verlag GmbH Co. KGaA, 2007.

[73] S. A. Murthy et al. "New limits on the electron electric dipole moment from cesium". In: *Phys. Rev. Lett.* 63 (9 1989), pp. 965–968.

[74] "Nuclear Emulsion Evidence for Parity Nonconservation in the Decay Chain π^+-μ^+-e$^+$, author = Friedman, Jerome I. and Telegdi, V. L., journal = Phys. Rev., volume = 105, issue = 5, pages = 1681–1682, numpages = 0, year = 1957, month = Mar, publisher = American Physical Society, doi = 10.1103/PhysRev.105.1681.2, url = http://link.aps.org/doi/10.1103/PhysRev.105.1681.2". In: ().

[75] "Nuclear spin maser and experimental search for 129 Xe atomic EDM". In: *Hyperfine Interactions* (2013).

[76] C. F. Ockeloen et al. "Detection of small atom numbers through image processing". In: *Phys. Rev. A* 82 (6 2010), p. 061606.

[77] R. H. Parker et al. "Efficient, tightly-confined trapping of 226Ra". In: *Phys. Rev. C* 86 (6 2012), p. 065503.

[78] R. H. Parker et al. "First Measurement of the Atomic Electric Dipole Moment of ^{225}Ra". In: *Phys. Rev. Lett.* 114 (23 2015), p. 233002.

[79] R. D. Peccei and Helen R. Quinn. "CP Conservation in the Presence of Pseudoparticles". In: *Phys. Rev. Lett.* 38 (25 1977), pp. 1440–1443.

[80] Jen-Chieh Peng. "Neutron Electric Dipole Moment Experiments". In: *Modern Physics Letters A* 23.17n20 (2008), pp. 1397–1408. eprint: `http://www.worldscientific.com/doi/pdf/10.1142/S0217732308027771`.

[81] William D. Phillips. "Nobel Lecture: Laser cooling and trapping of neutral atoms". In: *Rev. Mod. Phys.* 70 (3 1998), pp. 721–741.

[82] William D. Phillips and Harold Metcalf. "Laser Deceleration of an Atomic Beam". In: *Phys. Rev. Lett.* 48 (9 1982), pp. 596–599.

[83] M A Player and P G H Sandars. "An experiment to search for an electric dipole moment in the 3 P 2 metastable state of xenon". In: *Journal of Physics B: Atomic and Molecular Physics* 3.12 (1970), p. 1620.

[84] Maxim Pospelov and Adam Ritz. "Electric dipole moments as probes of new physics". In: *Annals of Physics* 318.1 (2005). Special Issue, pp. 119 –169.

[85] M.E. Pospelov and I.B. Khriplovich. "Electric dipole moment of the W boson and the electron in the Kobayashi-Maskawa model". In: *Sov.J.Nucl.Phys.* 53 (1991), pp. 638–640.

[86] E. M. Purcell and N. F. Ramsey. "On the Possibility of Electric Dipole Moments for Elementary Particles and Nuclei". In: *Phys. Rev.* 78 (6 1950), pp. 807–807.

[87] E. L. Raab et al. "Trapping of Neutral Sodium Atoms with Radiation Pressure". In: *Phys. Rev. Lett.* 59 (23 1987), pp. 2631–2634.

[88] B. C. Regan et al. "New Limit on the Electron Electric Dipole Moment". In: *Phys. Rev. Lett.* 88 (7 2002), p. 071805.

[89] M. V. Romalis and E. N. Fortson. "Zeeman frequency shifts in an optical dipole trap used to search for an electric-dipole moment". In: *Phys. Rev. A* 59 (6 1999), pp. 4547–4558.

[90] Andrei D Sakharov. "Violation of CP in variance, C asymmetry, and baryon asymmetry of the universe". In: *Soviet Physics Uspekhi* 34.5 (1991), p. 392.

[91] Jun John Sakurai and Jim Napolitano. *Modern quantum mechanics; 2nd ed.* San Francisco, CA: Addison-Wesley.

[92] L. I. Schiff. "Measurability of Nuclear Electric Dipole Moments". In: *Phys. Rev.* 132 (5 1963), pp. 2194–2200.

[93] John H. Schwarz and Nathan Seiberg. "String theory, supersymmetry, unification, and all that". In: *Rev. Mod. Phys.* 71 (2 1999), S112–S120.

[94] Julian Schwinger. "The Theory of Quantized Fields. III". In: *Phys. Rev.* 91 (3 1953), pp. 728–740.

[95] U. Schnemann et al. "Simple scheme for tunable frequency offset locking of two lasers". In: *Review of Scientific Instruments* 70.1 (1999).

[96] N. D. Scielzo et al. "Measurement of the lifetimes of the lowest $^3P_1$ state of neutral Ba and Ra". In: *Phys. Rev. A* 73 (1 2006), p. 010501.

[97] Y. Singh and B. K. Sahoo. "Electric dipole moment of ^{225}Ra due to P- and T-violating weak interactions". In: *ArXiv e-prints* (Apr. 2015). arXiv:`15 04.00269 [physics.atom-ph]`.

[98] J. H. Smith, E. M. Purcell, and N. F. Ramsey. "Experimental Limit to the Electric Dipole Moment of the Neutron". In: *Phys. Rev.* 108 (1 1957), pp. 120–122.

[99] V. Spevak, N. Auerbach, and V. V. Flambaum. "Enhanced T-odd, P-odd electromagnetic moments in reflection asymmetric nuclei". In: *Phys. Rev. C* 56 (3 1997), pp. 1357–1369.

[100] F.W. Stecker. "On the Nature of the Baryon Asymmetry". In: *Nucl.Phys.* B252 (1985), pp. 25–36.

[101] Gary Steigman. "Observational Tests of Antimatter Cosmologies". In: *Annual Review of Astronomy and Astrophysics* 14.1 (1976), pp. 339–372. eprint: `htt p://dx.doi.org/10.1146/annurev.aa.14.090176.002011`.

[102] Ibrahim A. Sulai. "Precision Spectroscopy of Laser Trapped Helium and Radium Atoms". In: (2011).

[103] E.R. Tardiff et al. "The radon EDM apparatus". English. In: *Hyperfine Interactions* 225.1-3 (2014), pp. 197–206.

[104] Mark Trodden. "Electroweak baryogenesis". In: *Rev. Mod. Phys.* 71 (5 1999), pp. 1463–1500.

[105] T. G. Vold et al. "Search for a Permanent Electric Dipole Moment on the ^{129}Xe Atom". In: *Phys. Rev. Lett.* 52 (25 1984), pp. 2229–2232.

[106] Steven Weinberg. "A New Light Boson?" In: *Phys. Rev. Lett.* 40 (4 1978), pp. 223–226.

[107] F. Wilczek. "Problem of Strong P and T Invariance in the Presence of Instantons". In: *Phys. Rev. Lett.* 40 (5 1978), pp. 279–282.

[108] C. S. Wu et al. "Experimental Test of Parity Conservation in Beta Decay". In: *Phys. Rev.* 105 (4 1957), pp. 1413–1415.

Vita

Education

- Indian Institute of Technology Guwahati, M.Sc. 2006.

Experience

- Physics Division, Argonne National Laboratory, Lemont, IL April 2010-April 2015.

- Department of Physics and Astronomy, University of Kentucky, Lexington, KY Summer 2008-March 2010.

Publications

- "First measurement of the permanent electric dipole moment (EDM) of the ^{225}Ra atom". R.H. Parker, M.R. Dietrich, M.R. Kalita, N.D. Lemke, K. G. Bailey, M. N. Bishof, J.P. Greene, R.J. Holt, W. Korsch, Z. -T. Lu, P. Mueller, T.P. O'Connor and J. T. Singh, Phys. Rev. Lett. 114, 233002 (2015).

- "Search for a permanent electric dipole moment (EDM) of ^{225}Ra atom". M.R. Kalita, M. Bishof, K. Bailey, M.R. Dietrich, J.P. Greene, R.J. Holt, W. Korsch, Z. -T. Lu, N.D. Lemke, P. Mueller, T.P. O'Connor, R.H. Parker, J. T. Singh, CLEO 2015 conference proceedings (2015).

- "Progress towards the search for the electric dipole moment of ^{225}Ra"., K. Bailey, M. R. Dietrich, J. P. Greene, R. J. Holt, M. R. Kalita, W. Korsch, ND Lemke, Z.-T. Lu, P. Mueller, T. P. O'Connor, R. H. Parker, J. T Singh, PAVI 14 conference proceedings (2014).

121

- "Efficient, tightly-confined trapping of ^{226}Ra". R. H. Parker, M. R. Dietrich, K. Bailey, J. P. Greene, R. J. Holt, M. R. Kalita, W. Korsch, Z.-T. Lu, P. Mueller, T. P. O'Connor, J. Singh, I. A. Sulai, and W. L. Trimble, Phys. Rev. C 86 065503 (2012).